HySA/Catalysis Centre of Competence, Catalysis Institute

Department of Chemical Engineering

University of Cape Town


# Low PGM PtCo alloy catalysts for low loading Polymer Electrolyte Membrane Fuel Cells

Submitted in partial fulfilment of the requirements for the degree of Master of Science in Chemical Engineering

**By: Tiaan Munro**
**Supervisor: Dr Jessica Chamier**
**Co-supervisor: Dr Darija Susac**

February 2023

# Abstract

Polymer Electrolyte Membrane Fuel Cells (PEMFCs) are a promising means of generating clean energy in especially transportation applications. The electrochemical conversion of energy is driven within membrane electrode assemblies (MEAS) over costly Pt catalyst which limits PEMFC cost viability. PtCo alloy catalysts are attractive alternatives to Pt, with similar or higher catalytic activity at a reduced cost. The catalyst is combined with a perfluorosulfonic acid (PFSA) ionomer which serves as the proton conductor and binder to form the catalyst layer (CL). The ionomer contains both hydrophilic and hydrophobic groups, and therefore plays a key role in water management in the fuel cell. In every MEA design, ionomer content needs to be optimised to maximise fuel cell performance, ensuring adequate reactant-catalyst interaction, without flooding the MEA. This optimal ionomer content depends on the properties of the ionomer as well as catalyst characteristics (such as platinum loading, carbon to metal ratio and particle size), as well as fuel cell operating conditions.

To establish an ideal low PGM MEA design, this thesis investigated two commercial PtCo catalysts (PtCoU30 and PtCoT50). Physical and electrochemical characterisation of the PtCo catalysts were investigated and compared to an in-house Pt benchmark (PtH40). The morphology, composition, size distribution, physical surface area, electrochemical surface area, performance and durability of these catalysts were established. Electrochemical characterization of the two catalysts showed that the higher Pt loading catalyst (PtCoT50) had lower mass activity compared to the lower Pt loading catalyst (PtCoU30). The PtCoT50 catalyst, however, exhibited similar specific activity. The electrochemical surface area of PtCoT50 was smaller than that of PtCoU30, which was consistent with the larger particle sizes observed for PtCoT50. Ex-situ accelerated stress tests showed that the higher metal loading catalyst was more susceptible to PtCo metal degradation but had greater carbon support durability.

The ionomer contents for PtCoU30 and PtCoT50 MEAs were optimised at 30 wt% and 24 wt% respectively. This suggested that the higher metal content catalyst (PtCoT50) required less ionomer than the PtCoU30, due to the thinner catalyst layer thickness. Both optimised PtCo MEAs outperformed the PtH40 benchmark. This trend was consistent with the activities seen in ex-situ Rotating Disk Electrode (RDE) testing.

The impact of incorporating ionomer in different ink preparation stages/phases on performance and durability was determined. A 1-phase catalyst ink was prepared by adding the ionomer to catalyst prior to heat treatment, and solvent addition. A 2-phase ink was made by adding additional ionomer to the 1-phase ink, without being heat treated. It was shown that the performance for the PtCo catalysts was higher when all the ionomer was added in the heat treatment phase. However, the 2-phase MEAs showed slightly improved carbon corrosion and particle stability. It was suggested that the minor improvement in stability for 2-phase MEAs did not override the 1-phase MEA performance benefit . The recommended design for a low PGM PtCo MEA based on these findings is a 30 wt% PtCo/C MEA with 30 wt% ionomer content added during the heat treatment phase.

# Plagiarism Declaration

I know the meaning of plagiarism and declare that all the work in the document, save for that which is properly acknowledged, is my own. This thesis/dissertation has been submitted to the Turnitin module and I confirm that my supervisor has seen my report and any concerns revealed by such have been resolved with my supervisor.

Signature: Signed by candidate

Date: 10/02/2023

# Acknowledgements

I am incredibly grateful to have had the opportunity to do a master's degree, especially in the field of Hydrogen fuel cells. It has been a pleasure to contribute even a small part to research into this technology. I have been blessed with an incredible amount of support over the past 2 years.

Firstly, and most importantly, I must thank you Jessica. I will forever be grateful to you for seeing potential in me and giving me this opportunity. You have been the best supervisor I could hope for. Your unwavering support, warm nature, willingness to engage, listen and problem solve have been immeasurably important to me. Thank you for always being available, for understanding when I'm not at my best, and for your encouragement and positivity. You have earned my lifelong respect and admiration, not only as a mentor and teacher, but also a friend. It has been a true pleasure being your student.

To Darija, my co-supervisor, thank you for stepping in and offering your full commitment to seeing me through this thesis. Thank you for your consistent willingness to help wherever I needed it. Your support and guidance in my writing has made me a better scientist. Thank you for dedicating so much of your time to my project. Specifically, for getting your hands dirty and doing SEM and EDX characterisation on my MEA samples. Your support has been a blessing.

To Ziyanda, thank you for welcoming me so warmly to the HySA team. You were my first teacher. Thank you for so thoroughly training me and assisting with RDE experiments. To Bettina and Ursula, thank you for all the MEA preparation and testing work you did for me. Your kindness and willingness to help me, even when it certainly wasn't your job to, has been a real delight these past two years. To Lazahn, thank you for helping out with RDE experiments; I am very grateful for your diligence in sometimes conducting multiple rounds of testing to get the perfect results. To Johnathan Gertzen, thank you for providing me with a particle stability test protocol, my thesis would've sorely missed it.

To my parents, Kobus and Ryette Munro, your love and support have meant the world to me. Thank you for all you have sacrificed for me to be where I am. And finally, to my beautiful partner, Willem, I could not have done this without you; I love you.

# Table of Contents

# List of Figures

# List of Tables

# Nomenclature

| | |
|---|---|
| AST | Accelerated Stress Test |
| CCL | Cathode Catalyst Membrane |
| CCM | Catalyst Coated Membrane |
| DOE | Department of Energy |
| ECSA | Electrochemical Surface Area |
| HOR | Hydrogen Oxidation Reaction |
| MA | Mass Activity |
| MEA | Membrane Electrode Assembly |
| ORR | Oxygen Reduction Reaction |
| PEM | Polymer Electrolyte Membrane |
| PEMFC | Polymer Electrolyte Membrane Fuel Cell |
| PFSA | Perfluorinated sulfonic acid |
| PGM | Platinum Group Metal |
| SA | Specific Activity or South Africa |
| TM | Transition Metal |
| TPB | Triple Phase Boundary |

# 1 introduction

## 1.1 Background

The current climate change crises have given rise to increasing concerns about the global dependence on fossil fuel combustion as an energy source. The scientific, as well as global political community have therefore been making concerted efforts invest in advanced clean energy technology. Hydrogen is one of the most promising vectors for storing energy, with polymer electrolyte membrane fuel cells (PEMFCs) being a central technology for efficient clean electrical energy. The conversion of hydrogen into electricity is a clean process, using air and hydrogen to produce electricity and water (Banham and Ye, 2017). Fuel cells are attractive power sources for a range of stationary and automotive applications owing to their low operating temperature, high power density, and easy scale-up, (Wang et al., 2020). PEMFC research directly addresses the Sustainable Development Goals for affordable and clean energy; industry, innovation and infrastructure; and climate action.

The major barrier for competitive commercialisation of PEMFCs, particularly in automotive applications, is the use of Platinum-Group-Metal (PGM) catalysts, which are platinum, palladium, rhodium, ruthenium, iridium, and osmium. In fuel cell applications platinum exhibits the highest activity of these PGMs, and cannot be feasibly replaced without significant losses in performance (Yang, 2009). At large scale fuel cell production platinum accounts for roughly 50 % of the projected total cost (Du et al., 2021). For perspective: the cost of platinum as a commodity is about 50 000 times more expensive than stainless steel (US$ 30 per gram in 2019) (Pollet, Kocha and Staffell, 2019). A solution that has been pursued in recent years is to reduce the use of PGM catalysts by decreasing the Pt loading in the catalyst layer of a PEMFC, while meeting performance requirements. However, at lower loadings, PEMFCs exhibit decreased stability and lifespan, associated with thinner catalyst layers.

Recently Platinum alloys have become the most used catalysts for the Oxygen Reduction Reaction (ORR) on the cathode of PEMFCs. Platinum alloyed with transition metals (TMs) such as Co, Ni or Fe has been shown to achieve higher electrochemical mass activity (MA) and demonstrates similar or better durability than

pure platinum catalysts, with the added benefit of being significantly less expensive, (Banham and Ye, 2017).

PtCo alloy catalysts, specifically, have been investigated extensively as a material solution for reducing Platinum usage, while maintaining sufficient performance. The increased activity of these PtCo catalysts can be attributed to the moderation of binding strength of reaction intermediates and increased efficiency in breaking of the $O_2$ double-bond. This binding moderation effect is caused by the geometric strain induced by sub-surface cobalt, as well as the electronic ligand effect which modifies Pt binding properties (Ramaswamy et al. 2021). It has been shown extensively in literature that PtCo catalysts exhibit greater performance than Pt catalysts in ex-situ rotating disk electrode (RDE) studies, as well as in-situ fuel cell performance testing (Ramaswamy et al., 2021; Garsany et al., 2018; Papadias et al., 2018; Kocha et al., 2017; Shinozaki et al., 2016; Nikkuni et al., 2015; Zignani, Antolini and Gonzalez, 2008; Santiago, Varanda and Villullas, 2007). It has also been shown that the mechanisms of degradation differ between PtCo and Pt catalysts owing to the role of sacrificial anode that Co plays in the harsh oxidative environment of fuel cell operation. Co therefore has a protective role, but conversely affects performance by poisoning the membrane in the PEMFC (Myers et al., 2021; Ball et al., 2006).

The catalyst layer (CL) in Membrane Electrode Assemblies (MEAs), contains both the catalyst as well as a perfluorosulfonic acid (PFSA) ionomer which serves as the proton conductor and binder. The ionomer contains both hydrophilic and hydrophobic groups, and therefore plays a key role in water management in a MEA. The amount of proton conducting ionomer in the CL can be optimised to maximise fuel cell performance, ensuring adequate reactant-catalyst interaction, without flooding the MEA (Kim et al., 2010). This optimal ionomer content depends on catalyst parameters such as platinum loading, carbon to metal ratio and particle size, as well as fuel cell operating conditions.

In the present work the *ex-situ* (RDE) and *in-situ* (fuel cell) performance and durability of two commercial PtCo catalysts with varying metal contents were compared against a commercial high surface area Pt/C benchmark. Herein, the respective catalyst and catalyst layer characteristics were studied to determine the link between catalyst properties and the optimal ionomer content in an MEA. The goal was to produce a

high performing low loading MEA using a PtCo catalyst and to understand the impact of the ink preparation method on the resulting MEA performance and durability.

## 1.2 Key questions

The key questions which the proposed project aims to answer are:

1. How does the difference in morphology and composition of two commercial PtCo catalysts affect ORR performance?
2. How and to what extent does the properties of the respective PtCo catalysts impact the optimal ionomer content and final MEAs performance?
3. Can the method for introducing ionomer to the ink impact MEA performance, and does the result differ depending on the properties of the catalyst?
4. What is the affect and impact of adding ionomer to the catalyst ink at different stages of ink preparation on MEA performance and durability?

## 1.3 Research objectives

The goal of this project is to design a high performing low Pt loading MEA using a PtCo catalyst with reasonable durability. To achieve this goal and address some of the key questions, the following objectives were set;

- To determine and compare the physical and electrochemical properties of two commercial PtCo alloy catalysts against a Pt benchmark, for use in PEMFC MEA.
- Optimise the MEA ionomer content used for two commercial PtCo catalysts to select the best performing catalyst for low loading MEAs.
- Investigate the effect of catalyst ink preparation (using heat treated and partially heat treater ionomer/catalyst inks) on performance and durability for two commercial PtCo catalysts.

## 1.4 Hypothesis

PtCo alloy MEAs, at a total loading of 0.25 $mg_{Pt}/cm^2$, using Aquivion 720 EW ionomer will show improved performance compared to a Pt benchmark. The optimal MEA ionomer content and catalyst layer structure of the two commercial PtCo catalysts will depend on their respective properties, including metal loading, particle size and support characteristics. The catalyst layer structure, performance and durability may differ from what has been shown at higher loadings in literature. Ionomer addition to the catalyst ink at different stages of ink preparation will affect the PtCo catalyst layer structures differently based on their respective properties. These differences will affect the performance and durability of the MEAs. A high performing low PGM PtCo MEA design can be presented based on an optimised ionomer content and ink preparation method.

## 1.5 Thesis layout

Chapter 1 provides the background, key questions, and objectives of the project. Chapter 2 contains a relevant literature review which informs the design of a low PGM PtCo MEA. The reviewed literature includes an overview of PEMFC components and operation, measures of performance, catalyst layer components including ORR catalysts and ionomers, the impact of ionomer on catalyst layer structure, ionomer optimisation in the catalyst layer, and finally a review of studies showing the effects of catalyst characteristics on PEMFC performance and durability. Chapter 3 presents the experimental techniques used and the methodology followed for each technique. Chapter 4 presents the experimental results of the thesis, which address the presented objectives. Section 4.1 contains the physical an electrochemical characterisation of the two PtCo catalysts and Pt benchmark catalyst under investigation, including ex-situ performance and durability studies performed in a 3-electrode RDE setup. Section 4.2 presents in-situ MEA ionomer optimisation studies for the two commercial PtCo catalysts. Section 4.3 presents the results from an investigation on the effect of thermal treatment of ionomers on MEA performance and durability for the optimised PtCo MEAs. Finally, a design for a low PGM PtCo MEA is presented. Chapter 5 gives the conclusions of the current work and recommendations for future consideration.

# 2 Literature review

A review of PEMFC catalysis is presented in this chapter. The following topics are addressed in order: an overview of PEMFC components and operation, measures of performance, catalyst layer components including ORR catalysts and ionomers, the impact of ionomer on catalyst layer structure, ionomer optimisation in the catalyst layer, and finally a review of studies showing the effects of catalyst characteristics on PEMFC performance and durability. The information presented here provides the necessary context for the informed design of a low PGM PtCo MEA.

## 2.1 Polymer Electrolyte Membrane Fuel Cells

### 2.1.1 Components and operation

Polymer electrolyte membrane fuel cells (PEMFCs) currently exhibit the highest power density among all fuel cell types (500 to 2500 mW/cm$^2$), as well as very good starting and stopping capabilities (O'hayre Ryan, 2016). These factors, along with its low operating temperature have made PEMFCs the major technology of interest for portable power and fuel cell electric vehicles (FCEVs). PEMFCs are constructed of various components. The most basic building blocks are the polymer electrolyte membrane (typically a perfluorinated sulfonic acid membrane), which acts as a proton conductor (O'hayre Ryan, 2016) and two electrodes responsible for the electrochemical reactions.

The electrodes constitute anode and cathode catalyst layers, which are in contact with an external electron conducting circuit. The catalyst electrode and membrane are sandwiched between gas diffusion layers to make a membrane electrode assembly (MEA), which in its entirety is less than 1 mm in thickness.

The basic principle of the operation of a PEMFC is depicted in the schematic Figure 2-1. At the anode, humidified Hydrogen gas enters, passing through a gas diffusion layer (GDL), and is oxidised into protons and electrons at the catalyst layer. The protons pass through the membrane to the cathode, whereas the electrons pass through the external circuit, generating a current. The membrane must remain hydrated with liquid water to facilitate proton conductivity. This also requires that the operating temperature of PEMFCs be below 90°C. At the cathode, humidified oxygen

gas (in the form of air) is supplied, passing through a GDL to the catalyst layer. Oxygen is reduced in the presence of a catalyst, combining with the protons and electrons, completing the circuit and producing water as a product. In this way Hydrogen and Oxygen are used as fuel for generating electricity, which may be harnessed in stationary or automotive applications.

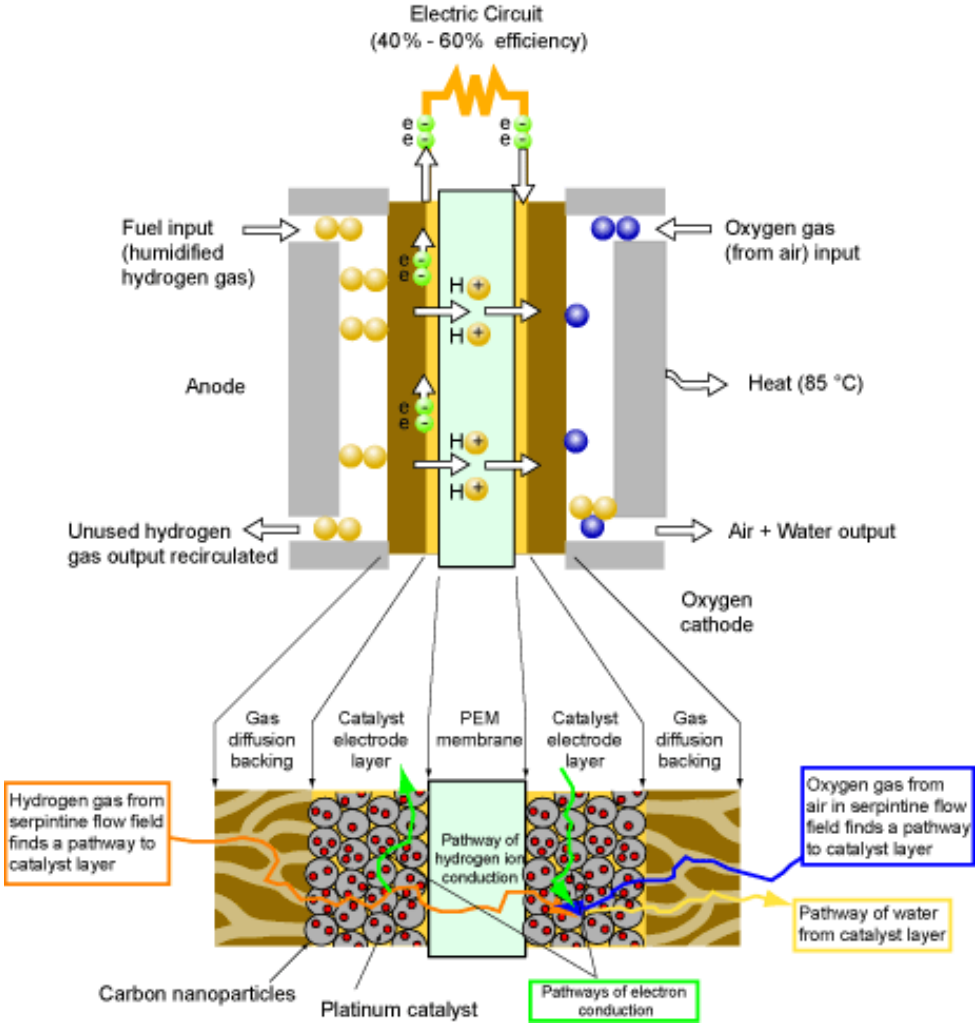


*Figure 2-1: Schematic of PEMFC, consisting of catalyst coated anode and cathode, polymer electrolyte membrane and external electron conducting circuit (National Institute of Standards and Technology, 2006).*

The Polymer Electrolyte Membrane (PEM) used in PEMFCs facilitates the transport of protons from the anode to the cathode and is therefore a critically important component of the fuel cell. PFSA polymers are referred to simply as ionomers. These ionomers are also commonly incorporated into the catalyst layers themselves, to extend the proton conductivity into the bulk catalyst layer from the membrane, and to

act as a binder. The ionomer contains both hydrophilic and hydrophobic groups, and therefore plays a key role in water management in a MEA (Kim et al., 2010).

The conversion of chemical energy to electrical energy in the PEMFCs is driven by the catalysts in the anode and cathode layer. The respective electrochemical reactions occurring at the anode and cathode are given by equations 2.1 hydrogen oxidation reaction, (HOR) and 2.2 oxygen reduction reaction, (ORR), respectively.

$$2H_2 \rightarrow 4H^+ + 4e^- \qquad 2.1$$

$$O_2 + 4H^+ + 4e^- \rightarrow 2H_2O \qquad 2.2$$

The ORR is notoriously sluggish, requiring a large overpotential for the reaction to occur, which significantly limits the overall efficiency of the fuel cell (Hargreaves, McFarlane and Said, 2018). The ORR reaction scheme for Pt electrodes is shown in Figure 2-2 (Sethuraman et al., 2009). Adsorbed oxygen may form water directly, via the 4-electron pathway (associative mechanism), or the superoxo radicals may combine with surrounding protons to form an $H_2O_2$ intermediate, which then reduces to form water (2-electron pathway, or dissociative pathway). The $H_2O_2$ may also escape into the bulk (Sethuraman et al., 2009). The 4-electron pathway is more efficient, and therefore the desired pathway for energy generation applications. Binary and ternary Pt alloys have higher selectivity towards $H_2O_2$ formation compared to Pt catalysts, especially at low potentials. The ORR reaction efficiency is an important consideration when designing an MEA.

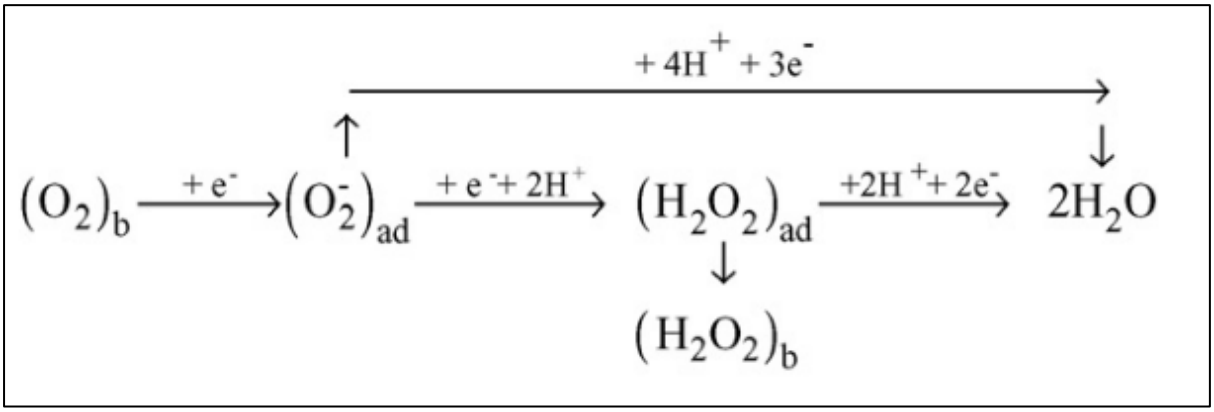


*Figure 2-2: ORR reaction scheme on Pt electrodes. Adapted from Sethuraman et al. (2009)*

### 2.1.2 ORR Catalysts

Among all pure metals, platinum is known to have the highest catalytic activity for the ORR, however, under typical fuel cell operating conditions, cathodic overpotential losses still amount to approximately 0.4 V (Zignani, Antolini and Gonzalez, 2008). The specific challenges presented by the efficiency losses of the ORR have led to significant effort in improving and optimising electrocatalysts used on the cathode of PEMFCs. In the past decade there have been considerable advances in ORR catalyst technology. Banham and Ye (2017) categorize the current state of catalysts into 6 broad groups, namely:

1. Pt/C catalysts
2. Pt and Pt alloy/dealloy catalysts
3. Core-shell catalysts
4. Non-precious metal catalysts
5. Shape controlled nanocrystal catalysts.
6. Nanoframe catalysts

This list is ordered in terms of relative stage of development, with the Pt/C catalysts being the most mature technology and nanoframe catalysts being at a very early stage of development. While pure Pt catalysts are well established and have undergone significant improvements, most notably with regards to catalyst-support interactions, Pt-alloy catalysts have become the new baseline catalysts on the commercial level (Banham and Ye, 2017).

Pt-Alloy catalysts have been shown to have greater mass activities than Pt/C catalysts, with similar or better durability (Banham and Ye, 2017). Examples of such alloys are PtCo, PtNi, PtFe, PtCr, PtV, PtTi, PtW, PtAl, and PtAg. The two major physicochemical beneficial properties that these alloys exhibit as compared to pure Pt/C catalysts are an increase in dissociative adsorption of oxygen onto the catalyst, owing to smaller inter-atomic distance in the metallic lattice; and secondly, an inhibiting effect on OH adsorption (Banham and Ye, 2017). The electrochemical surface area ECSA is an important factor that determines the performance and efficiency of a fuel cell, as it determines the rate of reaction between the fuel and the oxidant. The ECSA is the total surface area that is available for electrochemical reaction. The ECSA in ORR

catalysts is a function of the triple-phase boundary, which is the interface between ionomer, catalyst particles, and gas phase. This is elaborated on in section 3.2.4.

Pt is scarce, expensive, and susceptible to CO poisoning at standard operating temperatures. PtCo alloys are attractive alternative catalyst materials because they exhibit good catalyst kinetics, while being able to reduce the Pt loading. This Thesis aims to address this opportunity in adding to the knowledge base of PtCo catalysts for PEMFCs, which have the potential to help meet current global loading, performance, and durability standards.

### 2.1.3 Standards and measures of performance

The activity, ECSA, and durability of ORR catalysts are measured using *ex-situ* Rotating Disk Electrochemistry (RDE). These techniques are elaborated on in section 3.2. In-situ performance (polarisation curves) and durability are determined for membrane electrode assembly (MEA). In-situ techniques used in the current work are presented in section 3.3. Currently the major objectives for MEAs using Pt-alloy catalysts are to meet performance and durability targets for automotive applications, as well as to decrease the amount of platinum used. Summarised in Table 2-1 are the United States Department of Energy 2020 targets for electrocatalysts for transportation applications (DOE Fuel Cell Technologies Office, 2016). Notably, these performance target measures include Pt metal content, loading, mass activity, and performance loss following accelerated stress tests.

*Table 2-1: United States Department of Energy 2020 targets for electrocatalysts for transportation applications*

| Characteristic | Units | 2020 Target |
|---|---|---|
| Platinum group metal total content (both electrodes) | g/kW (rated, gross) @ 150 kPa (abs) | 0.125 |
| Platinum group metal (PGM) total loading (both electrodes) | $mg_{Pt}/cm^2$ electrode area | 0.125 |
| Mass activity | A/mg PGM @ 900 $mV_{iR\text{-}free}$ | 0.44 |
| Loss in initial catalytic activity | % mass activity loss | <40 |
| Loss in performance at 0.8 $A/cm^2$ | mV | <30 |
| Electrocatalyst support stability | % mass activity loss | <40 |
| Loss in performance at 1.5 $A/cm^2$ | mV | <30 |
| PGM-free catalyst activity | A / cm2 @ 900 $mV_{IR\text{-}free}$ | >0.044 |

### 2.1.4 Key challenges, and Shortcomings

The primary barriers to commercialization of automotive fuel cells are cost, durability, and hydrogen infrastructure availability. Significant fundamental research is required, especially for membrane and catalyst materials, in order to facilitate better degradation resistance and lower Pt loadings. Among all the fuel cell components, the CL contributes the largest portion of the cost, at 40% of the total fuel cell cost (Wang et al. 2020). Research on the reduction of PGM catalysts use in PEMFC catalyst layers is therefore a major focus in order to further the commercialisation of fuel cell applications. The major challenge associated with this reduction in PGMs is the reduced Pt layer utilisation, durability and reliability seen with lower loadings. When PGM loading is reduced from 0.15 to 0.05 $mg_{Pt}/cm^2$ it has been shown that the fuel cell durability drops significantly (Du et al., 2021). Durability of automotive PEMFCs specifically has been highlighted as a critical issue for the commercialisation of the technology. At low loadings, degradation of stack voltage due to activity loss is the major cause of fuel cell system failure (Yu and Ye, 2007).

## 2.2 Catalyst layer structure performance properties

The catalyst layer structure is a porous layer consisting of ionomer, carbon support, PGM catalyst and dispersing solvent. The performance and durability of an MEA strongly depends on the structural properties of the catalyst layer. Catalyst particle size and morphology affect the porosity of the CL. Small homogenous particles result in a uniform, porous CL. Higher loadings result in denser CLs (Kumano et al., 2019). Other factors influencing the catalyst layer structure, including the coating technology, the ink formulation, catalyst and ionomer properties are addressed in this section.

### 2.2.1 Catalyst layer coating technology

The methods for producing catalyst layers typically include depositing a dispersed ink solution onto a substrate through either inkjet printing, electrostatic spraying, slit coating, screen printing, or ultrasonic spraying (Yang et al., 2021). The sprayed ink is then dried by evaporation. The microstructure and ionomer distribution in the catalyst layer (CL) therefore depends on the microstructures of the catalyst material as well as ionomers in the inks. In the current work, ultrasonic spraying was fixed in the methodology used for producing the MEAs.

### 2.2.2 Ink formulation

The dispersing solvent used in fuel cell catalyst ink preparation has significant effects on the microstructure of the CL structure. The performance and durability of PEMFCs therefore strongly depend on the quality of catalyst ink dispersions (Lei et al., 2021).

The alcohol/water ratio plays a significant role in the quality of catalyst dispersion. Kim et al. (2012) showed that increasing the 2-propanol to water ratio in the cathode catalyst ink preparation resulted in improved performance due to a reduction in the secondary particle aggregate sizes in the CL. This is supported by Takahashi et al. (2015) who showed that alcohol-rich inks produce well dispersed ionomer in the CL with a larger number of small agglomerates, compared to water-rich inks which had large agglomerates with poor agglomerate/ionomer interface. This is illustrated in Figure 2-3, which shows the changes in catalyst ink and catalyst layer with different water/1-propanol ratios. It has also been shown that water-rich PtCo inks are more susceptible to leaching of Co in the ink, resulting in a contraction of the PtCo lattice (Myers et al., 2021). Dealloying of the PtCo results in particles with Pt-rich skins and Co-rich cores. Considering these ink effects, Increasing the alcohol/water ratio in catalyst inks may therefore offer a solution for poor dispersion and excessive Co loss.

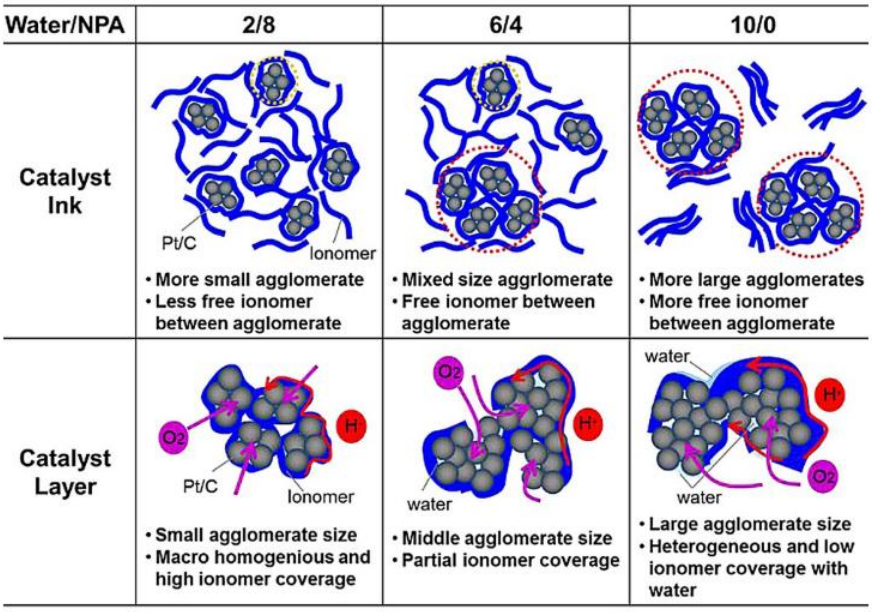


*Figure 2-3: Schematic representation of catalyst ink and catalyst layer physical characteristics at different ink water/NPA ratios. Adapted from Takahashi et al. (2015)*

The structure of a CL also depends on the methods of dispersion used. Common dispersion methods include ultrasonication, high-shear emulsifier, high-pressure homogenization and ball milling (Yang et al., 2021).

Yang et al. (2021) showed that treatment of ionomer with the catalyst in a ultrasonic water bath affects the catalyst layer structure. They showed that the water bath increases the ionomer mobility, which increases the dissociation of the $-SO_3H$ side chains, thereby improving ionomer/Pt interface. They also showed that the ultrasonic water bath treatment of ionomer resulted in a more extended ionomer distribution with a favourable pore size distribution for mass transfer capacity. Ionomer addition to the catalyst ink also increases the solution viscosity, which has been shown to reduce agglomeration of catalyst clusters (Yang et al., 2021). Pollet and Kocha (2022) showed that ultrasonication at a frequency 20 kHz is optimal for low loading PEMFC electrode preparation. In the current thesis, a combination of high-shear milling and ultrasonication was used consistently for all inks, however it should be noted that the appropriate dispersion method may depend on the specific properties on a catalyst.

### 2.2.3 Properties of the catalyst

The ionomer dispersion in the catalyst layer is affected by the Pt loading of the catalyst. Using contrast-variation small-angle neutron scattering (CV-SANS) Yoshimune and Harada (2019) observed that the ionomer-adsorption layer in the CL had decreased density and increased thickness with increasing Pt loading on carbon. They attributed this to the preferential adsorption of the hydrophobic ionomer backbone to the carbon support. They showed that a 30 wt% Pt/C catalyst layer had a thinner, more dense ionomer shell, compared to the thicker and less dense ionomer shell in a 50 wt% Pt/C catalyst layer. The greater available carbon surface area (and larger Pt-Pt distances) in lower metal loading Pt catalysts allow for facile adsorption of ionomer onto the carbon support. Ionomer/catalyst interaction therefore strongly depends on the composition of the catalyst itself.

There still exists significant debates about the nature and mechanisms of ionomer interaction with solvents, catalyst particles and carbon support. The review by Guo et al. (2021) highlights some of the controversial findings in recent literature. The purpose of this thesis is to understand how catalyst metal loading, solvent composition and ionomer heat treatment will affect the catalyst layer structure.

### 2.2.4 Properties of the ionomer

The ionomer in the catalyst ink may adsorb preferentially to either Pt or Carbon. The hydrophilic -$SO_3H$ side chain groups of the ionomer dissociate in the solvent, becoming negatively charged. These -$SO_3H$ groups adsorb to Pt, whereas the hydrophobic polytetrafluoroethylene ionomer backbone adsorbs to the support (Guo et al., 2021; Yang et al., 2021). Currently it is suggested that the ionomer distribution in Pt/C catalyst layers is heterogeneous consisting of thin films covering carbon agglomerates, as well as larger domains distributed unevenly though the secondary pore structure. This theory is consistent with experimentally observed ionomer aggregates, porous network evolution, and distinct interfaces between the ionomer and separate phases in the CL (Holdcroft, 2014).

The typical support, Carbon black, tends to form agglomerates of carbon particles in the CL, resulting in a bimodal pore size distribution. These *primary* and *secondary* pore sizes are in the order of 2-20 nm and >20 nm respectively, illustrated in Figure 2-4 (Holdcroft, 2014). The primary pore space is thought to be inaccessible to ionomer, which mainly covers the surface of agglomerates and intra-agglomerate pores.

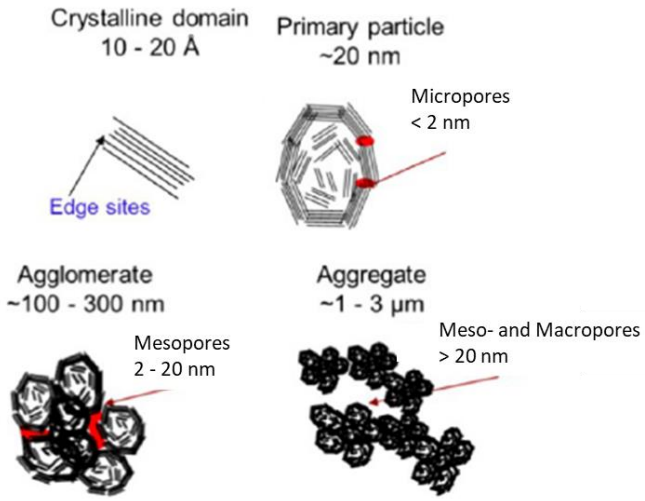


*Figure 2-4: Carbon support aggregates, agglomerates and pore sizes. Adapted from Holdcroft (2014).*

The influence of heat treatment of the ionomer with catalyst inks has not been extensively studied. Itota et al. (2022) investigated the effects of a thermal drying method (TDM) and no drying method (NDM) on the catalyst layer structure,

performance, and durability of MEAs made from Pt supported on Vulcan and Graphitised Vulcan. The TDM consisted of drying the ionomer with the catalyst and solvents to a dry ‘cake’, for 4h at 75°C. They showed that the TDM MEAs had lower charge transfer resistance, improved BOL ECSA, and performance, as well as greater ionomer dispersion and interface with the support, compared to the NDM MEAs. However, the NDM MEAs showed large ionomer/support aggregates, with less ionomer/catalyst interface, which resulted in improved carbon corrosion stability owing to the reduced wettability of the CL. The TDM MEAs retained water to a greater extent, thereby facilitating carbon corrosion. This study showed that there is a benefit for PEMFC performance when ionomer is heat treated with the catalyst, thereby improving the ionomer distribution in the CL, however, this reduces the stability, owing to the increased wettability. There have been no studies reporting on the combination of some heat-treated and non-heat-treated ionomer in the CL.

## 2.3 Ionomer optimisation in MEAs

The ionomer contains both hydrophilic and hydrophobic groups, and therefore plays a key role in water management in a MEA. It has been shown that the amount of proton conducting ionomer in the CL can be optimised to maximise fuel cell performance, ensuring adequate reactant-catalyst interaction, without flooding the MEA (Gatto et al., 2015; Kim et al., 2010; Sasikumar, Ihm and Ryu, 2004; Qi and Kaufman, 2003). This optimal ionomer content depends on catalyst parameters (such as platinum loading, carbon to metal ratio and particle size), as well as fuel cell operating conditions. Ionomer presence in the catalyst layer also confers the benefits of improved catalyst layer mechanical stability, as well as the prevention of membrane dehydration due to the moisture retaining property of these hydrophilic compounds (Kim et al., 2010).

This proton conduction capability is an important factor to consider when optimising catalyst utilisation, as insufficient ionomer may result in isolated catalyst particles, which cannot catalyse the reactions as they do not have access to a proton conducting pathway. Excessive ionomer content, however, can decrease performance by inhibiting electronic conduction paths (between platinum and carbon), thereby acting as an electronic insulator. Similarly, too much ionomer can physically block up gas transport channels in the catalyst layer, increasing mass transport resistance for reactants to reach the catalytic sites (Wang et al., 2019; Orfanidi et al., 2017). The hydrophilic nature of ionomers also means that excess ionomer can cause flooding of the catalyst layer, by retaining too much water, thereby inhibiting oxygen migration/diffusion to the catalytic sites (Kim et al., 2010). The following sections review ionomer optimisation studies across different ionomer types, catalyst loadings as well as the effect of ionomer content on Pt utilisation and ECSA. Table 2-2 summarises findings from ionomer optimisation studies in literature.

*Table 2-2: Catalyst properties and test conditions for selected ionomer optimisation studies*

| Catalyst Supplier | Catalyst metal content (Pt and/or Co wt%) | Support | CL Ionomer | Optimal Ionomer content (wt %) | Current density at 0.6 V ($mA/cm^2$) | CCL Pt loading ($mg_{Pt}/cm^2$) | Relative humidity (%) | Cathode air flowrate | Source |
|---|---|---|---|---|---|---|---|---|---|
| **TKK** | 46.6 % Pt | C | Nafion 1100EW | 32 | ~1200 | 0.4 | 100 | 0.2 L/min | (Xu et al., 2007) |
| **TKK** | 46.6 % Pt | C | Nafion 920EW | 28 | ~1300 | 0.4 | 100 | 0.2 L/min | |
| **TKK** | 46.6 % Pt | C | Nafion 800EW | 25 | ~1400 | 0.4 | 100 | 0.2 L/min | |
| **TKK** | 53.2 wt% $Pt_3Co$ | C | Nafion 1100EW | 28 | ~1400 | 0.2 | 100 | 0.2 L/min | |
| **E-TEK** | 20 wt% Pt | Vulcan XC-72 | Nafion 115 | 50 | ~700 | 0.1 | - | 0.2 L/min | (Sasikumar, Ihm and Ryu, 2004) |
| **E-TEK** | 20 wt% Pt | Vulcan XC-72 | Nafion 115 | 40 | ~700 | 0.25 | - | 0.2 L/min | |
| **E-TEK** | 20 wt% Pt | Vulcan XC-72 | Nafion 115 | 20 | ~550 | 0.5 | - | 0.2 L/min | |
| **E-TEK** | 20 wt% Pt | Vulcan XC-72 | Nafion 1035 | 40 | ~1000 | 0.25 | - | 0.2 L/min | |
| **TKK** | 45.5 wt% Pt | C | Nafion 1100EW | 30 | ~800 | 0.4 | 59 | 1.5 Stoich. Ratio | (Kim et al., 2010) |
| **TKK** | 45.5 wt% Pt | C | Nafion 1100EW | 30 | ~910 | 0.4 | 59 | 2.0 Stoich. Ratio | |
| **TKK** | 45.5 wt% Pt | C | Nafion 1100EW | 30 | ~940 | 0.4 | 59 | 2.5 Stoich. Ratio | |
| **TKK** | 46wt% Pt | C | Aquivion 830EW | 20 | ~1100 | 0.4 | 70 | 2 L/min (pure $O_2$) | (Lei et al., 2011) |

### 2.3.1 Effect of Equivalent Weight on optimal ionomer content

A study by Xu et al. (2007) focused on showing how ionomers with different equivalent weights affect the optimal ionomer content in a PEMFC. They used Nafion ionomers with equivalent weights of 1100, 920 and 800. For each of these ionomers, they were able to clearly show an optimal ionomer content, as evidenced by consistently greater cell voltage at any given current density on a polarisation curve, for the test conditions shown in Table 2-2. Xu et al. (2007) showed that the optimal ionomer contents were 32%, 28%, and 25% for Nafion 1100EW, Nafion 920EW and Nafion 800EW respectively. This indicates that less ionomer is needed to optimise CCLs when using lower EW ionomers. Additionally, the current densities at a cell voltage of 0.6 V increased with the decrease in EW of ionomers used (Table 2-2). The EW of an ionomer is therefore clearly a significant factor in optimisation of PEMFC ionomer content.

Lei et al. (2011), investigated the optimum amount of Aquivion 830EW, using the same TKK 46 wt% Pt catalyst, and 0.4 $mg_{Pt}/cm^2$ loading as Xu et al. (2007). They showed that the optimum Aquivion 830EW amount is 20 wt%, as opposed to the 25 wt % optimum Nafion 800 EW ionomer content in the study by Xu et al. (2007). Equivalent weight of ionomers was also investigated by Li et al. (2020) who showed that the short-side chained Aquivion (720 EW) ionomer compared to the long-side chained Nafion (1100 EW) showed improved performance, ECSA and voltage output, with lower high-frequency resistance.

### 2.3.2 Effect of catalyst layer loading on optimal ionomer content

The work done by Sasikumar, Ihm and Ryu (2004) focused on identifying the relationship between optimum ionomer content and MEA Pt loading (refer to Table 2-2). Using Nafion 115, they were able to show that the optimum ionomer content (at their test conditions) for MEA Pt loadings of 0.1, 0.25, and 0.5 $mg_{Pt}/cm^2$ were 50, 40 and 20 wt% respectively. The current density achieved at cell voltage of 0.6 V was similar for the 0.1 and 0.25 $mg_{Pt}/cm^2$ loadings with the 50 and 40 wt% ionomer contents (about 700 $mA/cm^2$), however, the higher loading MEA 0.5 $mg_{Pt}/cm^2$ with 20 wt% ionomer content showed the lowest performance with only around 550 $mA/cm^2$ achieved at a cell voltage of 0.6V. What the results from this study show is that optimum ionomer content depends directly on the MEA platinum loading. Higher

loadings will require less ionomer, and conversely low platinum loadings (which is the interest of this project) require greater ionomer content.

### 2.3.3 Ionomer content and ECSA

Sasikumar, Ihm and Ryu, (2004) showed that the optimal Nafion content (40 wt%) for the electrode with 0.25 $mg_{Pt}/cm^2$ loading corresponded directly to a maximum ECSA, roughness factor and Pt utilisation, among the tested Nafion contents, as measured by cyclic voltammetry (shown in Table 2-3). Here the ECSA is given as the total surface area (648 $cm^2$), the roughness factor (RF) of 130 is the ratio of the ECSA to the active cell area of 5 $cm^2$, and the utilisation (52%) was evaluated by dividing the RF of the electrode by the theoretical RF (250) for 20% Pt/C, which had a surface area of 100$m^2$/g. These results illustrate the earlier postulated mechanisms of the decrease in performance with excessive ionomer, which is that the actual available ECSA decreases when the excess ionomer starts acting as an electronic insulator, and/or a barrier to mass transport in the catalyst layer. Excess ionomer isolates catalyst particles either from the gaseous phase, or the electron conducting phase, and thereby instead of improving the TPB distribution, hinders it.

*Table 2-3: ECSA, RF and Pt utilisation for CCL wit 0.25 $mg_{Pt}/cm^2$ loading, from study by Sasikumar, Ihm and Ryu, (2004)*

| Nafion Content (wt%) | ECSA ($cm^2$) | Roughness Factor | Pt utilisation (%) |
|---|---|---|---|
| **20** | 266 | 53 | 21 |
| **30** | 628 | 126 | 50 |
| **40** | 648 | 130 | 52 |
| **50** | 586 | 117 | 47 |
| **60** | 457 | 91 | 37 |

## 2.4 PtCo alloy catalysts in the catalyst layer

In this section a review is presented of the recent developments in PtCo research, as well as the effect of PtCo physical and electrochemical characteristics on PEMFC performance and durability.

### 2.4.1 Performance

It has been extensively demonstrated in literature, that PtCo alloys show enhanced ORR catalytic activity compared with pure Pt catalysts (Ramaswamy et al., 2021; Wang and Spendelow, 2021; Garsany et al., 2018; Zignani, Antolini and Gonzalez, 2008; Santiago, Varanda and Villullas, 2007; Toda et al., 1999). According to Ramaswamy et al. (2021) the increased activity of these PtCo catalysts can be attributed to the moderation of binding strength of reaction intermediates and increased efficiency in breaking of the $O_2$ double-bond. This binding moderation effect is caused by the geometric strain induced by sub-surface cobalt, which is referred to as the electronic ligand effect. Bligaard and Nørskov (2007) used Density Functional Theory to show that O and H binding energies increase on Pt, when subsurface Co is present, owing to an upward shift in energy of the Pt d-band center. The hybridization of Pt and Co d-bands results in the d-band shifting closer to the Fermi level, thereby increasing adsorption strength of reaction intermediates, leading to improved catalytic activity.

They showed that a PtCo/C catalyst had 60% higher specific activity (1308 $\mu A/cm^2_{Pt}$), as well as a higher mass activity (0.56 $A/mg_{Pt}$), than a Pt/HSAC catalyst with similar particle size (with specific activity of 797 $\mu A/cm^2_{Pt}$ and mass activity of 0.31 $A/mg_{Pt}$). Stamenković et al. (2002) showed that during PtCo fuel cell operation, a Pt skin forms on the surface of particles, owing to the redeposition of dissolves Pt. This Pt-skin structure on PtCo particles show enhanced intrinsic activity compared to bulk PtCo and Pt catalysts, owing to the electronically modified Pt atoms atop a Co rich core. It has been shown that even at ultra-low loadings, PtCo catalysts in PEMFCs can achieve mass activities greater than the DOE target of 0.44 $A/mg_{Pt}$ (Du et al., 2021). Chong et al. (2018) showed that a PtCo MEA can reach up to 1.77 $A/mg_{Pt}$ at 0.9 V.

The following sections review key findings on the effects of loading, particle size & distribution, morphology, and composition on PtCo performance.

### *2.4.1.1 Loading*

Using a well-established commercial 30 wt % PtCo/C catalyst (Umicore, Elyst Pt30 0670), Garsany et al., (2018) investigated the effects of catalyst loading (at 0.16 $mg_{Pt}/cm^2$, 0.08 $mg_{Pt}/cm^2$, and 0.04 $mg_{Pt}/cm^2$) on performance, on MEAs with 10 $cm^2$ active area. The physical and electrochemical properties of these MEAs are shown in Table 2-4, labelled ac C1, C2 and C3. The polarisation and power density curves from this study are shown in Figure 2-5. A polarisation curve is the standard diagnostic technique for assessing in-situ PEMFC performance. A polarisation curve is a voltage vs current density plot which provides information on the performance losses in a fuel cell under operating conditions. A high performing MEA shows high cell voltage at a given current density. This technique was elaborated on in section 3.3.5. from Garsany et al., (2018), Figure 2-5 shows that the lowest catalyst loading (NRL#3 – blue curve) results in the lowest performance, as indicated by the significant loss of current density in the high current density region. The 0.08 $mg_{Pt}/cm^2$ PEMFC shows comparatively similar performance to the 0.16 $mg_{Pt}/cm^2$ PEMFC, despite having half the loading.

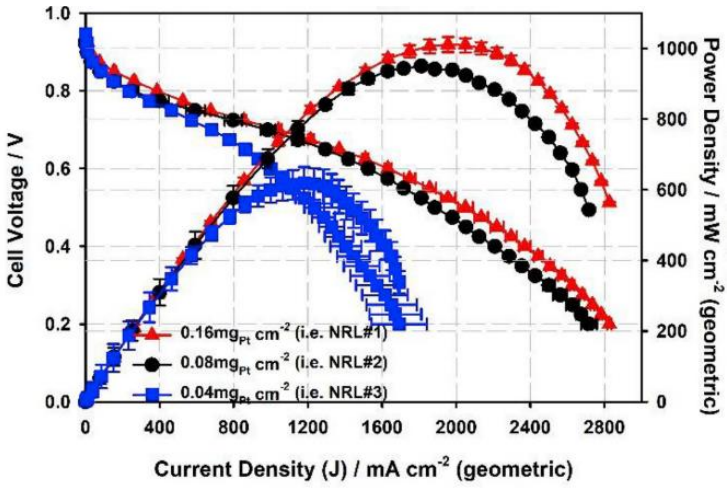


*Figure 2-5: Average I-V polarization and power density curves obtained for PtCo/HSAC (SSC Aquivion®) PEMFCs at different cathode Pt loadings, recorded at a cell temperature of 80 °C, 150 $kPa_{abs}$ back-pressure, adapted from Garsany et al., (2018).*

Given the need to reduce platinum use in PEMFCs the relatively small drop in performance from a 0.16 $mg_{Pt}/cm^2$ to a 0.08 $mg_{Pt}/cm^2$ is a favourable result, especially considering the U.S. DOE goal of reducing the loading of platinum electrocatalysts below 0.125 $mg_{Pt}/cm^2$. Garsany et al., (2018) also show that the large drop in performance for the 0.04 $mg_{Pt}/cm^2$ catalyst is consistent with the increase in the pressure-independent resistance to local oxygen transport on the catalyst layer.

*Table 2-4: Catalyst properties and test conditions for selected PtCo catalyst MEAs*

| | **Catalyst** | | | | | | | |
|---|---|---|---|---|---|---|---|---|
| Catalyst Designation | H | M | L | A | B | C-1 | C-2 | C-3 |
| Supplier & Catalyst designation | RD CAT0023 | Umicore (Elyst Pt30 0670) | General Motors | N/A | EWii Fuel Cells | Umicore, Elyst Pt30 0670 | | |
| Metal loading (wt %) | - | - | - | 30 | 55 | 30 | 30 | 30 |
| Pt:Co ratio | 66:34 | 80:20 | 85:15 | 81:19 | 61:39 | 27:3 | | |
| Cathode loading (mg/cm$^2$) | 0.21 | 0.1 | 0.1 | 0.1 | - | 0.04 | 0.08 | 0.16 |
| ECSA (m$^2$/g) | 41 | 37 | 43 | 42 | 27 | 44 | 44 | 37 |
| Average Particle Size (nm) | 7.0 | 4.4 | 4.5 | 4.5 | 7.0 | - | - | - |
| Mass activity (mA/mg$_{pt}$) | 850 | 700 | 780 | 560 | - | - | - | - |
| Specific Activity (mA/cm$^2$) | - | - | - | 1.308 | - | - | - | - |
| Predominant morphology | Porous | Crystalline | Crystalline | Crystalline | Porous | Crystalline | | |
| Support | HSAC | HSAC | HSAC | HSAC | HSAC | HSAC | | |
| Ionomer | - | - | - | - | - | Aquivion 830EW | | |
| Ionomer content (wt %) | - | - | - | - | - | 27 | 27 | 27 |
| | **Test conditions** | | | | | | | |
| Test cell Area (cm$^2$) | 50 | 50 | 50 | 5 | 47.6 | 10 | 10 | 10 |
| Cell temperature (°C) | 80 | 80 | 80 | 80 | - | 80 | 80 | 80 |
| Cell Pressure (atm) | 1 | 1 | 1 | 1 | - | 1 | 1 | 1 |
| Relative Humidity (%) | 100 | 100 | 100 | 100 | - | 100 | 100 | 100 |
| Hydrogen Flow rate (cm$^3$/min) | 200 | 200 | 200 | 200 | - | Stoichiometric ratio of 2 | | |
| Nitrogen flowrate (cm$^3$/min) | 75 | 75 | 75 | 200 | - | - | - | - |
| Source | (Papadias et al., 2018) | | | (Ramaswamy et al.,2021) | (Sneed et al., 2018) | (Garsany et al., 2018) | | |

Thinner cathode catalyst layers (as is the case in the 0.04 $mg_{Pt}/cm^2$ catalyst) are more prone to flooding, especially at lower current densities where water production is high. A film of water is therefore produced which prevents oxygen diffusion to the catalytic site, thereby impeding performance (Garsany et al., 2018).The lowest MEA loading is therefore limited by water management and reactant mass transfer effects, as well as durability. The goal is to design a low loading MEA by reducing the Pt loading as much as possible, to reduce cost, but not to limit performance and durability.

#### *2.4.1.2 Particle size and distribution*

According to Wang et al. (2015) the mass activity of a catalyst used for the ORR is inversely proportional to the particle size, whereas the specific activity is independent of particle size. Wang et al. (2015) also indicate that a narrow particle distribution with smaller particles, resulted in an increase in ORR activity. While smaller particles are favoured due to their improved performance, very small particles (less than 2 nm in diameter) are prone to agglomeration during fabrication. An appropriate particle size range has been suggested to be between 2 and 5 nm.

#### *2.4.1.3 Particle Morphology*

The ORR, like most electrochemical reactions, is site-dependent and structure-sensitive, according to Wang et al. (2015). The structure and shape of PtCo nanoparticles therefore have a significant effect on the electrochemical properties of the catalyst layer in MEAs. However, owing to the complexity of experimental preparation in order to manipulate and test various theoretical shapes, little work has been done on shape-controlled catalysts compared to the amount of research on traditional spherical particles.

Bing et al. (2010) provided a review comparing the ORR activity of different crystallographic planes in platinum nanoparticles. They explain that the surface energies of low-index crystallographic planes of the face-centred cubic crystal structure of platinum increase in the following order: $\gamma$ {111} < $\gamma$ {100} < $\gamma$ {110}. Bing et al. (2010) show that there existed conflicting results concerning the optimal crystallographic morphology in terms of catalytic activity. However, what is clear is that the thermodynamically favoured shape of platinum nanoparticles is spherical, with low index facets at the particle surface, such as Pt{100} and Pt{111} (Bing et al., 2010).

#### *2.4.1.4 PtCo alloy composition*

In addition to the benefits in reduced cost, PtCo alloy catalysts have altered electronic and adsorption properties. It has been shown extensively and consistently, that PtCo/C catalysts had superior performance and durability when compared to Pt/C catalysts (Ramaswamy et al., 2021; Garsany et al., 2018; Kim et al., 2010; Zignani, Antolini and Gonzalez, 2008; Xu et al., 2007). However, the exact optimal Pt:Co ratio is still under debate. According to Bing et al. (2010) PtM/C (M = Co, Cr, Fe, Ni and Mn) alloy catalyst has higher activity and stability at a 3:1 ratio. Others have suggested that 1:1 is the optimal ratio (Wang et al. 2015). It has been shown that PtCo alloy catalysts may be induced to have a 'Pt-skin', consisting of 100% Pt, compared to bulk PtCo, which is 75 mol % Pt. This skin has shown enhanced catalytic activity, compared to bulk PtCo, as well as Pt (Bing et al., 2010; Stamenković et al., 2002). Zignani, Antolini and Gonzalez (2008) shows that during accelerated stress tests in PtCo catalysts, this Pt skin arises spontaneously due to the dissolution and surface depositions of Pt species.

### 2.4.2 MEA durability

#### *2.4.2.1 PtCo Degradation mechanisms*

PtCo catalysts are susceptible to both chemical degradation, from the acidic environment created by PFSA membranes, as well as electrochemical degradation from being exposed to high potentials. These degradation mechanisms result in a loss of fuel cell performance over time. Ramaswamy et al., (2021) provided a useful categorisation for the reasons of cathode catalyst layer (CCL) performance loss as a result of degradation. The categories are as follows:

1. Decrease in ECSA due to particle size growth.
2. Decrease in intrinsic catalytic activity due to Cobalt leaching.
3. Contamination of membrane from leached $Co^{2+}$ cations
4. Local transport resistance from Pt redistribution in the carbon support

The predominant mechanisms of particle growth are Ostwald ripening and Pt-band formation. Ostwald ripening in PtCo catalysts is the phenomenon where Pt dissolves from smaller particles and becomes redeposited on larger particles; whereas Pt-band formation occurs when Pt dissolves and is deposited in the membrane itself. Particle

growth also occurs, to a lesser extent, due to particle migration and coalescence from smaller particles to larger particles, however it has been suggested that this is limited to catalysts with graphitised carbon support (Ramaswamy et al., 2021).

Cobalt leaching is responsible for not only a decrease in intrinsic catalytic activity, but also a contamination of the PFSA membrane. The contamination of the PFSA membrane occurs by $Co^{2+}$ cations ion-exchanging with the sulphonic-acid functional groups. Unlike Pt dissolution, which occurs largely at potentials exceeding 0.7 V, Co dissolution occurs at any potential exceeding 0.1 V. Cobalt acts as a sacrificial anode, being oxidised and leached before Pt or carbon can be affected, thereby conferring some degree of protection against Pt and Carbon corrosion (Nikkuni et al., 2015). However, the selective loss of Co results in a loss of the favourable geometric strain and ligand effects caused by subsurface Co; effectively transforming the properties of the degraded catalysts closer to that of pure platinum.

The benefit of PtCo alloy catalysts over Pt catalysts in terms of performance are clear, and have been discussed above, however, as has been mentioned, PtCo generally cannot compete in terms of particle degradation stability. The work by Ramaswamy et al demonstrate the differences in particle stability between PtCo and pure Platinum catalysts used in PEMFCs. In their work, they compared catalyst durability of Pt-HSAC and PtCo-HSAC catalysts using 5 $cm^2$ MEAs with cathode loadings of 0.1 $mg_{Pt}/cm^2$. In order to eliminate particle-size effects, the catalysts were heat-treated to produce particles of similar size (~ 4.5 nm). They showed that at BOL, the PtCo/HSAC catalyst had improved kinetics compared to the Pt/HSAC catalyst, however, after 30 000 particle stability cycles ( between 0.6 V and 0.95 vs RHE ), The PtCo/HSAC catalyst lost most of the kinetic benefit. The decrease in activity is due to strain relaxation cause by Co leaching, as described previously. Furthermore, it was observed that the PtCo/HSAC catalyst experienced drastic losses in cell voltage at current densities greater than 1.5 A $cm^2$ (End of life voltage at 2.5 A $cm^2$ is 200 mV lower than BOL voltage), compared to the modest drop in high current density voltage of the Pt/HSAC catalyst (voltage at 2.5 A $cm^2$ only 115 mV lower than BOL). This demonstrates the effect that the Co contamination of the membrane has on mass transport related losses in performance for PtCo catalysts compared to pure Pt (Ramaswamy et al., 2021).

Zignani, Antolini and Gonzalez (2008) show similar results when they compared the durability of PtCo and Pt in half cell environments by subjecting 0.4 mg/cm$^2$ loaded GDEs to 1000 potential cycles between 0.5 V and 1.0 V vs. RHE. As expected, the ORR activity of the fresh PtCo GDEs was greater than that of the pure Pt samples, however, after repetitive potential cycling (RPC), the ORR performance of the PtCo GDEs were no better than that of the spent Pt samples. They found that repetitive cycling resulted in Pt and Co dissolution in the PtCo samples, with Pt redeposition creating a Pt skin on PtCo particles. After RPC the difference between the PtCo and Pt ORR activities could be accounted for by only their difference in particle sizes.

While PtCo catalysts have been shown to have a larger reduction in activity compared to Pt catalysts in MEA particle stability testing, the protective role of Co as a sacrificial anode ensures minimal changes in ECSA during particle stability testing. Ball et al. (2006) showed that the ECSA of two different PtCo catalysts remained unchanged during both in-situ and ex-situ particle stability testing, compared to a significant drop in ECSA for a pure Pt catalyst.

#### *2.4.2.2 Carbon Corrosion*

In addition to the dissolution, detachment and agglomeration of PGM particles, the carbon in CCLs is also harshly affected by the electrochemical environment in PEMFCs. Carbon corrosion and PtCo degradation are distinct phenomena, however, they are not independent. PGM clusters accelerate carbon oxidation, which, in turn, results in compromised particle structural support, leading to further PtCo detachment an agglomeration. Currently, carbon corrosion and PGM particle degradation are rarely studied in conjunction. It is instead common practice to perform Accelerated Stress Tests (in RDE or MEA applications) for these two phenomena separately. Carbon corrosion is studied by performing ASTs in the voltage range of 1.0 V to 1.5 V, with 5000 triangle sweeps, whereas PGM particle degradation uses a range of 0.6 V to 0.9 V (Du et al., 2021).

Hu et al. (2021) proposed a three-stage classification for the distinct occurrences in the CL during carbon corrosion testing. In the first stage, in the absence of carbon corrosion, the micropores in the catalyst layer are open, the catalyst layer itself is complete, with good mass transfer capacity. In stage two carbon support corrosion results in slight particle loss, while mass transfer performance remains unchanged.

Micropores become progressively larger and supporting structure thinner with a reduction in triple phase boundary, but little loss of performance and ECSA occurs here. In the third and final stage the increasingly fragile support structure becomes unable to support the packing force. The catalyst layer abruptly collapses, filling micropores and leaving a dense mass of support. This is associated with a sharp drop in ECSA and performance.

Stariha et al. (2018) showed that under harsh carbon corrosion testing (Cycling between 1.0 V and 1.5V), there was little particle growth and minimal cobalt leaching (using a PtCo/HSAC catalyst MEA), however cross sectional TEM imaging showed significant loss of catalyst layer thickness (7.0 µm at BOT, 6.0 µm after 500 cycles and 2.9 µm after 1000 cycles), which resulted in significant losses in performance, associated with mass transport limitations. Du et al. (2021) observed the same phenomenon, following a carbon corrosion AST, where there was a significant loss in CL thickness (6.1 to 2.7 µm), with only a slight increase in particle size (4.0 to 4.8 nm). They postulate that the loss in performance was primarily due to loss in oxygen mass transfer capacity following the thinning and collapse of the catalyst layers. However, the collapse in structure also resulted in a change in hydrophobicity, which would impact on the ionomer orientation, resulting in compromised water management, to the detriment of performance. Lastly the ionic pathway would also be adversely affected, reducing the number of viable triple-phase boundary active sites (Du et al., 2021).

Du et al. (2021) have also shown that the physical properties of the carbon support greatly influence the degree and rate of carbon corrosion. They showed that a High-Surface-Area-carbon (HSAC) ( 800 $m^2/g$ ) with low degree of graphitisation, exhibited a greater rate of carbon corrosion than Vulcan carbon ( 250 $m^2/g$ ), while a graphitised Low-Surface-Area-carbon (LSAC) ( 150 $m^2/g$ ) had the lowest carbon degradation rate of all three supports. As expected, though, the Pt/LSAC showed much lower initial performance than the other two supported catalysts, owing to the poor dispersion of catalyst on the hydrophobic support with much fewer defects. In addition to graphitisation and surface area, the orientation and porosity of the support also impacts on the rate of carbon degradation. Supports with larger pore area allow for accelerated degradation through ease of diffusion of oxidants. In-planar graphitic sheets are more protected from degradation than exposed edge sites (Du et al., 2021).

## 2.5 Ties to project

The literature presented here has informed the investigations in the following chapters of this thesis in order to address the stated objectives and achieve the goal for the design of a high performing low PGM PtCo MEA.

From the literature review it has been shown that the activity and durability of PtCo and Pt catalysts are affected by their morphology, composition and particle size. In section 4.1 of this thesis, these characteristics will be determined for two PtCo catalysts and a Pt benchmark using physical and electrochemical characterisation techniques. This addressed the first objective of the thesis. The literature review has shown that the optimal ionomer content in an MEA CL depends on multiple factors including the equivalent weight of the ionomer and the Pt loading on the CL. The polarisation curves and ECSAs are the key parameters for determining the optimal ionomer content. Ionomer optimisation studies for two PtCo catalysts (which differ notably in metal/carbon ratio) are presented in section 4.2, thereby addressing the second objective. Across section 4.1 and 4.2 -ex-situ and in-situ performance and durability results were used to determine the best performing MEA, which is the third objective. Lastly, literature has shown that heat treatment of ionomer with the catalyst during ink during for MEA fabrication improves porosity, ionomer/catalyst interface and charge transfer properties in the CL, thereby improving performance. However, non-heat-treated ionomer has shown improved stability during carbon corrosion ASTs. In section 4.3 of this thesis, the effects of heat treatment and partial heat treatment of ionomer was investigated in terms of MEA performance and durability.

# 3 Experimental

The following chapter outlines the experimental procedures which were followed to complete the project. The experimental work is categorised in four sections, namely: physical characterisation, ex-situ catalyst electrochemical characterisation, in-situ performance evaluation, and MEA preparation and characterisation. This is summarised in the schematic shown in Figure 3-1.

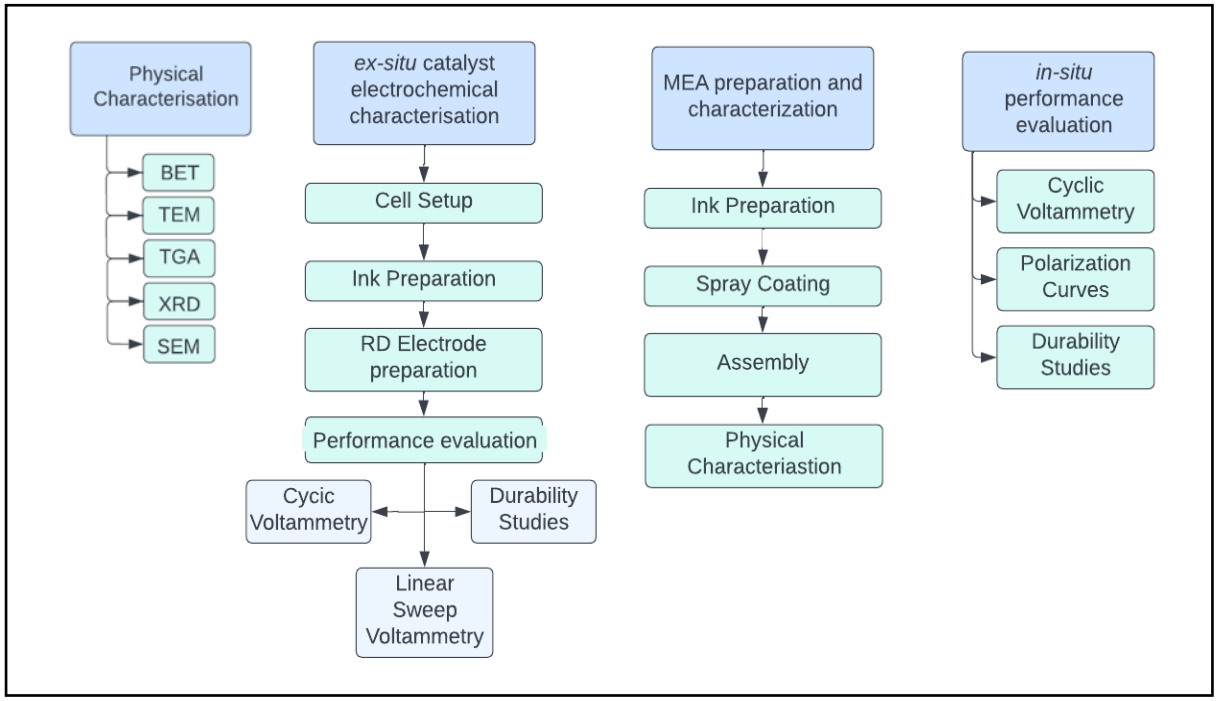


*Figure 3-1: Diagram of experimental plan layout*

The materials used in this work are summarised in Table 3-1. The two commercial catalysts investigated were the Umicore Elyst Pt30 0690 (PtCoU30) and TKK TEC36F52 (PtCoT50) catalysts, with detailed specifications shown in Table 3-1. Both catalysts are supported on High Surface Area Carbon (HSAC) but differ in metal loadings (30 wt% for PtCoU30 and 52 wt% for PtCoT50). The nominal Platinum to Carbon molar ratio is the same for both catalysts (3:1). The Platinum catalyst used for comparison was an in-house benchmark, heat treated 40 wt% Pt catalyst. These three catalysts were used as cathode materials, whereas the GV40 catalyst was consistently used for anode. The ionomer used for MEA preparation is the Aquivion D72-25BS, which is a low equivalent weight (720 EW) short-side chained ionomer. Catalyst inks

were prepared using this ionomer, water and isopropanol as solvents. The materials used for assembling/gasketing the MEAs are also listed in Table 3-1.

*Table 3-1: List of Materials and Suppliers*

| **Catalyst Materials** | | **Supplier** |
|---|---|---|
| Elyst Pt30 0690 | 30 wt% PtCo/C | Umicore |
| TEC36F52 | 52 Wt% PtCo/C | TKK |
| PtH40 | 40 wt% Pt/C | Mintek |
| GV40 (anode catalyst) | 40 wt% Pt/C | Mintek |
| **Catalyst Ink Materials** | | **Suppliers** |
| Aquivion D72-25BS | 28 wt % ionomer solution | Fuel Cell store |
| Deionised water | Resistivity > 15 MΩ.cm | Elix Milipore |
| Isopropanol | 99.8 % | Science World |
| **MEA Materials** | | **Suppliers** |
| Double sided adhesive | 37 µm PET film | HyPlat |
| Silicone seal | 74 µm PanocProtect PET film | HyPlat |
| Subgasket | 32 µm PET laminating film | HyPlat |
| Membrane | Nafion Gore M735, 18 | Gore |
| Gas diffusion layer | AvCarb MB30 | Fuel Cell Store |

## 3.1 Catalyst physical characterisation

### 3.1.1 Brunauer-Emmet-Teller surface area

The Brunauer-Emmett-Teller (BET) method was used to determine the surface areas of catalyst materials by $N_2$ physisorption. This technique was developed by Brunauer, Emmett and Teller (1938), and works on the principle of physical adsorption of an adsorbate (such as $N_2$) on a solid sample. The assumptions underlying this technique are that multilayer adsorption occurs, where the first layer of adsorption follows Langmuir adsorption pattern and subsequent layers behave as gas condensation on a liquid layer. The heat of adsorption of the first layer is therefore distinct. Using the known diameter of the adsorbate molecule, the surface area of the solid is calculated from the mass of the monolayer of adsorbate. In the present work, this technique was performed on a TriStar II 3020 (Micrometrics) device at the University of Cape Town. 200 mg of catalyst was loaded into sample holders, which were degassed for approximately 15 hours, before liquid $N_2$ was used as the analysis adsorptive. Surface area is reported in $m^2/g_{catalyst}$.

### 3.1.2 Transmission Electron Microscopy

Transmission Electron Microscopy (TEM) was used to determine the average catalyst particle sizes, particle size distribution, as well as morphological phenomena of the catalyst materials of interest in this work. TEM works by emitting a high voltage beam through an ultrathin sample, which is housed in a vacuum chamber. The high voltage beam is focused onto the sample by passing through an electromagnetic objective lens. Electrons pass through the sample and are detected on a fluorescent screen. This produces an image, which can be photographed and analysed. For the present work TEM was done by mixing the catalyst with acetone, sonicating the mixture, and applying it to a copper coated grid for analysis at the University of Cape Town using the F20-FEI Tecnai electron microscope at 200 kV. The resulting images were analysed using imageJ software.

### 3.1.3 Thermogravic Analysis

Thermogravic Analysis (TGA) was performed to determine the total metal content (wt%) in the catalyst materials. The Mettler-Toledo TGA/SDTA851e Thermogravic analyser was used at the University of Cape Town. The carbon support was fully oxidised, with only the metal content remaining after 600° C. The change in weight of the sample was measured as a function of time, as the temperature of the sample is steadily increased.

A sample of 2 to 10 mg of catalyst was placed into an aluminium oxide crucible. The sample temperature was increased at a rate of 10°C/min from 25°C to 900°C, in an atmosphere of synthetic air, flowing at a rate of 10 ml/min.

### 3.1.4 X-Ray Diffraction

X-Ray Diffraction (XRD) was used to determine the catalyst particle crystallite sizes, and PtCo metal phases. XRD is a non-destructive analysis technique, where X-rays are generated and directed towards a crystalline sample from electrically charged particles. When these X-rays interact with a crystalline nanomaterial a diffraction ray is produced, which is then detected and counted. The intensity and angle of diffraction of these rays are plotted to produce a diffraction pattern, which can then be used to identify the crystalline phase of the material by comparing to a crystallographic database. The shape and sizes of the diffraction peaks can also be used to identify

properties of the material; for example, broader peaks represent larger crystallites, whereas sharper peaks indicate smaller crystallites.

In the present work the catalyst sample was radiated with a Co-K$\alpha_1$ radiation source, at a scan rate of 2.5°/min from 20° to 120° (2θ), operating at voltage and current of 35 kV and 40 mA respectively, on a Bruker D8 Advance diffractometer. The volume weighted crystallite size was determined from the Sherrer equation, shown in Eq. 3.1

$$D_v = \frac{\mathrm{K}\lambda}{(\beta \cos\theta)} \qquad 3.1$$

Where: $D_v$ is the volume weighted crystallite size, K is the shape factor (unitless, assumed to be 1), λ is the X-Ray wavelength (which is 1.79 Angstrom from a Cobalt source), $\beta$ is the Full-Width-at-Half-Maximum (FWHM) at a specific angle $\theta$ (both in radians) after the instrument broadening contribution has been subtracted.

### 3.1.5 Energy Dispersive X-ray Spectroscopy

The Energy Dispersive X-ray Spectroscopy (EDS) technique was used to determine the Pt:Co ratio in the alloy catalysts. Catalyst samples were deposited onto a carbon substrate and analysed using the FEI Field Emission Nova NanoSEM 230 device, fitted with an Oxford X-Max detector and INCA software, at 30 kV, at the Electron Microscopy unit at the University of Cape Town.

## 3.2 *Ex-situ* electrochemical characterization

### 3.2.1 Three electrode cell setup

Electrochemical characterization was performed on a standard 3-electrode setup (Gamry instruments), with a SP-300 bipotentiostat (Biologic Science Instruments) and a Gamry rotation control device, all shown in Figure 3-2. The three electrodes were the platinum mesh counter electrode (CE), a $Hg/HgSO_4$ reference electrode (RE), and a glassy carbon working electrode (WE) (Figure 3-2). Before each experiment, the platinum RE was cleaned of impurities with a blowtorch flame and rinsed with DI water. The reversible hydrogen electrode (RHE) potential of the RE was measured against the CE in a hydrogen saturated 0.1 M $HClO_4$ electrolyte environment, using a voltmeter (approximately 0.73 V). The working electrode was polished and prepared, as described in section 3.2.3. All RDE experiments were performed in a 0.1 M $HClO_4$ electrolyte solution. The glassware was cleaned regularly between experiments.

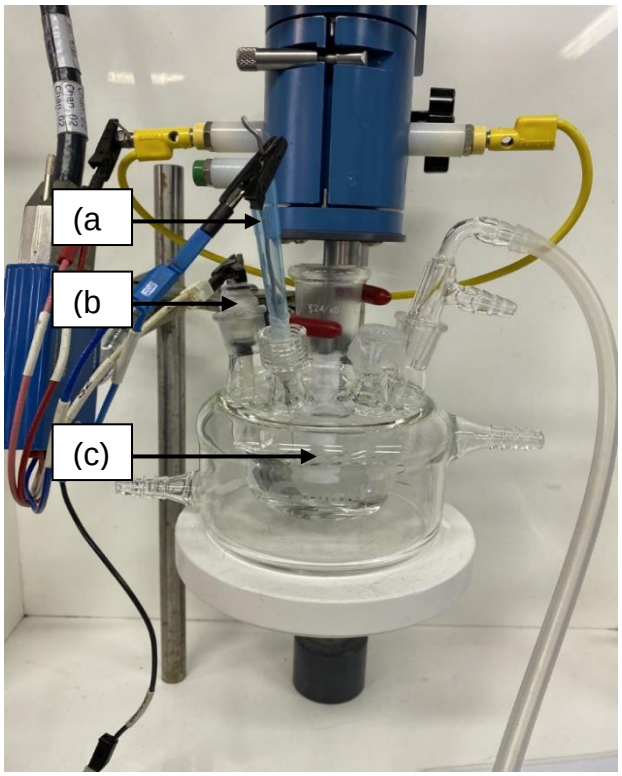


*Figure 3-2: Gamry instruments 3-electrode setup with (a) Pt mesh counter electrode, (b) $Hg/HgSO_4$ reference electrode and (c) glassy carbon working electrode.*

### 3.2.2 Ink preparation for RDE

To produce a thin film on a working electrode with a reproducible, smooth surface, the viscosity, dispersion, and solid content of the catalyst ink was essential. The ink formulation was based on the work done by Kocha et al. (2017), where a 3:1 ratio of deionised water to isopropanol solvent was used.

In a clean vial, 4.2 mg of dry catalyst was measured. The vial was placed in an ice bath before 7.6 ml of deionised water was added, followed by 2.4 ml of isopropanol and 40 μl of 5 wt% Nafion solution. The vial was covered with parafilm, labelled, and sonicated in a large beaker containing ice for 30 minutes. A new ink dispersion was used to produce each working electrode. The working electrode Pt loadings are shown in Table 3-2.

*Table 3-2: Working electrode catalyst loadings used in RDE testing.*

| Catalyst | Catalyst mass on WE surface (mg) | Nominal Pt content (wt %) in catalyst | Pt loading on working electrode ($mg_{Pt}/cm^2$) |
|---|---|---|---|
| **Umicore** | 4.2 | 30 | 0.00620 |
| **TKK** | 4.2 | 52 | 0.0107 |
| **PtH40** | 4.2 | 40 | 0.0087 |

### 3.2.3 Electrode preparation

The same WE electrode was used for all RDE experiments to eliminate potential discrepancies between equipment pieces. The electrode is prepared before each set of experiments by polishing the surface. First a 6 μm polycrystalline diamond suspension was used as lubricant to polish the electrode surface, by scraping the electrode in a figure-8 motion on a grinding sheet. The electrode was rinsed with DI water, and the process was repeated using a slurry made from 1.0 μm Alumina powder (MicroPolish Buehler) and DI water. In the final polishing step was done with 0.05 μm Alumina powder (MicroPolish Buehler) in a similar manner. The glassy carbon surface was submerged in a vial of water, and sonicated for 10 minutes, followed by another 10 minutes of sonication in isopropanol. Once the electrode was rinsed with DI water and blotted dry, it was coated with the catalyst layer. 10 μl of the prepared ink was carefully deposited onto the dry electrode. The electrode was placed under a large beaker, in an upright position, and dried in an oven at 70°C. Only smooth even thin films were considered for analysis.

### 3.2.4 Cyclic voltammetry

The purpose of Cyclic Voltammetry (CV) was to determine the Electrochemical Surface Area (ECSA) of each catalyst and to condition and electrochemically clean the catalyst layer of impurities.

Figure 3-3 shows a typical Cyclic voltammogram for a Pt-based electrocatalyst in an Argon saturated $HClO_4$ solution. In the Hydrogen regime (at voltages lower than 0.3 V), during the cathodic sweep, Hydrogen adsorbs reversibly onto the Platinum surface. During the anodic sweep, the deposited $H^+$ions are oxidised into the acidic electrolyte. This region of the CV is utilised to calculate the ECSA of the catalyst.

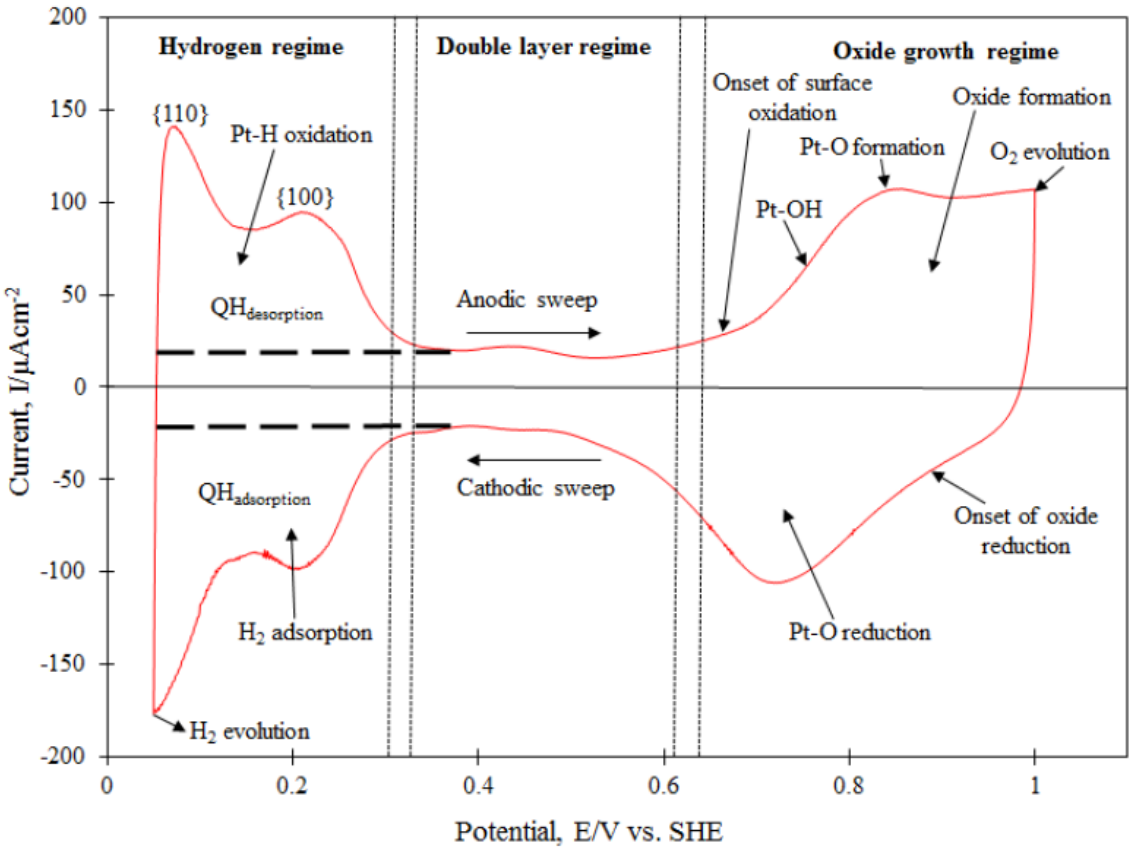


*Figure 3-3: Cyclic Voltammogram for Pt-based catalyst in Argon and $HClO_4$ solution. Adapted from (Juodkazis et al., 2013)*

In the present work, CV was performed in the following way: first, argon gas was bubbled through the 0.1 M $HClO_4$ electrolyte solution in the 3-electrode setup. The WE was attached to the motor and submerged into the electrolyte, taking care to prevent bubbles from forming on the catalyst layer. EC-lab software was used to run a test script, which cycled between 0.05 V and 1.2 V vs. RHE at a scan rate of 100 mV/s for

100 cycles (or until the current response stabilised). The scan rate was reduced to 20 mV/s, and the potential was swept between 0.05 V and 1.2 V vs. RHE for 5 cycles, from which the ECSA was determined. The ECSA was determined by integrating the area under the curve for the hydrogen underpotential deposition ($H_{udp}$) region of the voltammogram, assuming a 210 μC/$cm^2_{Pt}$ monolayer hydrogen charge, and using this in equation 3.2 below.

$$ECSA\left(\frac{cm^2_{Pt}}{g_{Pt}}\right) = \frac{charge\ (\mu C)}{210\left(\frac{\mu C}{cm^2_{Pt}}\right)\cdot catalyst\ loading\ (g_{Pt})} \qquad 3.2$$

### 3.2.5 Linear sweep voltammetry

Linear sweep voltammetry (LSV) was used to determine the Oxygen Reduction Reaction (ORR) activity of the various catalysts. Figure 3-4 shows a typical ORR current-potential curve obtained for a Pt based catalyst on a glassy carbon rotating disk electrode. The purpose of this technique is to determine catalyst kinetic activity towards ORR, by controlling mass transfer to the electrode surface.

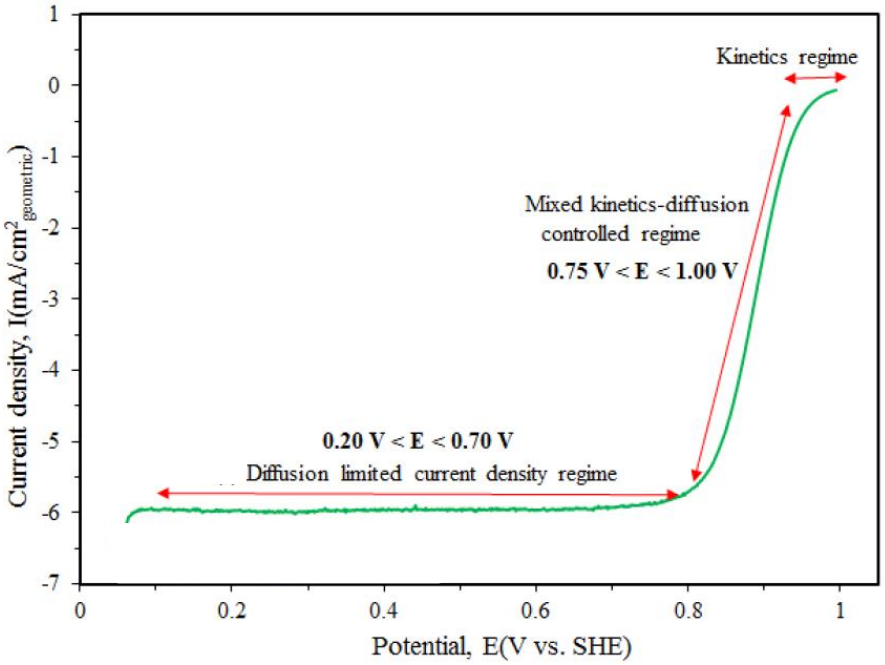


*Figure 3-4: Typical ORR current-potential curve, recorded at 1600 rpm for Pt/C film on glassy carbon disk electrode in Oxygen saturated 0.1M $HClO_4$ solution. Adapted from (Garsany et al., 2010)*

When a catalyst coated electrode is rotated in an electrolyte, the bulk liquid surrounding the electrode is well-stirred by convection, however, a thin film of the

solution will rotate with the electrode. This is called the hydrodynamic layer. Withing this hydrodynamic layer a diffusion layer exists on the electrode, which is not influenced by convection. This diffusion layer thickness depends on the rotation speed of the electrode. By controlling the thickness of this stagnant layer, the diffusion limited current density can be studied by LSV, when potential is applied to the electrode.

For the present work, LSV was performed on conditioned electrodes in an oxygen saturated environment. Oxygen gas was bubbled through the $HClO_4$ electrolyte solution for 20 minutes. Anodic and cathodic potential sweeps were performed at a scan rate of 10 mV/s in the potential windows of 0 V to 1.2 V vs. RHE. These potential sweeps were performed while the electrode was in rotation mode, at 400 rpm, 900 rpm, 1600 rpm and 2500 rpm. The mass activity and specific activity were determined from the cathodic sweep performed at 1600 rpm, using the Koutecký–Levich equation shown in equation 3.3 bellow.

$$\frac{1}{i} = \frac{1}{i_k} + \frac{1}{i_d} \qquad 3.3$$

Here, $i$ is the measured current density, $i_k$ is the true kinetic current density and $i_d$ is the diffusion limited current density. This equation can be rewritten with the kinetic current as the subject of the equation, as shown in equation 3.4.

$$i_k\left(\frac{mA}{cm^2}\right) = \frac{i\left(\frac{mA}{cm^2}\right) \times i_d\left(\frac{mA}{cm^2}\right)}{i_d\left(\frac{mA}{cm^2}\right) - i\left(\frac{mA}{cm^2}\right)} \qquad 3.4$$

The mass-specific activity ($i_m$) and area-specific activity ($i_s$) are commonly determined from the measured current at a voltage of 0.90V. These values are used to benchmark the activities of catalysts used for ORR. The activities for the catalysts in this study were calculated using equations 3.5 and 3.6.

$$i_m\left(\frac{A}{mg_{Pt}}\right) = \frac{i_{k(0.9V)}\left(\frac{A}{cm^2}\right)}{L_{Pt}\left(\frac{mg_{Pt}}{cm^2}\right)} \qquad 3.5$$

$i_m$ is the mass activity, $i_{k(0.9V)}$ is the kinetic current, determined at a voltage of 0.9 V, and $L_{Pt}$ is the platinum loading on the working electrode surface.

$$i_s\left(\frac{mA}{cm^2}\right) = \frac{i_m(\frac{mA}{mg_{Pt}})}{ECSA(\frac{cm^2}{mg_{Pt}})} \qquad 3.6$$

$i_s$ is the specific activity, determined by normalising the mass activity by the electrochemical surface area of the catalyst.

### 3.2.6 Durability studies using accelerated stress tests

Ex-situ durability was determined using accelerated stress tests (ASTs) in the 3-electrode setup by rapidly cycling between specific potential ranges to simulate platinum and carbon degradation mechanisms.

Argon gas was bubbled through the cell for 20 minutes. The electrode was conditioned by cycling between potential range of 0.0 V and 1.2 V vs RHE for 50 cycles. For the carbon support AST, the potential was cycled between 1.0 V and 1.5 V vs RHE for a total of 6000 cycles. CVs were recorded periodically to determine the ECSA loss. CVs were recorded after every 10 cycles from cycle 0 – 100; every 100 cycles from cycle 100 – 1000; every 1000 cycles from cycle 1000 – 6000.

The catalyst durability AST was performed by cycling the potential between 0.6 V and 0.9 V vs RHE for 6000 cycles. CVs for the ECSA was recorded at intervals similar to the carbon corrosion AST.

The durability of the support and catalyst was determined by the rate of degradation observed in a plot of the ECSA loss versus the potential cycle.

## 3.3 *In-situ* electrochemical characterization

### 3.3.1 Ink preparation

Automated (proprietary) spreadsheets were used to calculate the required mass of ionomer, catalyst, deionised water, and isopropanol required to achieve inks with the desired ionomer to catalyst weight ratio. The general procedures were as follow.

a) An ink prepared with ionomer in a single phase. All the ionomer was dried in into an ionomer/catalyst powder. This was called 1-phase ink preparation.
b) An ink prepared in which a portion of the ionomer is dried with the catalyst and the second portion of ionomer was added with the solvents. This was called 2-phase ink preparation.

#### *3.3.1.1 The catalyst/ionomer powder, single phase ionomer ink*

A required amount of ionomer was added to a clean and weighted beaker. In a separate beaker, the required amount of deionised water is weighed. Water was added to the ionomer, the beaker was covered and sonicated for 20 minutes. A required amount of catalyst was weighed and added to the sonicated water and ionomer mixture and swirled to produce a suspension. This catalyst suspension was covered and sonicated at room temperature for 1 hour. The suspension was dried in an oven for, approximately 24 hours, at 75°C until the resulting powder was 99.9% dry. The dryness was determined by weighing the dried cake. The dried cake was crushed in a mortar and pestle. Water and IPA were added to the catalyst powder in a 1:1 ratio for the Umicore, HTRK40 and GV40 catalysts, and a 1:3 ratio for the TKK catalyst. Water was added first, followed by dropwise addition of IPA using a funnel.

#### *3.3.1.2 2-phase ionomer ink*

For a 2-phase ionomer ink, the second portion of ionomer was added after the drying of the catalyst/ionomer powder. The second portion of ionomer was not heat treated and was considered in a separate ‘phase’. During ionomer optimisation trials, ionomer was progressively added to the primary catalyst/ionomer ink to reach the required ionomer wt % intervals. Substrates sprayed with this ink were referred to as 2-phase MEAs, GDEs, etc.

### 3.3.2 Electrode preparation

A PRISM Ultra-Coat 300 device was used to produce Catalyst Coated Membranes (CCMs) and Gas Diffusion Electrodes (GDEs). The CCMs were used for performance and durability testing, SEM imaging, as well as microporous intrusion porosimetry; the and the GDEs were used to study the gas permeability of the catalyst layer.

Immediately after the catalyst ink was prepared, it was loaded into the sprayer syringe. The CCMs were sprayed to produce an active area of 50 $cm^2$ (7.1 cm x 7.1 cm), whereas GDEs were sprayed on active areas of 121 $cm^2$ (11 cm x 11 cm). Figure 3-5 shows the spraying pattern and dimensions for the CCM (a) and the GDE sheets (b).

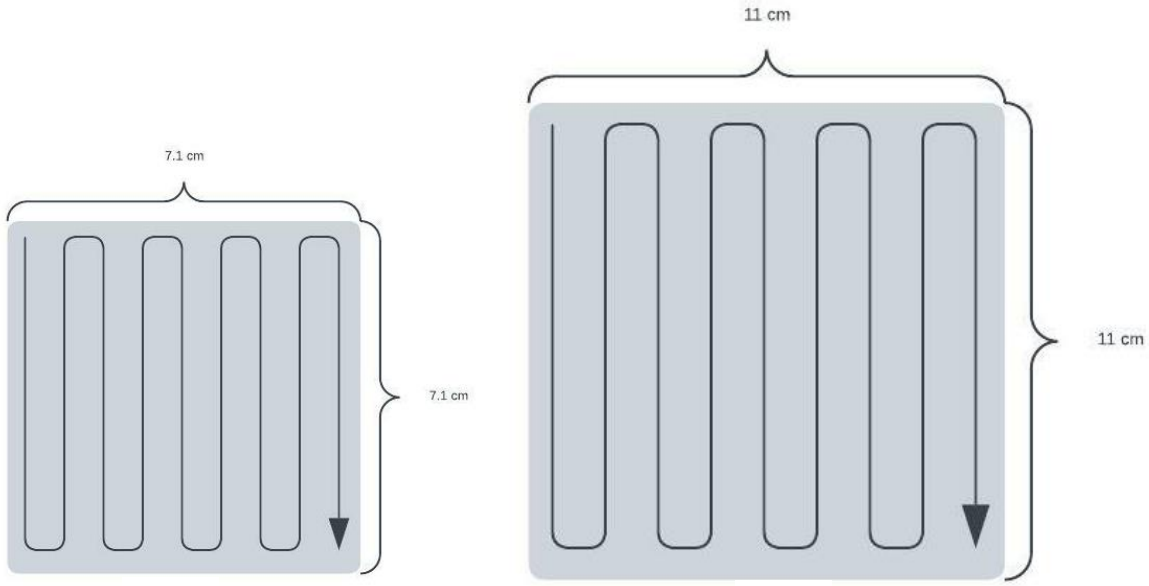


*Figure 3-5: Spray coating pattern and dimensions of the (a) CCM and (b) GDE.*

The spraying parameters used are shown in Table 3-3. The substrates were place on a heated vacuum plate, to secure and flatten the surface. Cathodes were loaded at 0.05 $mg_{Pt}/cm^2$, and anodes at 0.20 $g_{Pt}/cm^2$. Multiple layers were required in order to reach these loadings. The loadings were calculated from the difference in substrate mass before and after spraying (after allowing 20 minutes for solvents to completely evaporate.

*Table 3-3: Spraycoating parameters*

| Parameter | Value |
|---|---|
| **Ink flowrate** | 1.0 ml/min |
| **Sprayer speed** | 80 mm/s |
| **Heated table temperature** | 70 °C |
| **Nozzle height** | 60 cm |

### 3.3.3 The membrane electrode assembly

The Membrane Electrode Assembly (MEA) consisted of a CCM, sandwiched between two gas diffusion layers, followed by sealing material on either side. The sealing material consisted of a subgasket layer, followed by a layer of double-sided adhesive (DSA), and finally a silicone seal (cathode only). The subgasket material was hot-pressed to the CCM at 80 °C for 1 minute at a pressure of 10 MPa, whereas the DSA and silicone layers have adhesive layers which could be applied manually. The specifications and suppliers for these materials are given in Table 3-1.

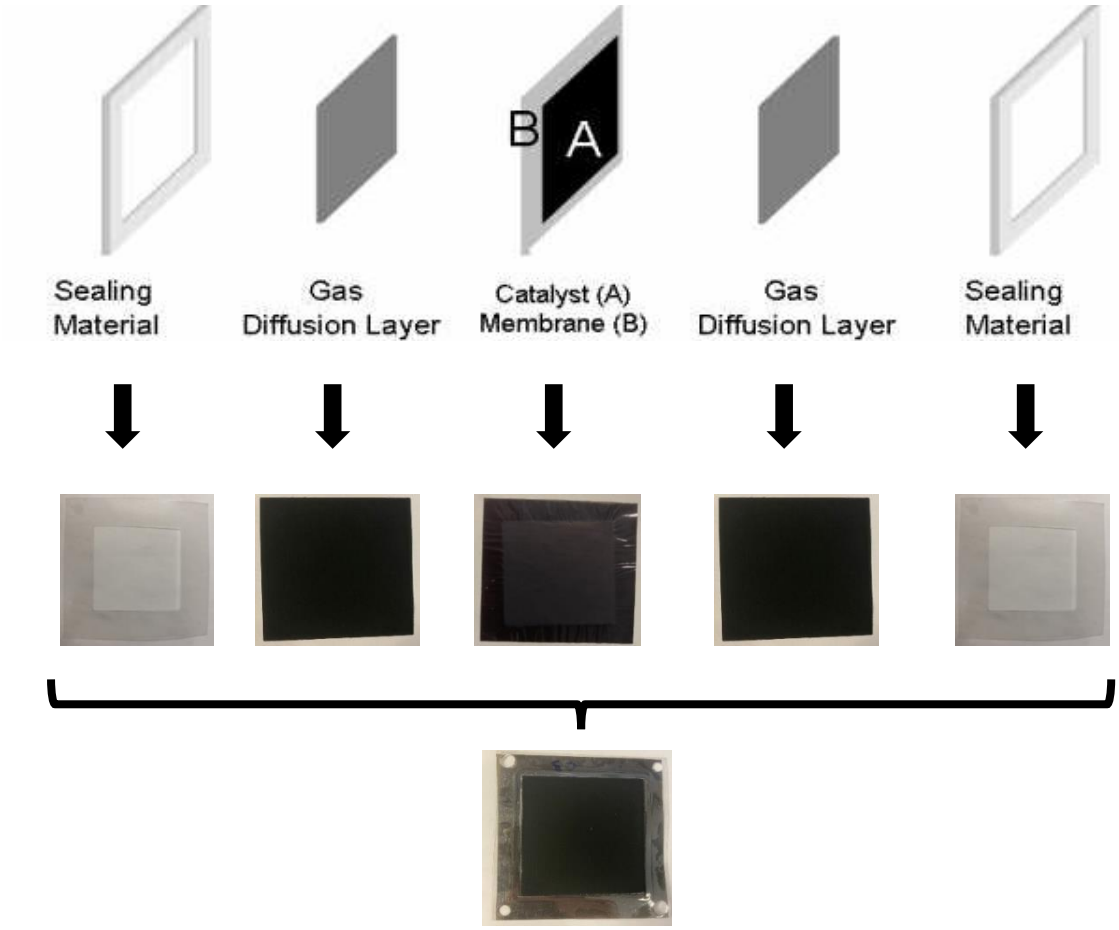


.

*Figure 3-6: Components of the MEAs used in this study. Adapted from Yuanbo Engineering (n.d.).*

### 3.3.4 Cell Assembly

The MEAs were assembled in a 50 $cm^2$ Baltic Fuel Cells fixture (Schwerin, Germany), which consisted of a fixture with two graphite flow field plates (with channel width and depth of 1 mm), and gold-plated stainless steel current collectors (Figure 3-7). The cell was equipped with an automated hydraulic cell compression piston, which secured the MEA at a pressure of 4.8 bara.

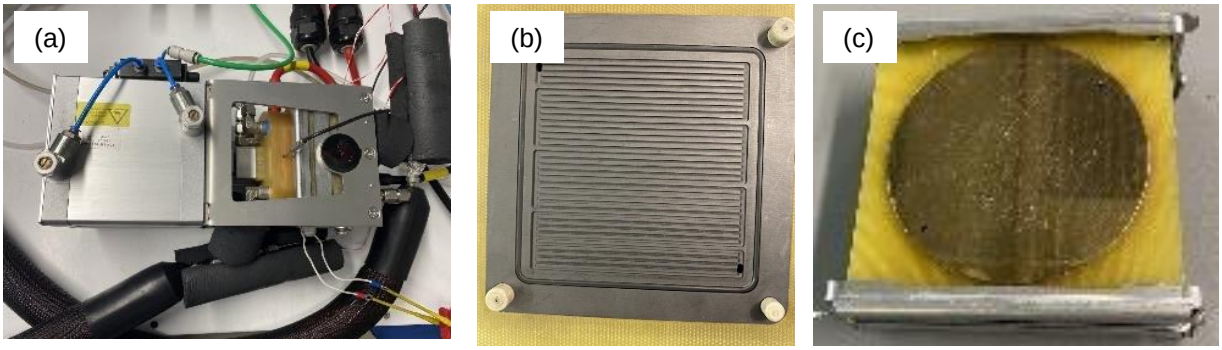


*Figure 3-7: Images of (a) Baltic Fuel Cells Fixture, (b) serpentine graphite flow field plates, and (c) gold-plated stainless steel current collectors.*

The cell was connected to a Fuelcon Evaluator C50-LT (Barleben, Germany), equipped with FuelWork software, capable of performing performance and ASTs).

### 3.3.5 Polarization curves

A polarisation curve is the standard diagnostic technique for assessing in-situ PEMFC performance. It is a voltage vs current density plot which provides information on the performance losses in a fuel cell under operating conditions. A typical polarisation curve with the three regions of performance loss is shown in Figure 3-8.

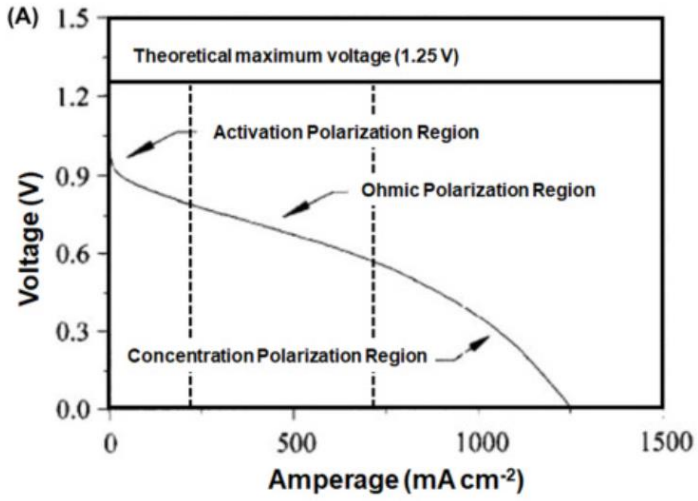


*Figure 3-8: Typical polarisation curve with performance loss regions. Adapted from Kaur (2022)*

Activation losses are due to sluggish ORR kinetics at the cathode; ohmic losses are due to resistance in the flow of ions and electrons; and mass transport losses (concentration polarisation region) are due to transportation limitations in the CL (Kaur, 2022).

Polarisation curves were measured on MEAs under two sets of conditions, namely stationary, and automotive conditions. These test conditions were considered representative of applicable in-the-field stationary and automotive applications. Automotive conditions were drier (lower feed humidities), with higher backpressures, and lower feed flowrates. These conditions were adapted from the EU harmonised test protocols for PEMFC MEA testing in single cell configuration (Tsotridis et al., 2015). Stationery and automotive test conditions are shown in Table 3-4.

*Table 3-4: Automotive and stationary test conditions for polarisation curves.*

| **Conditions** | **Stationary** | **Automotive** |
|---|---|---|
| **Cell Temperature (°C)** | 80 | 80 |
| **Anode Bubbler Temperature (°C)** | 80 (100 % RH) | 64 (50 % RH) |
| **Cathode Bubbler Temperature (°C)** | 75 (80 % RH) | 53 (30 % RH) |
| **Anode Back Pressure (bara)** | 2 | 2.3 |
| **Cathode Back Pressure (bara)** | 2 | 2.5 |
| **Anode min flow (Nl/min)** | 0.15 | 0.15 |
| **Cathode min flow (Nl/min** | 0.53 | 0.3 |
| **Anode Stoichiometry** | 1.5 | 1.3 |
| **Cathode Stoichiometry** | 2 | 1.5 |

The MEAs were conditioned for 2 hours by voltage cycling between 0.3 V and 0.8 V for 12 cycles. The voltage was held at 0.8 V for 30 seconds, followed by 10 minutes at 0.3 V during each cycle.

### 3.3.6 Cyclic Voltammetry

The ECSA of the cathode catalyst layer was determined from CV (in a similar way to CVs performed *ex-situ* on the 3-electrode cell). CV was performed on conditioned MEAs. The cathode air feed valve was closed, and the system was purged of oxygen using nitrogen gas at a flowrate of 30 Nl/h, for 20 minutes. CVs were performed at conditions shown in Table 3-5, cycling between 0.04 V and 0.9 V at a scan rate of 10 mV/s. The current limit was 10 A. Approximately 15 scans were recorded to produce an average ECSA.

.

*Table 3-5: Cyclic Voltammetry In-situ test conditions*

| Conditions | Value |
|---|---|
| **Cell Temperature (°C)** | 80 |
| **Anode Bubbler Temperature (°C)** | 80 (100 % RH) |
| **Cathode Bubbler Temperature (°C)** | 80 (100 % RH) |
| **Anode Back Pressure (bara)** | 1 |
| **Cathode Back Pressure (bara)** | 1 |
| **Anode Hydrogen flow (Nl/min)** | 0.5 |

The ECSA was determined by integrating the area under the curve for the hydrogen underpotential deposition ($H_{udp}$) region of the voltammogram, assuming a 210 $\mu C/cm^2_{Pt}$ monolayer hydrogen charge, and applying equation 3.2.

### 3.3.7 Accelerated stress tests

MEA durability studies are conducted using standardised AST protocols, as described by the U.S. Department of Energy (DOE Fuel Cell Technologies Office, 2016). As with ex-situ testing, both particle stability and support durability studies were performed in-situ, investigating the Pt dissolution and carbon corrosion, respectively. These durability studies were performed on conditioned MEAs, under conditions shown in Table 3-6. For the particle stability test, voltages were cycled between 0.6 V and 0.95 V for 10 000 cycles, with CV measurements occurring at cycles 1, 10, 100, 200, 500, 1000, 2000, 5000 and 10000. For the carbon corrosion test, the potential was cycled between values of 1.0 V and 1.5 V for a total of 5000 cycles with CV measurements occurring at cycles 1, 10, 100, 200, 500, 1000, 2000 and 5000.

*Table 3-6: In-situ particle stability and carbon corrosion test conditions*

| Conditions | Particle Stability |
|---|---|
| **Cell temperature (°C)** | 80 |
| **Anode bubbler temperature (°C)** | 80 (100 % RH) |
| **Cathode bubbler temperature (°C)** | 80 (100 % RH) |
| **Anode back pressure (bara)** | 1 |
| **Cathode back pressure (bara)** | 1 |
| **Anode min flow (Nl/min)** | 0.2 |

### 3.3.8 Electronic Impedance Spectroscopy

The purpose of Electronic Impedance Spectroscopy (EIS) was to identify and quantify resistance contributions in the MEA. Electrochemical reactions are mainly affected by electrolyte resistance, mass transfer from the bulk solution to the reactive site, adsorption of electroactive species and charge transfer to the electrode surface. These processes were modelled as electrical components in a simple electric circuit. The Randles cell is the most commonly used model for the electrochemical interface, as shown in Figure 3-9, where $R_{ct}$ is the charge transfer of the electrode process, $C_{dl}$ is the capacitance of the double layer and $R_{el}$ is the resistance of the electrolyte (Yuan et al., 2010). Randles circuit was applied using Zview software (Scribner).

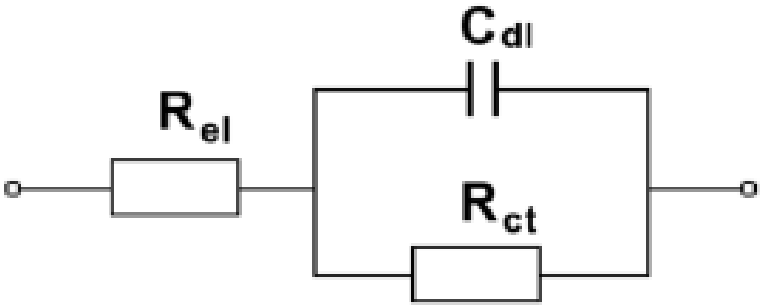


*Figure 3-9: Randles cell equivalent circuit model, adapted from* Yuan et al. (2010)

The individual components of this circuit were extracted in an electrochemical system by applying an AC amplitude perturbation to a DC signal with a changing frequency (Yuan et al., 2010). The change in impedance is measured across a range of frequencies. A Nyquist plot is generated from the real and imaginary resistances. A typical Nyquist plot for a Randles circuit is shown in Figure 3-10,

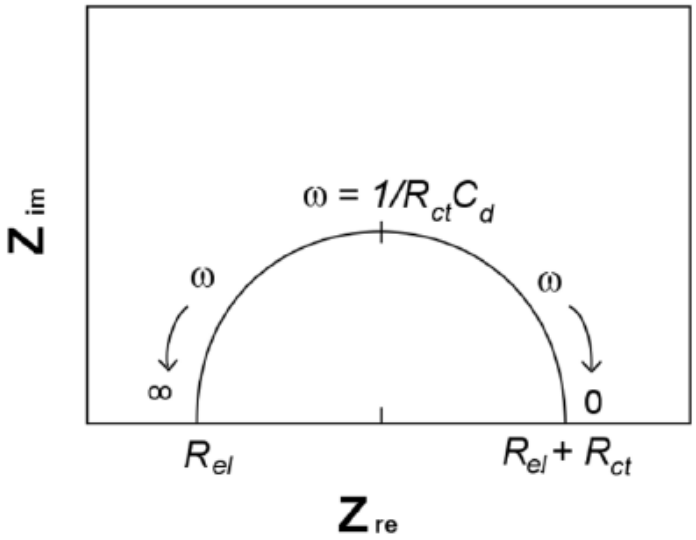


*Figure 3-10: Nyquist plot for a typical Randles circuit, adapted from Yuan et al. (2010)*

From Figure 3-10 it is shown that as $\omega \rightarrow \infty$, the double layer capacitance is close to zero, and the total impedance is represented by the electrolyte resistance ($R_{el}$) (which is the left intersection of the semicircle with the real axis). As $\omega \rightarrow 0$, the right intersection of the semicircle represents the combined electrolyte and charge transfer resistances. The double layer capacitance value can be calculated from the peak value of the frequency (Yuan et al., 2010).

In this work, EIS was performed across a frequency sweep of 20 kHz to 0.1 Hz, at an applied current density of 0.1 A/cm$^2$ and cell temperature of 80°C, with hydrogen and air being supplied to the cathode and anode respectively. Electrolyte resistance, charge transfer resistance and double layer capacitance were determined by applying the Randles circuit model.

## 3.4 MEA Physical Characterization

### 3.4.1 Mercury Intrusion Porosimetry

Mercury Intrusion Porosimetry (MIP) was used to evaluate the pore size distribution, porosity, and pore volume of the CCMs. MIP samples were prepared by cutting 2 $cm^2$ sections from coated CCMs and sent for analysis by Anton Paar QuantaTec Inc., Florida, USA.

### 3.4.2 Gas Permeability

In order to compare the permeability of the different catalyst layer structures the CFP-1200AEL permeameter (PMI) was used to determine the through-plane gas permeability of GDEs coated with the cathode catalyst layer with a Pt loading of 0.20 $g/cm^2$.

The procedure was as follows. The device was turned on and purged with synthetic air for 45 minutes. The GDEs were cut into a circular shape with diameter of roughly 2.0 cm and weighed. The sample thickness was determined by averaging 5 thickness measurements using a precision thickness gauge . The sample was secured in the permeameter, as shown in Figure 3-11 and tightened to a torque of 20 Nm using a torque wrench. Using the CapWin software (V. 6.74.96), the thickness, mass, and density were specified, and the test was run. This procedure was performed on 3 samples for each catalyst, with each sample being tested 3 times.

*Figure 3-11: Gas permeameter assembly*

The outcome of the gas permeability test is given as the Gurley number. The Gurley number was defined as the amount of time required for 100 $cm^3$ of air to pass through 1 $in^2$ (6.45 $cm^2$) of material at a pressure differential of 0.176 psi. The units of the Gurley number are given in seconds/100 $cm^3$. A greater Gurley number implied greater resistance to air permeability.

### 3.4.3 Cross-sectional Scanning Electron Microscopy

Cross-sectional SEM analysis was done on Beginning of life (BOL), and end-of-life (EOL) CCMs (subjected to particle stability and carbon corrosion tests). BOL samples were gasketed, compressed and conditioned to be comparable to the EOL samples. The samples were prepared by cutting 1 cm x 2 cm sections from the centre of the MEAs and embedding them in an epoxy resin. This resin was prepared by mixing EpoFix resin with EpoFix Hardener. The resin puck was then polished, to reveal the cross-sectional view of the samples. SEM imaging was performed using the FEI Field Emission Nova NanoSEM 230 device, fitted with an Oxford X-Max detector and INCA software, at 30 kV, at the Electron Microscopy unit at the University of Cape Town. From here, the catalyst layer thickness was determined.

# 4 Results and Discussion

## 4.1 Physical and electrochemical properties of catalyst materials

The purpose of this section is to present, discuss and compare the physical and electrochemical properties of two commercial PtCo/C catalysts (PtCoU30 and PtCoT50) and a Pt/C benchmark catalyst (PtH40). The physical characterisation techniques used include TGA, TEM and SEM imaging as well as EDX elemental analysis. The electrochemical investigations consist of cyclic voltammetry, linear sweep voltammetry and accelerated stress tests in a standard 3 electrode setup.

### 4.1.1 Physical characterisation

#### *4.1.1.1 Catalyst specifications*

The two commercial catalysts investigated were the Umicore Elyst Pt30 0690 (PtCoU30) and TKK TEC36F52 (PtCoT50) catalysts, with detailed specifications shown in Table 4-1. Both catalysts are supported on High Surface Area Carbon (HSAC) but differ in metal loadings (30 wt% for PtCoU30 and 52 wt% for PtCoT50). The Platinum catalyst used for comparison was an in-house benchmark, heat treated 40 wt% Pt catalyst (PtH40).

*Table 4-1: Catalyst material specifications and nomenclature.*

| Nomenclature in this work | Catalyst ID | Specifications | Supplier |
|---|---|---|---|
| PtCoU30 | Elyst Pt30 0690 | 30 wt% PtCo/C | Umicore |
| PtCoT50 | TEC36F52 | 52 Wt% PtCo/C | TKK |
| PtH40 | PtH40 | 40 wt% Pt/C | Mintek |

#### *4.1.1.2 TEM*

Transmission electron microscopy was performed on the PtCoU30, PtCoT50 and PtH40 catalysts, to present and compare morphological differences and to determine the particle size distributions.

*PtCoU30*

The PtCoU30 catalyst (Figure 4-1) showed relatively uniform and well dispersed spherical PtCo particles on the carbon support. The particle sizes were fairly homogenous, with few outlying larger particles (Figure 4-1 (a)). Little to no particle agglomeration was observed in these images. The particle size distribution was determined from sample of 560 particles. PTCOU30 presented a relatively narrow range of particle sizes, with the average particle size of 5.4 nm and a standard deviation of 1.3 nm. A few outlying large particles were observed (maximum of 15 nm), with the smallest particle being 3.0 nm.

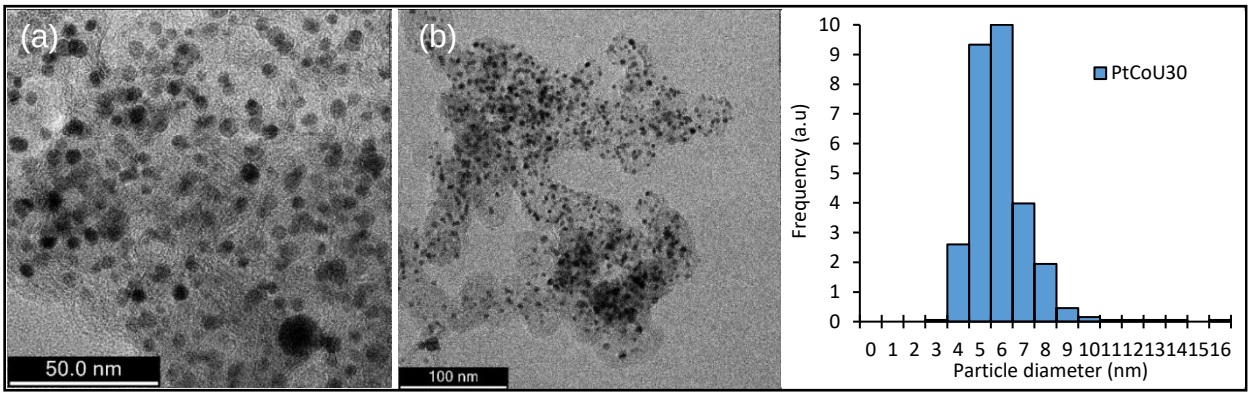


*Figure 4-1: TEM images of PtCoU30 catalyst at varying magnifications (a and b), with a bar chart showing the particle size distribution.*

*PtCoT50*

Figure 4-2 shows TEM images of the PtCoT50 catalyst at different magnifications. In contrast to the PtCoU30 catalyst, the PtCoT50 catalyst was visibly inhomogeneous in particle size, with varying PtCo particle sizes on the support surface. This was increasingly evident at high magnification. The particle size distribution was produced from a sample of 630 particles. The average PtCoT50 particle size (7.1 nm) was larger than the PtCoU30 catalyst. This catalyst showed a wide spread of particle sizes (standard deviation of 2.6 nm), with particle sizes distributed fairly evenly from 4 to 8 nm.

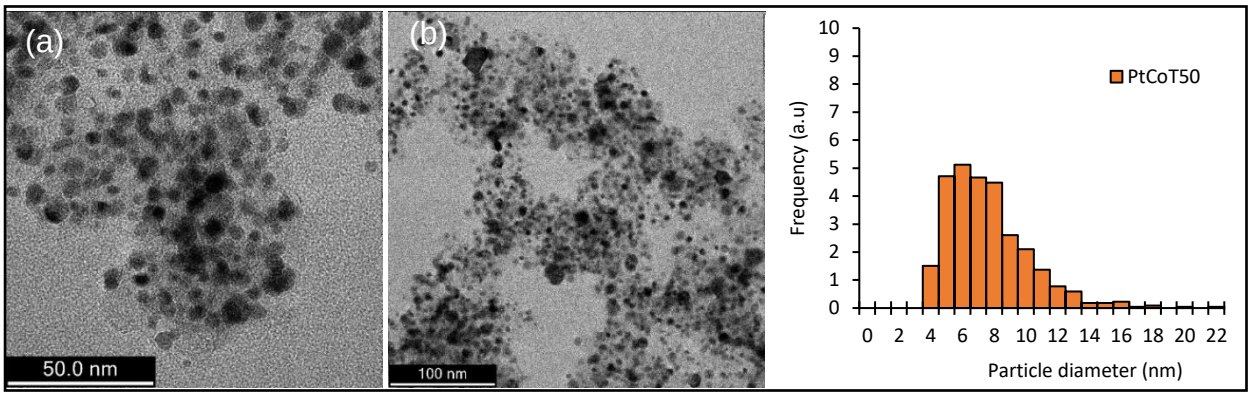


*Figure 4-2: TEM images of PtCoT50 catalyst at varying magnifications (a and b), with a bar chart showing the particle size distribution.*

*PtH40*

Figure 4-3 shows TEM images and particle size distribution for the PtH40 Pt/C catalyst. The particle sizes were also reasonably inhomogeneous. In general, the Pt/C particles do not appear as perfectly spherical as either of the PtCo/C catalyst. From a sample of 650 measured particles, the average particle size of PtH40 was 5.0 nm. PtH40 showed the largest spread in measured particle sizes (1.9 nm to 22.0 nm), with a standard deviation of 2.0 nm.

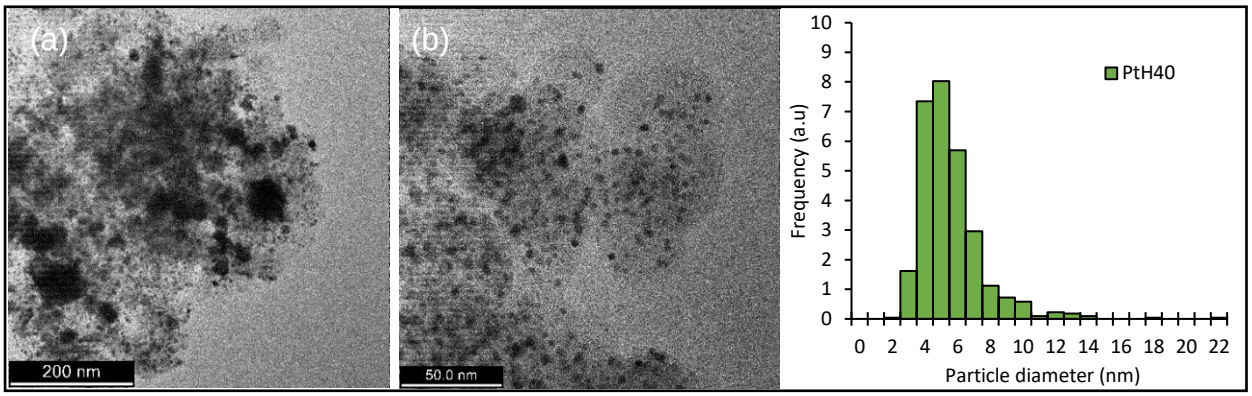


*Figure 4-3: TEM images of PtH40 catalyst at varying magnifications (a and b), with a bar chart showing the particle size distribution.*

PtH40 showed the smallest average particle size of the three catalysts (5.0 nm) followed by PtCoU30 (5.4 nm) and PtCoT50 (7.1 nm). PtCoU30 had the narrowest distribution of particle sizes, followed by PtH40 and PtCoT50.

#### *4.1.1.3 XRD*

Figure 4-4 contains the diffractograms for the catalysts under investigation. The sharp diffraction peaks indicate a crystalline presence with no sign of an amorphous carbon hump at lower angles. Four distinct peaks are observed for each catalyst. For the Pt catalyst, these peaks occurred at 2θ values of 47.7°, 55.7° 82.7° and 101.5°, and are representative of Pt(111), Pt(200), Pt(220), Pt(311) crystallographic planes respectively. No crystallite structure of Co is observed; however, all four characteristic Pt peaks are present for the two PtCo catalysts, with a positive shift in the 2θ value. This shift is indicative of the formation of a PtCo alloy, by the intercalation of the Co particle in the face-centred-cubic Pt lattice (Kaewsai et al., 2017). The PtCo diffractograms matched closely with a $Pt_3Co$ reference pattern, indicating that the Pt:Co ratio in these catalysts is indeed 3:1, as specified by the suppliers.

The average crystallite size for each catalyst was determined using the Sherrer equation. These crystallite sizes for PtH40, PtCoT50, and PtCoU30 were 11.2 nm, 5.1 nm, and 4.4 nm respectively. These values represent the mean value of the cube roots of the individual crystallite volumes, assuming spherical particles. However, XRD cannot be used to accurately determine average crystallite sizes for samples with broad size distributions. Furthermore, XRD determines the *crystallite* size; one particle may consist of multiple crystallite domains. Therefore, the physical particle sizes of each catalyst were taken from TEM images.

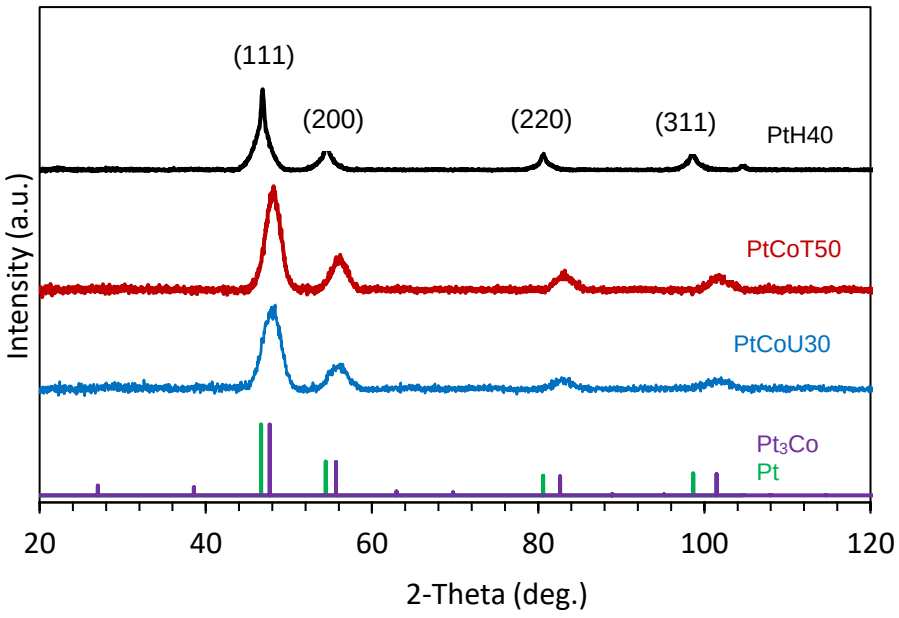


*Figure 4-4: Diffractograms of PtH40, PtCoT50 and PtCoU30 catalyst powders.*

#### *4.1.1.4 EDS*

EDS was used to determine the Pt/Co ratio, and total metal loading of the catalysts. Table 4-2 shows the average Pt and Co contribution for each of the catalysts. The atomic Pt:Co ratio for the catalysts was similar at approximately 4:1. This is not the same as the nominal Pt/Co ratio provided by the suppliers, or what has been shown on XRD (both 3:1). However, the difference between the catalysts compositions was considered to be negligible and considered the same in this study.

*Table 4-2: Catalyst EDS results*

| | | Co | Pt | Std Deviation |
|---|---|---|---|---|
| **PtCoT50** | Weight % | 7.30 | 92.7 | 1.29 |
| | Atomic % | 20.6 | 79.3 | 3.13 |
| **PtCoU30** | Weight % | 7.52 | 92.4 | 1.08 |
| | Atomic % | 21.1 | 78.8 | 2.57 |

#### *4.1.1.5 TGA*

Thermogravic analysis was used to determine the metal contents of the catalysts and are provided in with the PtH40 benchmark platinum catalyst at 45 wt%, (5% higher than suggested by the supplier).

Table 4-3. The determined metal contents for these catalysts are consistent with the nominal metal contents reported by the catalyst manufacturers. The PtCoT50 catalyst has a much higher total metal content (54 wt%) than the PtCoU30 catalyst (29.5 wt%), with the PtH40 benchmark platinum catalyst at 45 wt%, (5% higher than suggested by the supplier).

*Table 4-3: Metal contents of PtCoT50 and PtCoU30 catalysts determined by TGA, compared to nominal values*

| Catalyst | TGA (wt %) | Nominal (wt %) |
|---|---|---|
| **PtCoT50** | 54.4 | 52 |
| **PtCoU30** | 29.5 | 30 |
| **PtH40** | 45.6 | 40 |

#### *4.1.1.6 BET*

The catalyst surface area of the supported catalysts was determined with BET. The PtCoU30 catalyst has a 47% greater overall surface area (461 $m^2/g$) compared to the PtCoT50 catalyst (313 $m^2/g$) with PtH40 showing an intermediate surface area of 403.8 $m^2/g$. All three catalysts are reported to be supported on high surface area carbon; however, they differ slightly. PtCoT50 support is partially graphitised, which may explain the lower surface area. PtCoU30 support is reported simply as carbon black, by the supplier, and PtH40 is supported on Ketjenblack, which is a highly electrically conductive carbon black. The trend in surface area is likely due to the relative carbon/metal (C/M) ratio. The highest C/M ratio of PtCoU30 resulted in the highest surface area, whereas PtCoT50 has the lowest surface area and the lowest C/M ratio.

### 4.1.2 Catalyst electrochemical characterisation

#### *4.1.2.1 Thin film ink optimisations*

The reproducibility of thin film RDE electrochemistry is directly dependant on the quality of the catalyst layer on the electrode. The composition, drying and deposition of the catalyst ink on the working electrode was optimised to ensure precise and accurate measurements. The methodology developed for RDE using PtCoU30, PtH40 and PtCoT50 catalysts is based on the method described by Garsany et al. (2010).

Garsany et al. (2010) suggest a range of 7 to 30 $\mu g_{Pt}/cm^2$ loading for catalysts having concentrations of 10 to 50 wt% Pt. Lower loadings are optimal for catalysts with lower Pt content. Alloy catalysts, which are inherently hydrophobic, may require higher alcohol/water ratios, to ensure sufficient dispersion in solution. The baseline procedure shown in Table 4-4 was applied to each of the three catalysts and adapted to the final procedures shown.

The baseline procedure applied to the PtCoU30 catalyst yielded an ink that was too viscous, drying in coffee-stain ring patterns, with clumps of undispersed catalyst visible on the electrode. By decreasing the loading by 40%, increasing the drying temperature, and covering the drying electrode (to control rate of drying), the resulting film quality was significantly improved. Figure 4-5 shows the film quality for the

PtCoU30 catalyst using a) the baseline procedure, and b) the PtCoU30 adapted procedure.

*Table 4-4: RDE catalyst ink baseline and adapted procedures.*

| Parameter | Baseline procedure | PtCoU30 adapted procedure | PtCoT50 adapted procedure | PtH40 adapted procedure |
|---|---|---|---|---|
| **Isopropanol : Water ratio** | 1:4 | 1:4 | 1:1 | 1:4 |
| **Electrode loading ($\mu g_{Pt}/cm^2$)** | 10.7 | 6.2 | 10.7 | 8.7 |
| **Drying temperature (°C)** | 60 | 75 | 75 | 75 |
| **Drying condition** | Uncovered | Covered | Covered | Covered |
| **Total catalyst mass (mg)** | variable | 4.2 | 4.2 | 4.2 |

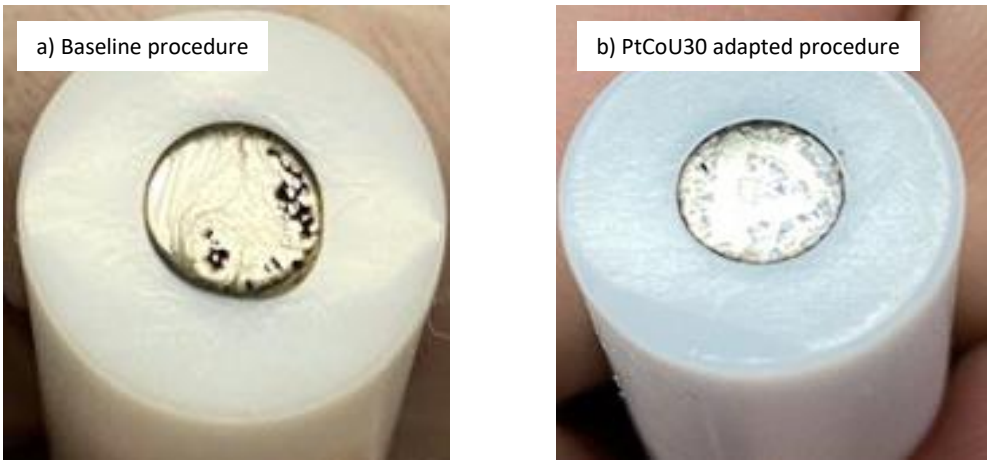


*Figure 4-5: Catalyst coated working electrodes using PtCoU30 catalyst for a) the baseline procedure and b) the PtCoU30 adapted procedure*

The baseline procedure loading for the PtCoT50 catalyst was less viscous than the PtCoU30 baseline ink, likely because PtCoT50 has a higher metal content, and therefore requires less catalyst mass for the same loading. However, the PtCoT50 baseline ink did not remain fully dispersed in the catalyst ink. Increasing the alcohol/water ratio (from 1:4 to 1:1) resulted in good thin-film quality.

The PtH40 catalyst ink was adjusted to have the same catalyst mass in solution as the PtCoT50 and PtCoU30 inks. The resulting ‘adapted procedures’ catalyst inks were all made with 4.2 mg of catalyst. This means that the total solid content of the inks was

kept consistent, but with varied Pt loadings. Electrochemical performance was only performed on electrodes with perfect coatings.

#### *4.1.2.2 Electrochemical surface area*

The ECSAs for the PtCoU30, PtCoT50 and PtH40 catalysts were determined from CV in the 3-electrode cell, as described in section 3.2.4.

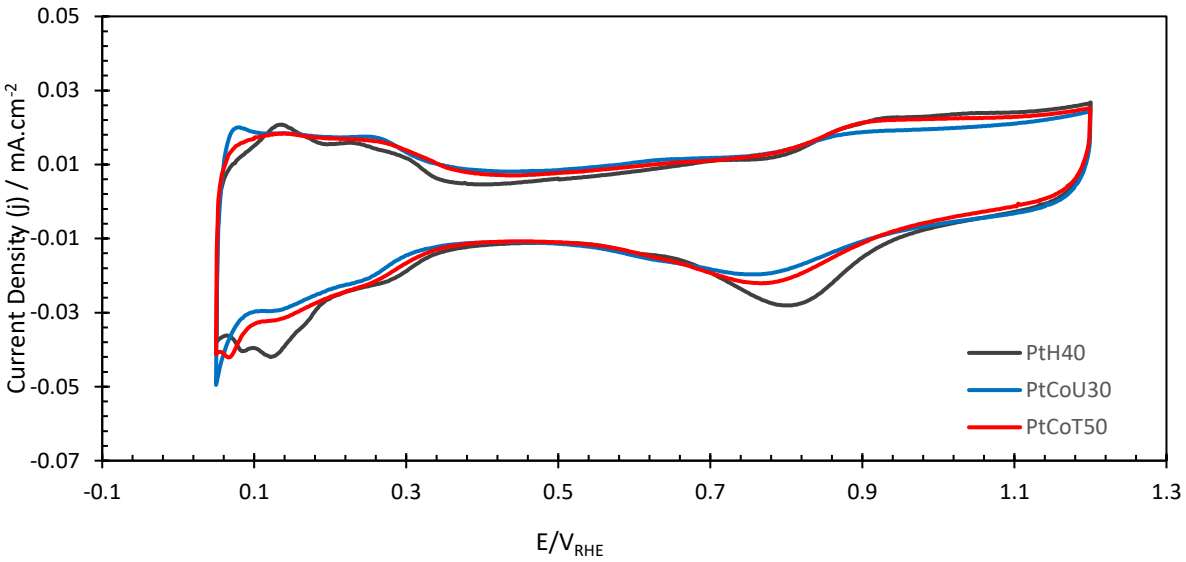


*Figure 4-6: Cyclic Voltammograms for PtH40, PtCoU30 and, in 0.1 M $HClO_4$, at a scan rate of 20 mV/s.*

The Pt/C catalyst had a higher ECSA (70.2 $m^2/g_{Pt}$), than either of the PtCo Catalysts (61.9 $m^2/g_{Pt}$ for PtCoU30 followed by 49.2 $m^2/g_{Pt}$ for PtCoT50). These values are in agreement with what has been shown in literature for commercial PtCo catalysts, under similar test conditions (54 $m^2/g_{Pt}$ for a 50 wt % PtCo/HSC, and 70 $m^2/g_{Pt}$ for a 30 wt % PtCo/HSC catalyst) (Shinozaki et al., 2016).

The decrease in ECSA from PtH40 to PtCoU30 to PtCoT50 corresponds to the increase in average particle size, 5.0 nm, 5.4 nm and 7.1 nm, respectively. Catalysts with greater Pt to carbon ratios generally have smaller ECSAs. This was shown by Li et al., (2019), where an increase in Pt wt % (from 5% to 50 wt%) at similar electrode loadings resulted in a decrease in ECSA, due to the relative increase in catalyst layer thickness, and decrease in accessible Pt particles. From Figure 4-6, a clear difference in the Hydrogen region (0.05 <E< 0.35V vs. RHE) can be observed between the Pt and PtCo catalyst. The PtCo catalysts exhibit notably less-defined peaks in this region,

which is classically ascribed to an increase in capacitive and ohmic effects in PtCo catalysts, as compared to Pt catalysts (Nikkuni et al., 2015).

#### *4.1.2.3 Linear Sweep Voltammetry – ORR performance*

Figure 4-7 summarises the performance curved for PtCoU30, PtCoT50 and PtH40 catalysts. Figure 4-7 a) shows the ORR polarisation curves at 1600 rpm. The catalysts achieved limiting current densities greater than 1.0 A/cm$^2$. However, the PtCo catalysts exhibited an increase (more positive) in current density over the limiting current region, whereas the Pt catalyst remained relatively stable. This is likely due to a greater rate of $H_2O_2$ formation, via the two-electron pathway in the PtCo catalysts compared to the Pt. The two electron pathway is less efficient than the 4 electron pathway, therefore results in smaller limiting currents. Sethuraman et al. (2009) showed that binary (including PtCo) and ternary Pt alloy catalysts show greater selectivity towards $H_2O_2$, especially at lower voltages, compared to Pt catalysts.

Figure 4-7 b), c) and d) are the Tafel plots obtained in the range of 0.86 V to 0.94 V vs RHE. Figure 4-7 b) shows the absolute voltage vs kinetic current, whereas figures c) and d) are corrected for by platinum weight and ECSA respectively. The mass specific and area specific activities were determined from the Tafel plots at 0.9 V vs RHE and are shown in Figure 4-7 e) and f). From Figure 4-7 b), the ORR activity for the catalysts increased in the order of: PtH40 < PtCoU30 < PtCoT50 .However, this trend changes in Figure 4-7 c) and e) which shows that the mass activities ($I_m$) of the catalysts increased in the following order: PtH40 < PtCoT50 < PtCoU30. Similarly, the specific activities ($I_s$) increased: PtH40 < PtCoT50 ≤ PtCoU30 (see Figure 4-7 d) and f)). Essentially, the absolute performance of the PtCoT50 electrode was the highest, however, when correcting for both platinum mass and ECSA, the PtCoU30 electrode has the greatest activity. The PtCo alloy catalysts performed consistently better than the Pt catalyst. These results are consistent with the work by Shinozaki et al. (2016) who showed that a 27.4 Pt wt% PtCo/HSC catalyst had a higher ECSA (70 m$^2$/g$_{Pt}$), $I_m$ (1.53 mA/mg$_{Pt}$) and $I_s$ (2.17 mA/cm$^2$) compared to a 46.4 Pt wt% PtCo/HSC (with ECSA of 54 m$^2$/g$_{Pt}$ $I_m$ of 0.78 mA/mg$_{Pt}$ and $I_s$ of 1.5 mA/cm$^2$). The electrode loadings and ionomer content used by Shinozaki et al. (2016) differ from the current work, and can therefore not be compared directly.

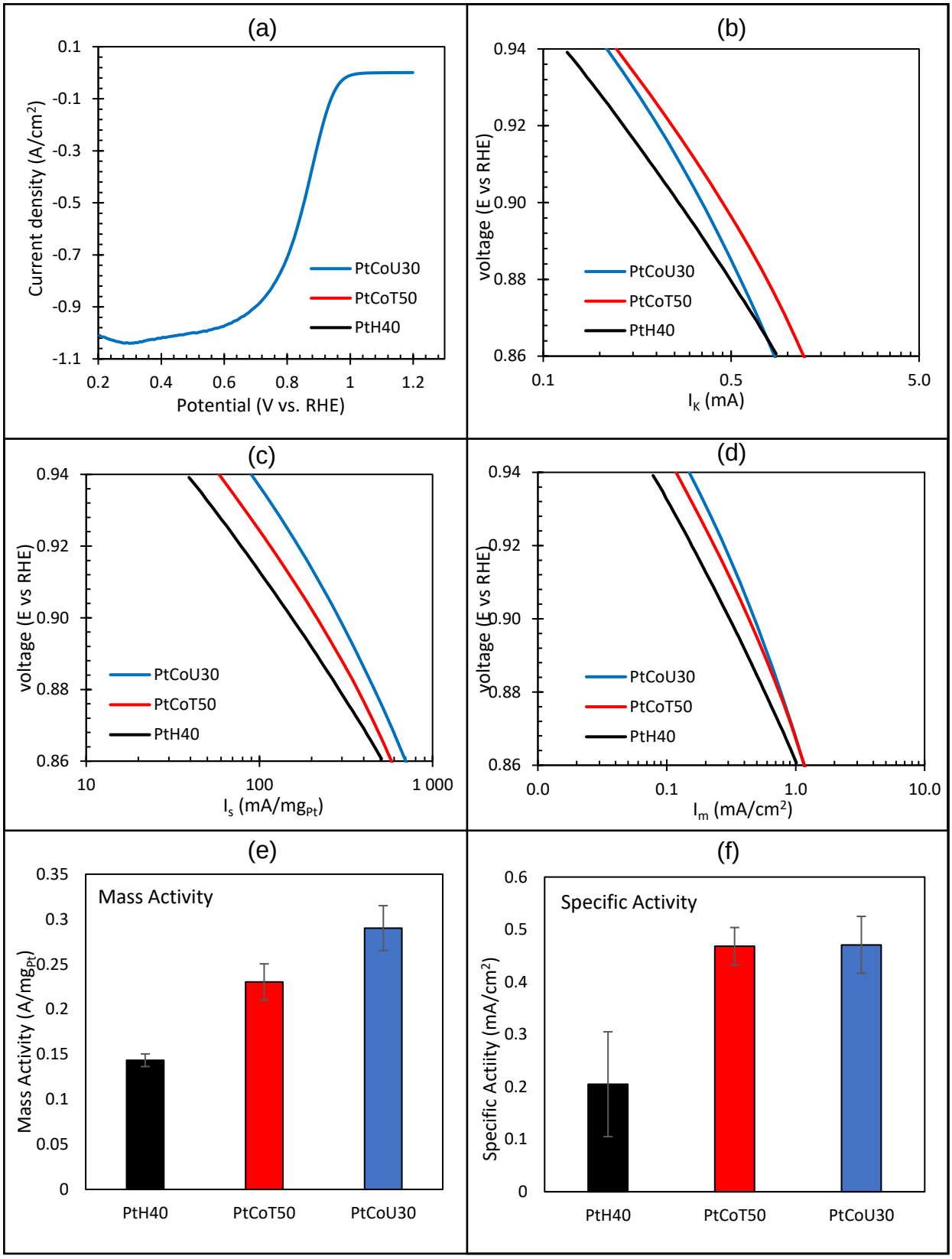


*Figure 4-7: Comparison of PtCoU30, PtCoT50 and PtH40 catalysts shown by a) ORR cathodic sweep (1600 rpm, 10 mV/s) in 0.1 M $HClO_4$ b)Tafel plot of kinetic current ($I_k$ vs E) c) Tafel plot for the mass activity and d) Tafel plot for the specific activity, e) Mass activities, f) specific activities determined from Tafel plots and 0.9 V (1600 rpm, 10 mV/s in 0.1 M $HClO_4$ ).*

Literature describes that platinum utilisation (and by extension, mass activity) decreases with an increase in electrode loading (Garsany et al., 2010). This is mainly due to an increase in isolated subsurface Pt particles, as the catalyst layer thickness increases. The electrode loadings of these three catalysts have been kept close to the lower end of the suggested optimal range (7 to 30 $\mu g/cm^2$), to improve ORR activity, however, owing to the inherent differences of the catalyst materials, the optimised ink formulations resulted in slightly different final loadings for each catalyst. The PtCoU30 (6.2 $\mu g/cm^2$) catalyst had the lowest loading, followed by PtH40 (8.7 $\mu g/cm^2$) and PtCoT50 (10.7 $\mu g/cm^2$). These differences in Pt loading are not large enough to expect significant effect on the comparability of these results, but it is possible that the mass activity of PtCoU30 benefited from having the lowest loading of the three catalysts.

The PtCo catalysts also exhibited greater specific activities ($I_s$) than the Pt catalyst. This is to be expected, considering that PtH40 catalyst had the highest ECSA (70.2 $m^2/g_{Pt}$), due to its smaller average particle size (5.0 nm), and the lowest ORR activity. The underlying difference in electronic structure of PtCo alloys compared to Pt catalysts, allows for higher activity at similar ECSAs. According to Ramaswamy et al. (2021) the increased activity of these PtCo catalysts can be attributed to the moderation of binding strength of reaction intermediates and increased efficiency in breaking of the $O_2$ double-bond. This binding moderation effect is caused by the geometric strain induced by sub-surface cobalt, as well as the electronic ligand effect which modifies Pt binding properties.

The PtCo catalysts have virtually identical specific activities, indicating that, by surface area, their ORR performance is the same despite having different particle size distributions, electrode loadings and metal/carbon ratios. This is consistent with the work by Higuchi, Uchida and Watanabe (2005) who showed that area-specific ORR activity is independent of Pt loading level. This explains why the PtCo area specific activities are similar, while having improved intrinsic activity, compared to the Pt catalyst. From these results it is expected that the PtCo MEAs will outperform the Pt benchmark; furthermore, the PtCo30 MEA is likely to show better performance than the PtCoT50 MEA.

#### *4.1.2.4 RDE accelerated stress tests*

Figure 4-8 and Figure 4-9 show the change in ECSA for the catalysts during 6000 cycles of catalyst and support durability tests, respectively. The y-axis in each graph is normalised to the maximum ECSA observed throughout the test.

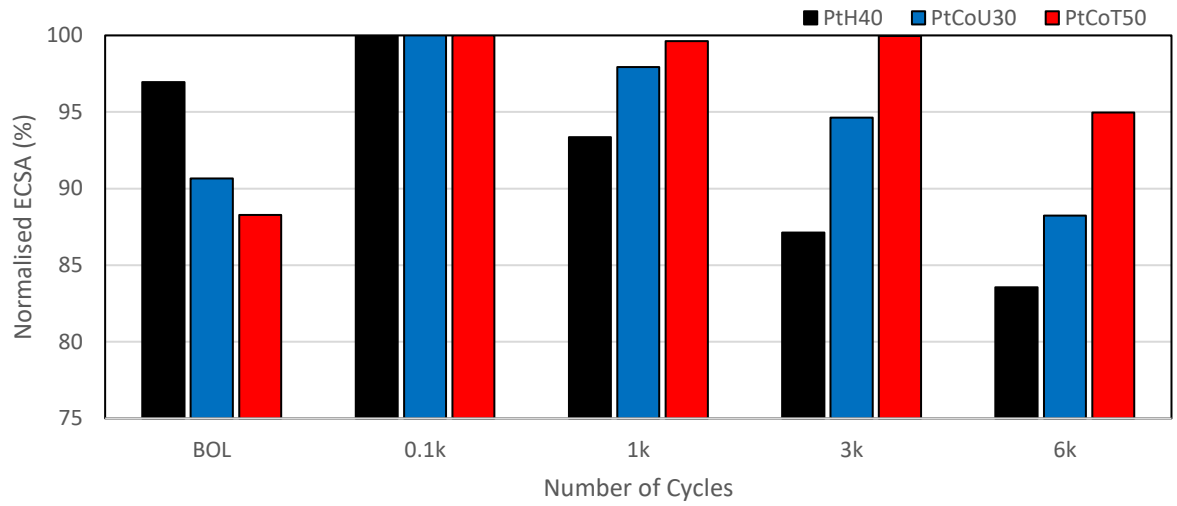


*Figure 4-8: ECSA as a function of cycle number in catalyst (Pt) durability study for PtH40, PtCoT50 and PtCoU30 catalysts for 6000 cycles between 0.6 V and 0.9 V at 100 mV/s.*

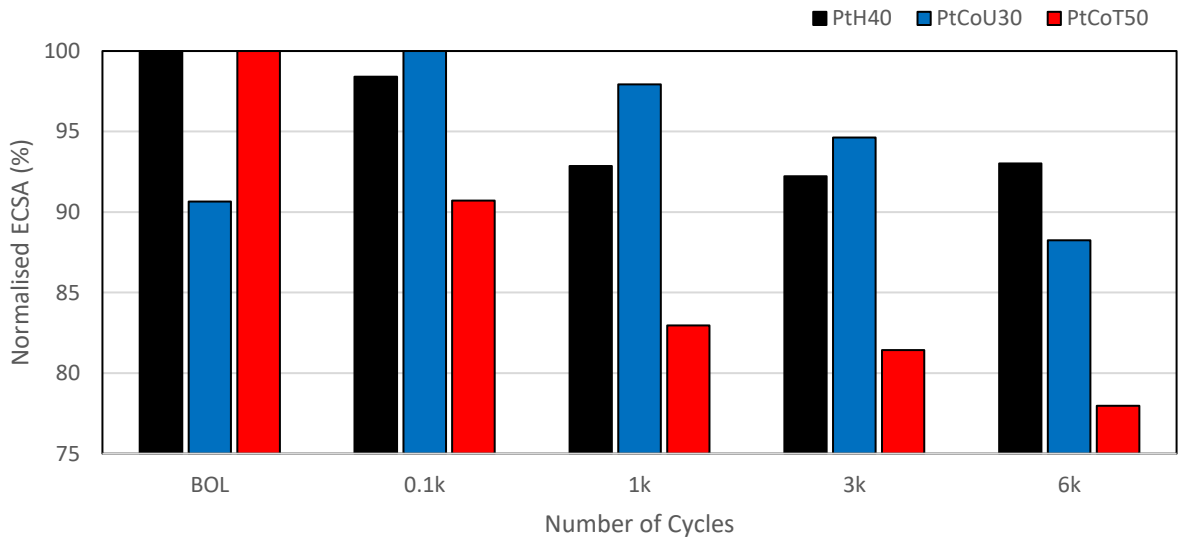


*Figure 4-9: ECSA as a function of cycle number in support durability study for PtCoT50, PtCoU30 and PtH40 Catalysts for 6000 cycles between 1.0 V and 1.5 V at 100 mV/s.*

The ECSAs were expected to decrease after being subjected to support and catalyst durability tests. The initial increase in ECSA, after 100 cycles has also been found in literature (Papadias et al., 2018), and was due to an increase in available active sites. For the support durability AST, this initial increase is likely due to exposure of previously electronically isolated catalyst particles following initial carbon oxidation.

For the catalyst durability AST, especially for PtCo catalysts, the initial increase in ECSA is due to the dealloying of Co, and subsequent ‘Pt skin’ formation on catalyst particles during cycles of Pt dissolution and redeposition. This results in an initial increase in Pt availability on the surface of particles (Bing et al., 2010). After the first 100 cycles the ECSA (Figure 4-8) declined gradually to 6000 cycles. The decline in ECSA was due to the dissolution of bare-Pt and Pt-oxides on the catalyst surface during the anodic sweep. Redeposition of Pt occurs during the cathodic sweep, however, less coordinated Pt atoms redeposit, resulting in exposed edge sites in the PtCo particles, which are more susceptible to attack in the following anodic sweep (Takahashi and Kocha, 2010). The continuous loss of Pt in this way results in the decrease in ECSA. The ECSA loss was the largest for the PtH40 catalyst, followed by PtCoU30, and PtCoT50. This trend in durability is likely due to the increase in average particle size from PtH40 to PtCoU30 to PtCoT50. PtCoU30 showed a smaller average size (5.4 nm) compared to PtCoT50 (7.1 nm), and a higher initial ECSA (61.9 $m^2/g_{Pt}$ for PtCoU30 and 49.2 $m^2/g_{Pt}$ for PtCoT50). The higher surface area and exposed Pt surface in the PtCoU30 catalyst made it more susceptible to Pt oxidation compared to the PtCoT50 catalyst.

In the support durability study, Figure 4-9, only the PtCoU30 catalyst showed an increase in ECSA after the first 100 cycles before declining, whereas the PtH40 and PtCoT50 catalysts showed a gradual decline in ECSA for the 6000 cycles. PtCoU30 has the greatest carbon to metal ratio; it is possible that initially, as carbon is oxidised, previously isolated Pt particles become liberated, and may contribute to the ECSA. The PtCo catalysts exhibited poorer support durability compared to the Pt catalyst. After 6000 cycles, the total losses in ECSA for PtH40, PtCoU30 and PtCoT50 were 6.9 %, 11.9% and 22.0% respectively. The large loss in ECSA seen in the PtCoT50 catalyst is likely due to the higher Pt/C ratio compared to the other catalysts. It has been shown that PGM clusters accelerate carbon oxidation, which, in turn, results in compromised particle structural support, leading to further PtCo detachment an agglomeration (Du et al., 2021). PtCoT50 is therefore more susceptible to carbon corrosion, particle detachment and agglomeration, resulting in ECSA loss.

### 4.1.3 Section Summary

Chapter 4.1 provides insight into the physical and electrochemical properties of each catalyst, which will aid in interpreting their performance in the following MEA testing sections.

The morphology, composition, size distribution, physical surface area, ECSA, ORR performance and durability of these catalysts have been presented and discussed. Though the PtH40 catalyst showed the highest ECSA (and smallest average particle size), the PtCo catalysts showed higher ORR activity, with signs of higher selectivity towards $H_2O_2$ production. PtCoU30 exhibited similar specific activity and higher mass activity compared to the PtCoT50 catalyst.

The PtCoT50 catalyst showed the highest catalyst durability, likely due to its high metal content and larger average particle size. PtH40 showed the best support durability. The PtCoT50 experienced the greatest loss in ECSA during support durability studies, likely due to its higher Pt/C ratio accelerating carbon degradation and facilitating Pt agglomeration.

Thin film RDE is a convenient, and quick screening tool to determine the activity of fuel cell catalyst and support material. The advantage of this technique over in-situ MEA testing is that it requires minimal catalyst, it can be performed in a day, and requires less infrastructure and equipment (Du et al., 2021; Riese et al., 2015). However, RDE cannot reflect many of the key parameters in a real-life fuel cell environment. Notably, AST performed in liquid electrolyte solution provides the worst scenario for the degradation of catalyst components, as water participates in the reactions (Nikkuni et al., 2015).

It is expected that In-situ MEA testing will confirm the higher activity of PtCo catalysts compared to Pt. The higher ORR activity of PtCoU30 compared to PtCoT50 seen in LSV may be reflected in the MEA results. However, the role of the ionomer, the influence of the catalyst layer structure as well as ionomer/catalyst interaction can only be seen from in-situ MEA performance and durability.

## 4.2 MEA ionomer optimisation

In-situ MEA performance is affected by ionomer content in the catalyst layer (CL). It has been shown that the amount of proton conducting ionomer in the CL can be optimised to maximise fuel cell performance, ensuring adequate reactant-catalyst interaction, without flooding the MEA (Gatto et al., 2015; Kim et al., 2010; Sasikumar, Ihm and Ryu, 2004; Qi and Kaufman, 2003). Insufficient ionomer may result in isolated catalyst particles, which cannot catalyse the reactions as they do not have access to a proton conducting pathway. Excessive ionomer content decreases performance by inhibiting electronic conduction paths (between platinum and carbon), thereby acting as an electronic insulator. Too much ionomer can physically block up gas transport channels in the catalyst layer, increasing mass transport resistance for reactants to reach the catalytic sites (Wang et al., 2019; Orfanidi et al., 2017). The hydrophilic nature of ionomers also means that excess ionomer will result in flooding of the catalyst layer, by retaining too much water, thereby inhibiting oxygen migration/diffusion to the catalytic sites (Kim et al., 2010).

To optimise the performance of the MEAs, PtCo-containing MEAs were produced and tested with increasing ionomer content. The in-house PtH40 MEAs were used as the benchmark. The ranges of ionomer contents used, and platinum loadings are shown in Table 4-5.

*Table 4-5: Ionomer content range and loadings for the respective catalysts.*

| Catalyst | Ionomer range investigated (wt %) |
|---|---|
| **PtCoU30** | 24 – 50 wt |
| **PtCoT50** | 20 – 28 |
| **PtH40** | 25 (optimised) |

As with ex-situ electrochemical characterisation, the catalyst ink preparation was adjusted for each catalyst to ensure optimal catalyst dispersion and deposition onto the substrates.

### 4.2.1 Ink optimisation

Ex-situ catalyst performance evaluation revealed that the PtCoT50 catalyst was more sensitive to the alcohol content in the ink preparation. A greater isopropanol to water

ratio was required to ensure adequate catalyst particle dispersion for PtCoT50 RDE electrochemistry, compared to the PtCoU30 and PtH40 catalysts. Figure 4-10 shows the in-situ electrochemical performance and ECSA of PtCoT50 MEAs prepared using different isopropanol to water ratios (3:1 and 1:1) and compared to PtH40 for reference. The cathode and anode loadings were 0.20 and 0.05 $mg_{Pt}/cm^2$ respectively, with 25 wt% cathode ionomer content for all the MEAs. Polarisation curves were obtained under automotive and stationary test conditions as described in section 3.3.5.

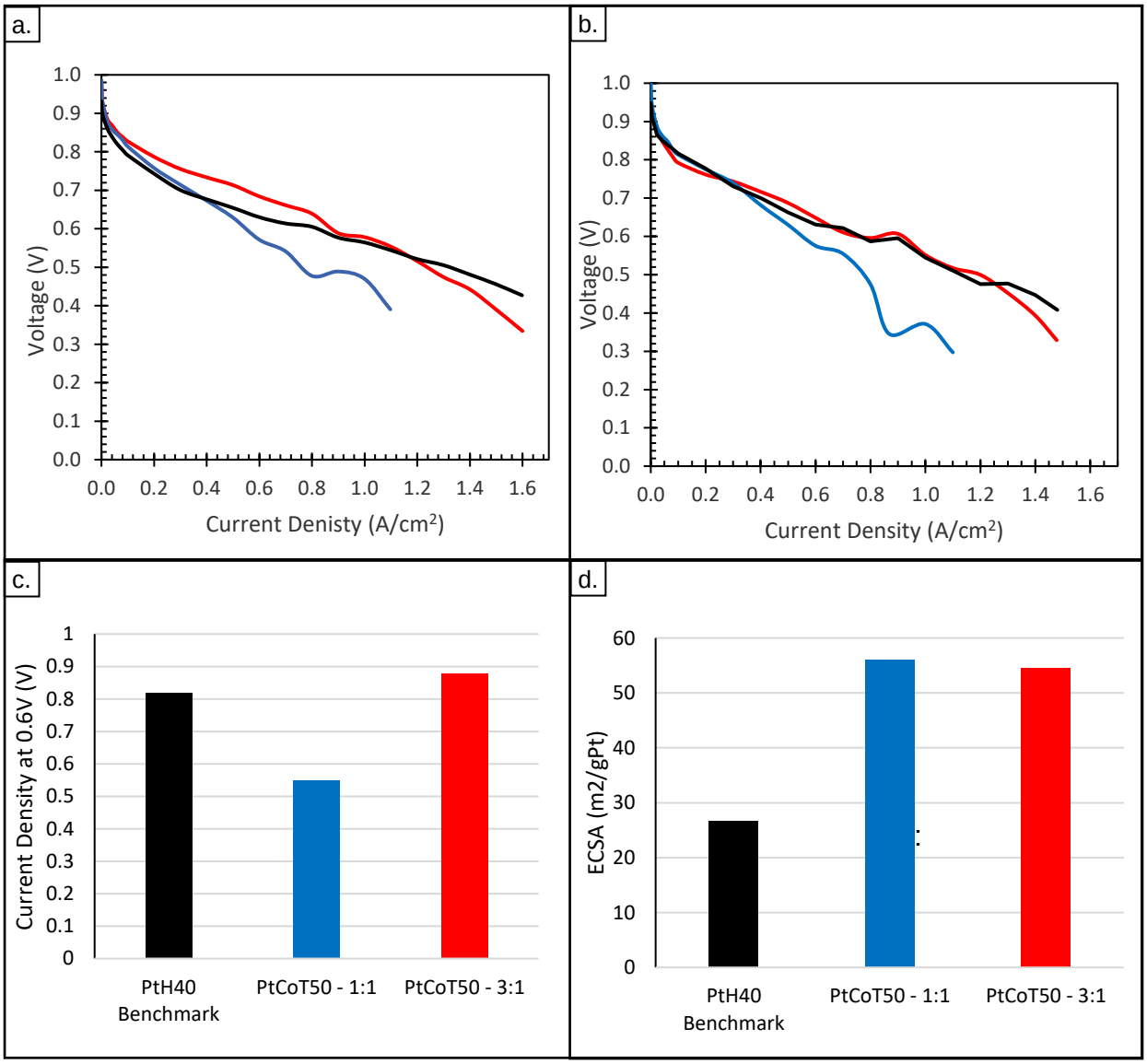


*Figure 4-10: Polarization curves for stationary (a) and automotive (b) conditions, as well as bar charts to display (c) the current density attained at 0.6 V and (d) the ECSA for the different isopropanol to water ratios in PtCoT50 MEA preparation.*

the PtCoT50 MEA prepared using a 3:1 IPA:water ratio yielded superior performance across all current densities, compared to the MEA prepared with the 1:1 ink. The PtCoT50-3:1 MEA performed better than the PtH40 benchmark at lower current

densities, however, at current densities greater than 1.2 A/cm$^2$, the PtCoT50 MEA suffers greater mass transport voltage losses. PtCoT50 – 3:1 had significantly larger current density at 0.6 V (as shown in d.), although the ECSA for PtCoT50-3:1 and PtCoT50-1:1 MEAs were remarkably similar ( 54 $m^2/g_{Pt}$ and 55 $m^2/g_{Pt}$ respectively). Increasing the isopropanol:water ratio in the PtCoT50 catalyst ink resulted in better dispersion of the catalyst particles and improved the accessibility of the active sites in the CCM. Kim et al. (2012) showed that increasing the 2-propanol to water ratio in the cathode catalyst ink preparation resulted in improved performance due to a reduction in the secondary particle aggregate sizes in the CL. This is supported by Takahashi et al. (2015) who showed that alcohol-rich inks produce well dispersed ionomer in the CL with a larger number of small agglomerates, compared to water-rich inks which had large agglomerates with poor agglomerate/ionomer interface This adapted isopropanol to water ratio is used for PtCoT50 MEA preparation in the following sections.

### 4.2.2 Impact of Ionomer content on performance and ECSA

#### *4.2.2.1 PtCoT50 ionomer optimisation*

PtCoT50 MEAs were prepared with ionomer contents of 20 wt%, 24 wt% and 28 wt%, as described in section 3.3. This range was selected based on the findings of (Kim et al., 2010) for low-loading MEA, with a high metal content catalyst. The impact of the ionomer content on PtCoT50 MEA performance was determined using polarisation curves and ECSAs.

Figure 4-11 shows the polarisation curves measured in stationary (a) and automotive (b) conditions, as well as the ECSA (c) and current densities at 0.6 V (d) to optimize the ionomer content in the PtCoT50 MEAs. At low current densities, where activation losses dominate, the ionomer content does not result in significant differences in performance. However, for current densities greater than 0.2 A/cm$^2$, the 28 wt% PtCoT50 MEA showed the greatest loss in voltage, followed by the 20 wt%, then 24 wt%.

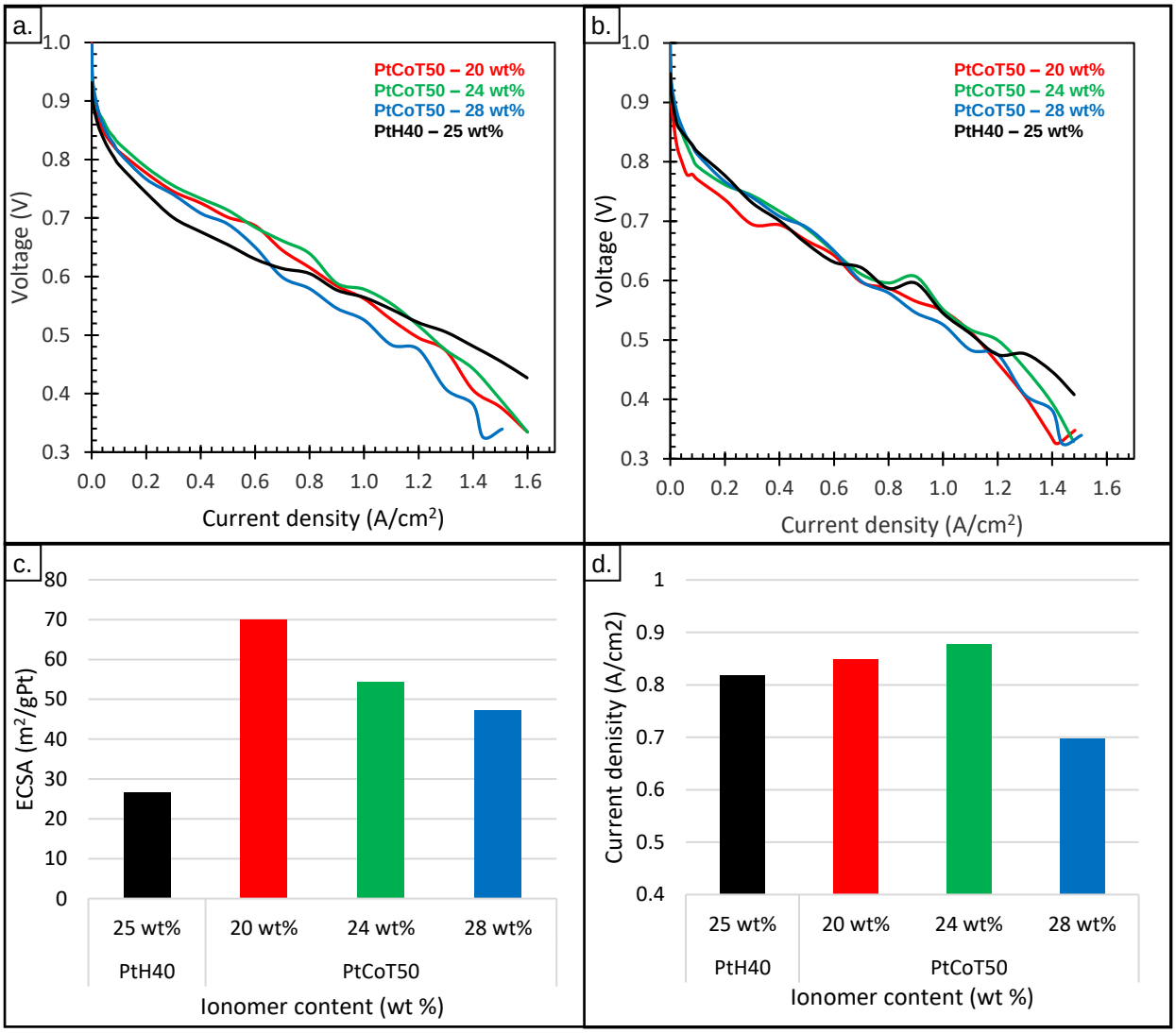


*Figure 4-11: Polarisation curves for stationary (a) and automotive (b) conditions, as well as bar charts to display electrochemical surface area (ECSA) (c) and the current density attained at 0.6 V (d) for the ionomer contents used in PtCoT50 MEAs.*

The PtCoT50 MEAs showed performances comparative to that of the PtH40 benchmark, but with greater performance losses at higher current densities.

Figure 5.11 (c) shows that the ECSA decreases for the PtCoT50 MEAs, as the ionomer content increases. Sasikumar, Ihm and Ryu, (2004) showed that available ECSA decreases when the excess ionomer starts acting as an electronic insulator, and/or a barrier to mass transport in the catalyst layer, owing to increased water retention by the hydrophilic ionomer. Excess ionomer isolates catalyst particles either from the gaseous phase, or the electron conducting phase, and thereby instead of improving the triple phase boundary distribution, hinders it. Figure 5.11 (d) shows that the 24

wt% ionomer content MEA has the greatest performance (0.87 A/cm$^2$ at 0.6 V compared to 0.84 A/cm$^2$ for the 20 wt % ionomer content), despite having a lower ECSA (54.4 m$^2$/g$_{Pt}$) than the 20 wt% ionomer content MEA (69.9 m$^2$/g$_{Pt}$). According to Kim et al., (2010) this behaviour is explained by the ionic resistance in the catalyst layer. When ionic resistance is high, accompanied by poor ionomer networks, the total ECSA cannot be fully utilised for electrochemical reactions. Therefore, while the 24 wt % MEA has a lower ECSA, it has greater proton conductivity (and performance), due to improved ionomer/catalyst interface. Above 24 wt% ionomer content the performance drops (0.69 A/cm$^2$ at 0.6V for the 28 wt% ionomer content MEA) likely due to excess water retention inside the hydrophilic pores (especially at higher current densities) resulting in greater mass transfer losses. The optimal ionomer content for the PtCoT50 catalyst at a loading of 0.25 mg$_{Pt}$/cm$^2$ is 24 wt%. Less ionomer results in insufficient proton conductivity, while more ionomer results in increased resistance and catalyst isolation. This result is consistent with the work done by Xu et al. (2007), who showed an optimal ionomer content of 25 wt%, using a 800 EW Nafion ionomer and a 53 wt% PtCo/C catalyst, similar to the PtCoT50 used here

#### *4.2.2.2 PtCoU30 ionomer optimisation*

50 cm$^2$ PtCoU30 MEAs were prepared with ionomer contents from 24 wt% up to 50 wt%, as described in section 3.3. This range is wider than what was used for PtCoT50, owing to the lower metal content in the catalyst. It has been shown that the optimal ionomer content, at a constant Pt loading, increases as metal content in a catalyst decreases (Kim et al., 2010). This is due to the larger catalyst layer thickness associated with lower metal content catalysts, at a specific CL loading, given the density difference between Pt (or PtCo) and carbon support. The 30 wt% metal PtCoU30 is therefore expected to be optimised at greater ionomer content than the 50 wt% metal content PtCoT50 catalyst. Polarisation curves were generated, and ECSA measurements conducted to establish the optimal ionomer content.

Figure 4-12 shows the polarisation curves generated under stationary (a) and automotive (b) conditions, as well as the ECSA (c) and current densities at 0.6 V (d) to optimize the ionomer content in the PtCoU30 MEAs. The PtH40 benchmark performance is included for reference. The trends in performance seen in (a) and (b) are the same, indicating that the optimal amount of ionomer is the same for both

stationary and automotive test conditions. The PtCoU30 MEAs with 24 wt%, 28 wt%, and 30 wt% ionomer content showed greater performance at all current densities compared to the PtH40 MEA. However, at ionomer contents greater than 35 wt%, the PtCoU30 performances decrease steadily to far below the PtH40 benchmark. Figure (d) shows that the current density increases to a maximum from 24 wt% (1.11 A/cm$^2$) to 30 wt% (1.28 A/cm$^2$) at 0.6 V, after which the performance steadily declines. Figure (c) shows that, like the PtCoT50 MEAs, the highest ECSA was obtained with the lowest ionomer content (72 m$^2$/g$_{Pt}$). As ionomer content increases, the ECSA decreases steadily.

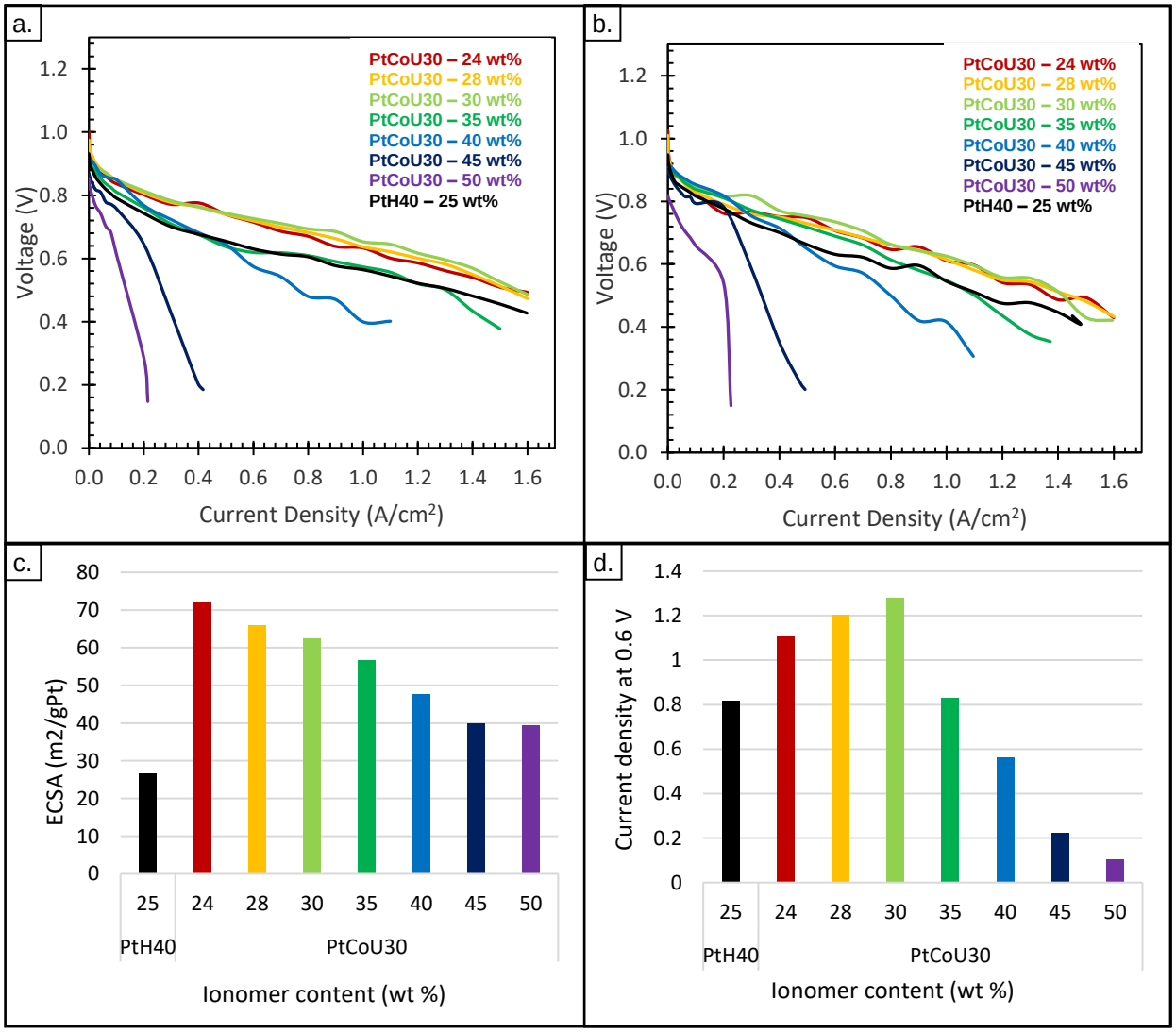


*Figure 4-12: Polarisation curves for PtCoU30 MEAs in stationary (a) and automotive (b) conditions. The ECSA (c) and the current density attained at 0.6 V (d) for increasing ionomer contents.*

The optimal ionomer content for the PtCoU30 catalyst (based on current density at 0.6 V) is 30 wt%. This is lower ionomer content than the optimal amount shown by Sasikumar, Ihm and Ryu (2004) for a similar MEA. They showed that, for a 30 wt% PtCo MEA at total loading of 0.25 $mg_{Pt}/cm^2$ the performance increased from 20 wt% ionomer content to a maximum performance at 40 wt% ionomer content. The performance declined at higher ionomer contents. However in their study, a Nafion 1035 ionomer was used. Xu et al. (2007) showed that the optimal ionomer content in PEMFC MEAs decreases with a decrease in equivalent weight of the ionomer used. Therefore, considering that the ionomer used in the current work is a low EW (720) SSC ionomer, it is to be expected that the optimal amount of ionomer (30 wt%) is lower than what was shown with the 1035 EW LSC Nafion ionomer in the work presented by Sasikumar, Ihm and Ryu (2004). The explanations for the optimal ionomer content are the same as described for the PtCoT50 MEAs. When ionic resistance is high, accompanied by poor ionomer networks, the total ECSA cannot be fully utilised for electrochemical reactions (at low ionomer contents). For PtCoU30 at 30 wt% ionomer content, an optimal 3-dimensional ionomer network exists to facilitate proton conduction to the available catalyst sites. Above 30 wt% ionomer content, excess ionomer reduced the performance by increasing mass transfer resistance, and resulting in flooding in the hydrophilic pores, especially at higher current densities (Kim et al., 2010).

### 4.2.3 Comparison of optimised MEAs

#### *4.2.3.1 Performance of Optimised PtCoU30 and PtCoT50 MEAs*

Figure 4-13 shows the polarisation curves for the optimised PtCoU30 and PtCoT50 MEAs generated under stationary (a) and automotive (b) conditions, as well as their ECSA (c) and current densities at 0.6 V (d). The PtH40 benchmark performance is included for reference, at the same anode and cathode Pt loadings (0.05 $mg_{Pt}/cm^2$ and 0.20 $mg_{Pt}/cm^2$ respectively). The PtCoU30 MEA with 30 wt % ionomer content shows the greatest performance under stationary and automotive test conditions, at all current densities. The PtCoT50 MEA shows performance comparable to that of the PtH40 benchmark at lower current densities, at high current densities (above1.2 $A/cm^2$) however, the PtCoT50 MEA shows larger voltage losses.

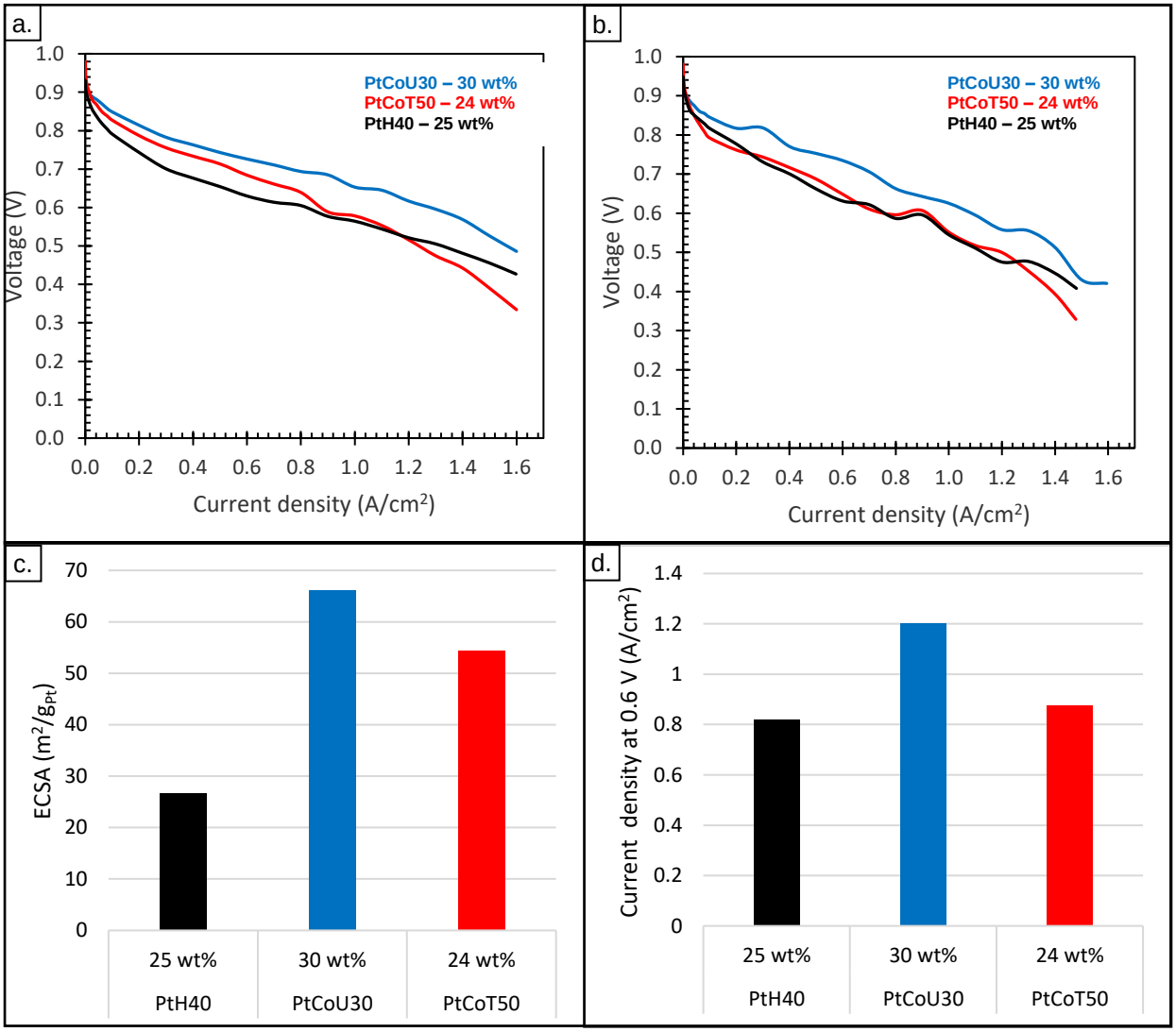


*Figure 4-13: Polarisation curves for stationary (a) and automotive (b) conditions; ECSA (c) and the current density attained at 0.6 V (d) for the best performing PtCoU30, PtCoT50 and PtH40 benchmark MEAs.*

The PtCoU30 MEA has the highest ECSA, and current density at 0.6 V (Figure 4-13). It is suggested that the higher optimal ionomer content in the PtCoU30 MEA (facilitated by the lower metal content, and corresponding larger volume of catalyst) allows for improved availability of electrochemically active sites, while mitigating the deleterious effects of excess ionomer, as seen in the decline in performance for PtCoT50 above 24 wt% ionomer content.

The in-situ MEA performance and ECSA results shown here are consistent with ex-situ RDE results shown in Section 4.1. The PtCo MEAs showed better performance compared to the PT benchmark, while the PtCoU30 MEA showed better performance than the PtCOT50 MEA. This is also consistent with the trend in mass activities and specific activities shown in Section 4.1. Similarly, the PtCoU30 MEA showed a higher ECSA than the PtCOT50 MEA, which is consistent with the particle size distribution and RDE ECSAs shown in the previous chapter. Furthermore, the PtCoT50 catalyst benefited from an increase in alcohol/water ratio, just as was seen for RDE ink preparation.

#### *4.2.3.2 MEA carbon corrosion AST*

Figure 4-14 shows the ECSA of the optimised PtCoU30 and PtCoT50 MEAs as a function of cycle number during 5000 cycles of carbon corrosion AST, compared to the PtH40 benchmark MEA.

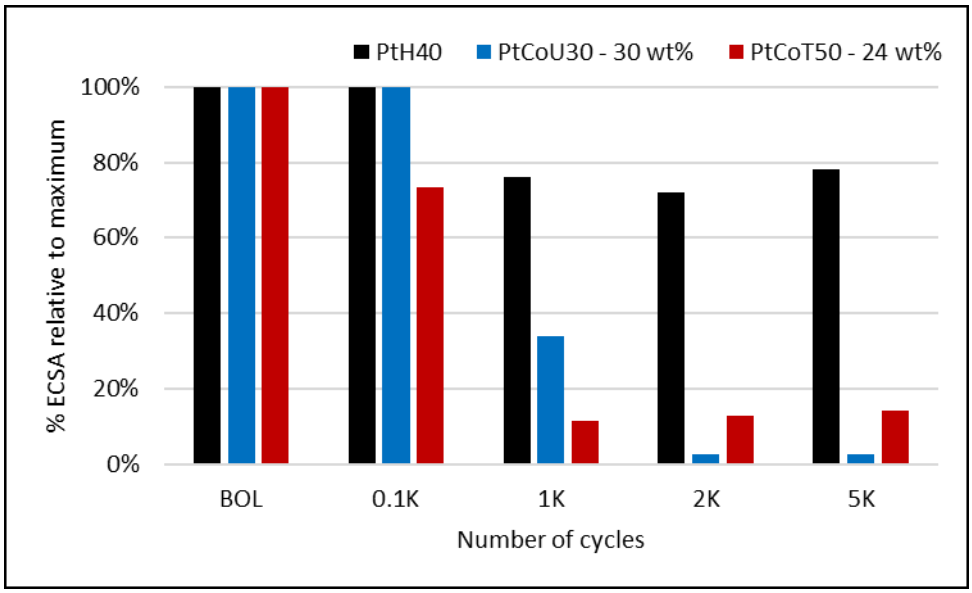


*Figure 4-14: ECSA as a function of cycle number for in-situ carbon corrosion AST on optimised PtCoU30 and PtCoT50 MEAs with PtH40 benchmark.*

The results showed that the PtCo catalysts lost significantly more ECSA (>80%) compared to the Pt catalyst (~20%) after 5000 cycles. This is contrary to what was shown by Nikkuni et al. (2015), where a 20 wt% PtCo/C MEA experienced a smaller reduction in ECSA compared to a 20 wt% Pt/C MEA, at similar loadings. However, the results are consistent with the trends seen in the ex-situ support durability AST. The RDE results showed a larger decrease in ECSA for PtCo electrodes compared to the Pt electrode. However, the in-situ results show a much larger decrease in ECSA for PtCoT50 (85% loss) and PtCoU30 (97% loss) than was observed during ex-situ support durability (11.9% and 22.0% for PtCoU30 and PtCoT50 respectively). This difference was expected, as has been discussed, due to the difference in degradation mechanisms between RDE and MEA environments, owing to the presence or absence of liquid electrolyte, which facilitates carbon corrosion, as well as he dependence of MEA ECSA on the structuring integrity of the catalyst layer (Nikkuni et al., 2015). The large drop in ECSA seen for MEA ASTs is associated with a total structural collapse, which is not seen in RDE ASTs.

This is likely due to the fact that at the same Pt loading, the PtCoU30 catalyst has significantly more carbon in the catalyst layer, and indeed a thicker catalyst layer overall, owing to its lower metal content (30 wt%) compared to PtT50 (50 wt%). This is supported by the BET surface areas shown previously (461 $m^2/g$ for PtCoU30 compared to 313 $m^2/g$ for PtCoT50 catalyst). It has been mentioned that PtCoT50 is supported on partially graphitised support, which may contribute to the improved stability, however, the specific differences in support structures were not extensively investigated in this thesis.

*4.2.3.3 MEA particle stability AST*

Figure 4-15 shows the ECSA of the optimised PtCoU30 and PtCoT50 MEAs as a function of cycle number during 10000 cycles of particle stability AST, compared to the PtH40 benchmark.

The ECSA loss for all MEAs was lower than for carbon corrosion testing. After 10 000 cycles the PtCoU30 MEA lost 24.1% and the PtCoT50 MEA lost 17% of the ECSA. The PtH40 MEA lost the most ECSA at 35%. This is consistent with what has been shown for Pt and PtCo particle stability in literature. Ball et al. (2006). Showed that, following particle stability AST in a 50 $cm^2$ MEA with cathode loading of 0.25 $mg_{Pt}/cm^2$ PtCo MEAs lost almost no ECSA, compared to a 60% loss for a Pt catalyst. This is largely due to the role that Cobalt plays as a sacrificial anode, carrying the oxidation current, and preferentially dissolving, thereby reducing Pt dissolution (Nikkuni et al., 2015). These results are also consistent with the ex-situ RDE catalyst durability AST results, which showed a greater loss in ECSA for the PtH40 catalyst, compared to the PtCo catalysts.

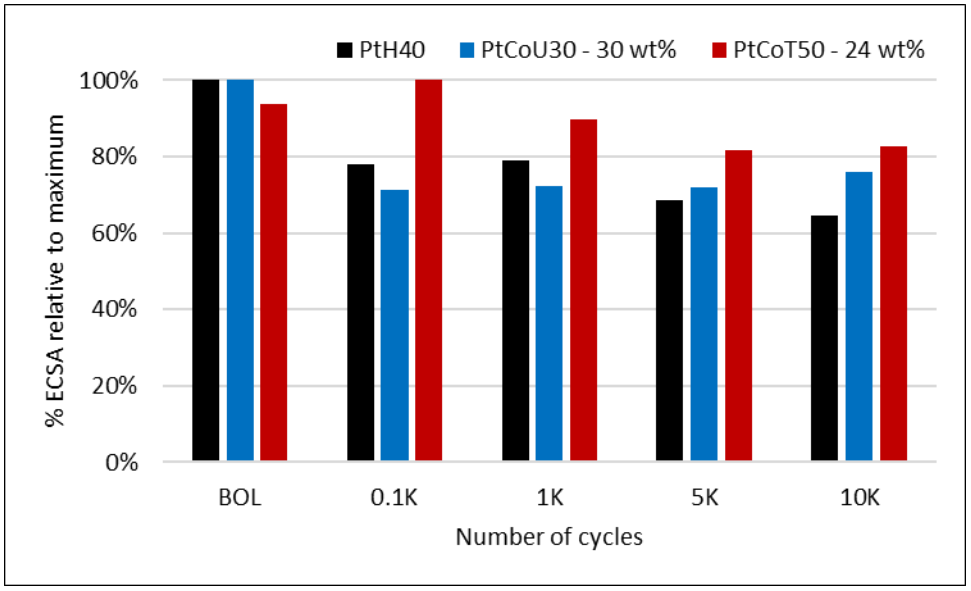


*Figure 4-15: ECSA as a function of cycle number for in-situ particle stability AST on optimised PtCoU30 and PtCoT50 MEAs with PtH40 benchmark.*

Figure 4-15 shows that PtCoU30 experienced a more rapid decline in ECSA than PtCoT50, which had an initial increase in ECSA followed by a gradual decline. Li et al. (2019) showed that the effect of particle stability testing on the ECSA and performance

of catalysts with higher metal contents (up to 50 %) was more appreciable, compared to lower metal content MEAs. When catalyst particles are further apart, they are less likely to suffer from catalyst degradation. The higher rate of ECSA loss in PtCoU30 is likely related to the significantly smaller average particle size (5.4 nm) compared to the larger PtCoT50 catalyst particles (7.1 nm), as well as a larger BOL ECSA

### 4.2.4 Section summary

The ionomer contents for PtCoU30 and PtCoT50 MEAs were optimised at 30 wt% and 24 wt% respectively. These ionomer contents showed the highest performance on polarisation curves. The optimal performance did not correspond to a maximum ECSA.

The in-situ MEA performance and ECSA results shown in this chapter are consistent with ex-situ RDE results shown in chapter 4.1. The PtCo MEAs showed better performance compared to the Pt benchmark, while the PtCoU30 MEA showed better performance than the PtCoT50 MEA. This is consistent with the trend in mass activities and specific activities shown in section 4.1. Similarly, the PtCoU30 MEA showed a higher ECSA than the PtCoT50 MEA, which is consistent with the particle size distribution and RDE ECSAs shown in the previous chapter. Furthermore, the PtCoT50 catalyst benefited from an increase in alcohol/water ratio, as was seen for RDE ink preparation. The PtCo MEAs lost significantly more ECSA than the Pt MEA in the in-situ carbon corrosion ASTs. However, for particle stability ASTs, the PtCo catalysts retained an higher ECSA than the PtH40 MEA. These trends are in agreement with what was observed for ex-situ ASTs.

Using the optimised ionomer content MEAs developed in this section, the following section will investigate the effects of heat treating all of the ionomer (1-phase) or a portion thereof (2-phase) with the catalyst and solvent. The differences in performance between PtCoT50 MEA and PtCoU30 MEA shown in this chapter revealed the impact of particle size and metal content on performance, ECSA and stability, however, the physical characteristics of the catalyst layer and influence of ionomer preparation need to be addressed.

## 4.3 Effect of Ionomer treatment on MEA performance, durability, and catalyst layer characteristics

During the ionomer optimisation in chapter 5.2, the ionomer/catalyst solution was dried to a powder. Thereafter, the powder was redispersed in solution to form the ink. The dried ionomer was in a single thermally treated phase. To increase the ionomer content for an MEA, additional ionomer was added directly to the ink, and was therefore not exposed to thermal treatment. These inks were then called 2-phase inks, indicating that the ionomer was present in two phases, or different states brought about by thermal treatment. Itota et al. (2022) investigated the effect of catalyst inks with and without thermal treatment on MEA performance and durability. They found that thermally treated inks resulted in improved performance due to a greater support/ionomer interface. However, the inks that were not thermally treated showed improved stability in MEA carbon corrosion testing, due to hydrophobic aggregates restricting water access, thereby prolonging the catalyst layer lifespan. The 1-phase inks investigated in the current work is similar to the thermally treated inks investigated by Itota et al. (2022), whereas the 2-phase inks represent a combination of the thermally treated and non-thermally treated.

In this section, the differences in catalyst layer characteristics and their effects on MEA performance and durability were investigated for PtCoU30 and PtCoT50 MEAs with 1-phase and 2-phase ink preparations. The aim was to investigate whether a combination of thermally treated and non-thermally treated ionomer would show combined benefits of thermally treated and non-thermally treated catalyst inks as shown by Itota et al. (2022). The PtH40 data is included throughout the chapter to serve only as a reference.

The relative amounts of dried (heat treated) ionomer and additional untreated ionomer in the PtCoU30 and PtCoT50 catalyst inks are shown in Table 4-6.

*Table 4-6: 1-phase and 2-phase ionomer contents for PtCoU30 and PtCoT50 catalyst inks*

| Catalyst | Phase | Dried ionomer content (wt%) | Final Ionomer content (wt%) |
|---|---|---|---|
| **PtCoT50** | 1-Phase | 24 | 24 |
| | 2-Phase | 20 | 24 |
| **PtCoU30** | 1-Phase | 30 | 30 |
| | 2-Phase | 24 | 30 |
| **PtH40** | 2-Phase | 15 | 25 |

### 4.3.1 Pore volume and pore size distribution

#### *4.3.1.1 PtCoU30*

Figure 4-16 shows the pore size distribution for PtCoU30 1-phase and 2-phase MEA catalyst layers (CLs), determined from Microporous Intrusion Porosimetry (MIP). Three distinct pore size regions were observed: 10-40 μm for pores between clusters of agglomerates, 20-300 nm for secondary pores, which exist between agglomerates, and <10 nm for primary pores, which exist inside particle agglomerates (Holdcroft, 2014).

The primary and secondary pore size distribution for 1-phase and 2-phase PtCoU30 catalyst layers were similar. The 2-phase CL showed a higher primary pore (4-6nm) volume compared to the 1-phase. The 2-phase also showed a broader range and larger volume of secondary pore sizes (20-300 nm) compared to the narrow 1-phase range (30-150 nm).

For pore sizes greater than 10 μm, the 1-phase PtCoU30 CL showed significantly larger intrusion volume than the 2-phase PtCoU30. The 1-phase MEA CL has larger channels between aggregates, which allows for higher mass transport. These results are consistent with the work by Itota et al. (2022) who showed MEA CLs made from thermally treated inks (40 wt% Pt on graphitised Vulcan) had significantly larger intrusion volume between aggregates compared to non-thermally treated inks, resulting in improved mass transport properties of the CLs. They showed that the thermally treated inks resulted in smaller loosely packed aggregates, compared to large, densely packed aggregates which had significantly smaller pore volume.

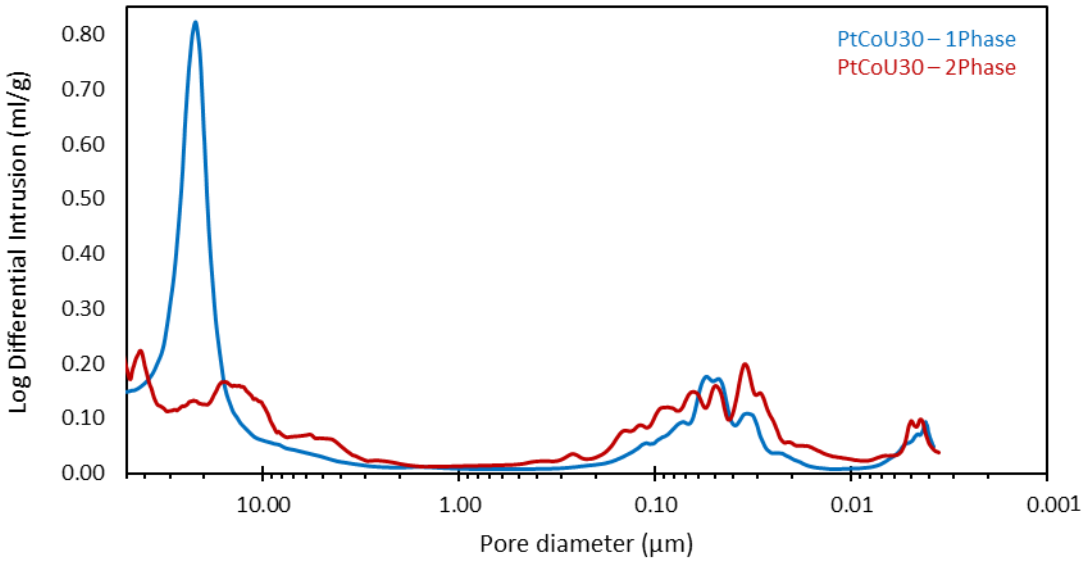


*Figure 4-16: Pore size distribution for PtCoU30 1-phase and 2-phase MEA catalyst layers*

The cathode catalyst layer thickness for the BOL 1-phase and 2-phase PtCoU30 MEAs were 11.2 µm and 16.7 µm respectively, determined from cross sectional SEM images. At the same catalyst layer loading, it is expected that the thicker 2-phase CL would be more porous, however, the intrusion volume shown in Figure 4-16 suggests less pore volume for the thicker catalyst layer. This may be due to the second phase of non-heat-treated ionomer forming clusters and filling the larger pore, which reduces the overall pore volume, despite having a thicker CL.

#### *4.3.1.2 PtCoT50*

Figure 4-17 shows the pore size distribution for PtCoT50 1-phase and 2-phase MEA CLs, determined from MIP. As was observed for the PtCoU30 catalyst, three pore size regions were observed in the PtCoT50 samples: 10-40 µm for pores between clusters of agglomerates, 20-300 nm for secondary pores, which exist between agglomerates, and <10 nm for primary pores, which exist inside particle agglomerates.

The 1-phase PtCoT50 CL showed greater overall primary and secondary pore volumes and wider pore size distribution. The 2-phase CL showed narrow peaks of larger primary (~4 nm) and secondary (~15 nm) pore volumes.

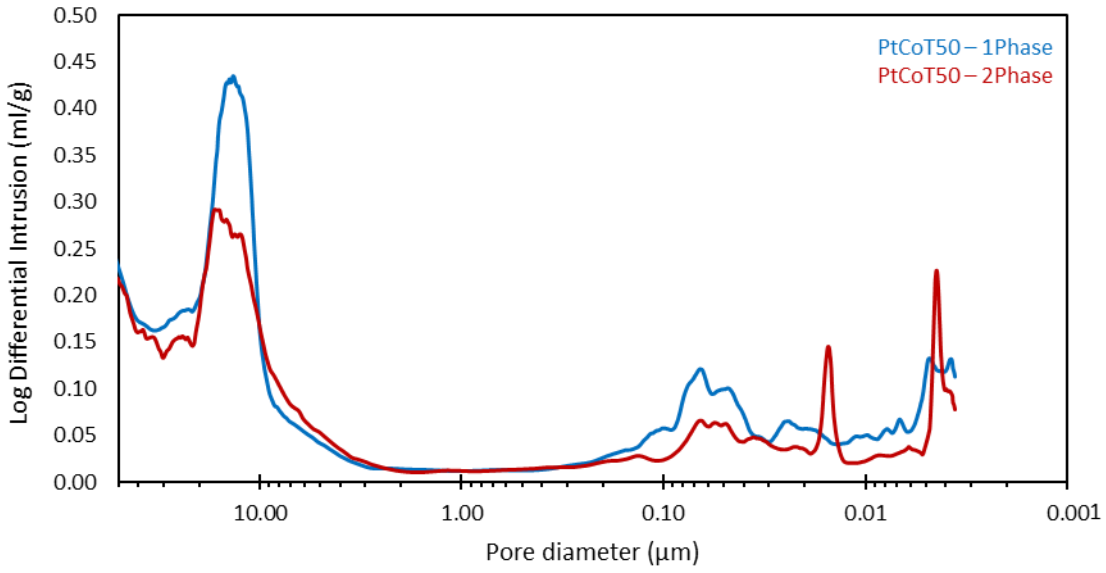


*Figure 4-17: Pore size distribution for PtCoT50 1-phase and 2-phase MEA catalyst layers*

As with the PtCoU30 samples, the 1-phase PtCoT50 CL showed significantly larger intrusion volume for pore sizes greater than 10 μm indicating that the channel sizes between aggregates of particle agglomerates were larger. This is supported by through-plane gas permeability studies, which were performed on 1-phase and 2-phase PtCoT50 GDEs. The Gurley numbers for the 1-phase and 2-phase samples were 7.8 s/100ml and 13.2 s/100ml respectively, which indicate that the 1-phase PtCoT50 catalyst layer was significantly more permeable to flow compared to the 2-phase PtCoT50 sample. These results are consistent with the work by Itota et al. (2022) who showed MEA CLs made from thermally treated inks (40 wt% Pt on graphitised Vulcan) had significantly larger intrusion volume between aggregates compared to non-thermally treated inks, resulting in improved mass transport properties of the CLs. They showed that the thermally treated inks resulted in smaller loosely packed aggregates, compared to large, densely packed aggregates which had significantly smaller pore volume.

The cathode catalyst layer thickness for 1-phase and 2-phase PtCo50 MEAs were 6.1 μm and 5.7 μm respectively. Unlike the PtCoU30 MEAs, there is very little difference in CL thickness for the 1-phase and 2-phase PtCoT50 MEAs. However, from the pore size distribution in Figure 4-17 it is inferred that, with a smaller pore volume, and similar CL thickness, the 2-phase CL must be denser than the more porous 1-phase CL.

This indicates that the 1-phase and 2-phase ink preparations do not interact with the higher metal/ lower carbon content PtCoT50 MEA in the same way as PtCo30. This may be due to the differences in the types of carbon support. As has been mentioned, PtCoT50 is supported on partially graphitised carbon. Itota et al. (2022) showed that graphitised support form hydrophobic compacts with ionomer, whereas non-graphitised support forms more hydrophilic compacts between ionomer side chains and the support. Yoshimune and Harada (2019) showed that the greater available carbon surface area (and larger Pt-Pt distances) in lower metal loading Pt catalysts allow for facile adsorption of ionomer onto the carbon support. Ionomer/catalyst interaction therefore strongly depends on the composition of the catalyst itself. It may be that the ionomer phase has less impact on the higher metal content catalyst, due to the smaller available carbon surface area, as well as the graphitised nature of support.

### 4.3.2 Electrochemical performance

#### *4.3.2.1 Electrochemical impedance studies*

Beginning of life (BOL) contributions to resistance for 1-phase and 2-phase MEAs were determined using EIS performed at a frequency of 0.1 A/cm$^2$ across a frequency range of 20 kHz to 0.1 Hz, and fitted with a simple Randle circuit model (Yuan et al., 2010). At this low current density, the charge transfer resistance dominates and the mass transfer and ohmic resistances are considered negligible. The charge transfer resistance provides insight into the availability of electron transfer routes in the different catalyst layer structures produced from 1-phase or 2-phase inks (Yuan et al., 2010). Figure 4-18 shows the Nyquist plots for 1-phase and 2-phase (a) PtCoU30 and (b) PtCoT50 MEAs. PtCoT50 had a negligible difference in the charge transfer resistance between 1-phase and 2-phase (3.97 Ω ), as can be seen from the similar distance between the 1-phase and 2-phase semi-circle intercepts (Figure 4-18 b). PtCoU30 showed a slight decrease in charge transfer resistance between 1-phase and 2-phase (3.58 Ω and 3.52 Ω respectively), which is apparent in Figure 4-18 (a) from the smaller distance between the 2-phase semi-circle intercepts.

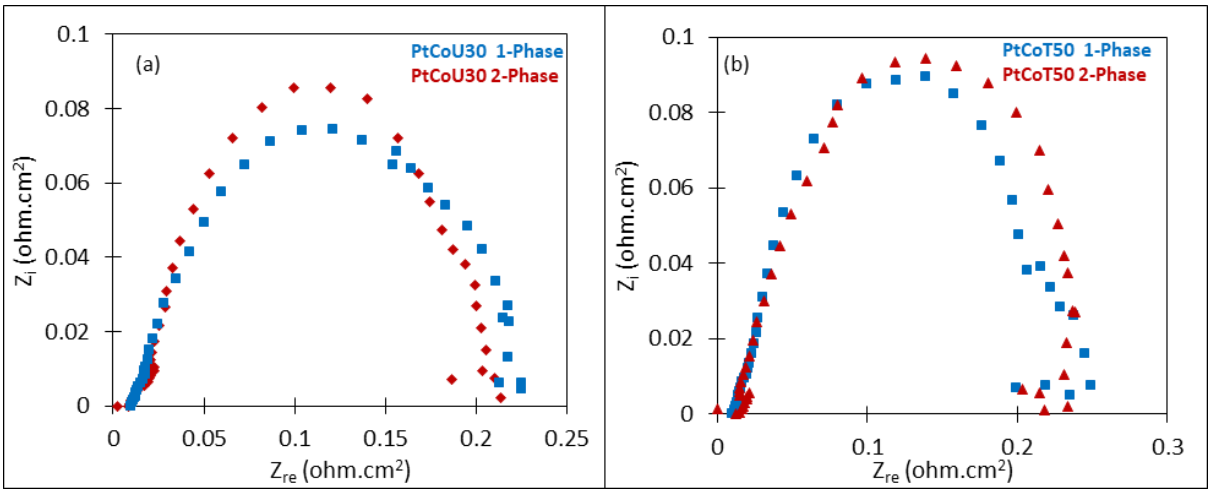


*Figure 4-18: Nyquist plots for 1-phase and 2-phase (a) PtCoU30 and (b) PtCoT50 MEAs*

This indicates that for the lower metal content PtCo catalyst, there may be a slight benefit in electronic conductivity for the ionomer/catalyst interface resulting from a 2-phase ink. Itota et al. (2022) showed that a heat-treated ink preparation resulted in significantly lower charge transfer resistance than a non-heat-treated MEA. They ascribed the difference to the conductive support being coated or insulated with ionomer in the non-heat-treated MEA. In the current work, it is suggested that having

a portion of ionomer heat treated (2-phase) is sufficient to ensure comparable charge transfer to the MEAs prepared with 1-phase inks. The addition of non-heat-treated ionomer does not reduce the beneficial electron-transfer effects of heat treating the ionomer with the catalyst.

### 4.3.3 Polarisation curves

#### *4.3.3.1 PtCoU30 1-phase vs 2-phase electrochemical performance*

Figure 4-19 shows the polarisation curves obtained under stationary and automotive conditions, as well as bar charts showing current density at 0.6 V and ECSA, for 1-phase and 2-phase 30 wt% ionomer content PtCoU30 MEAs.Figure 4-19 (a) and (b) shows that the 1-phase 30 wt% PtCoU30 MEA performed better than the 2-phase PtCoU30 MEA across all current densities in both sets of conditions.

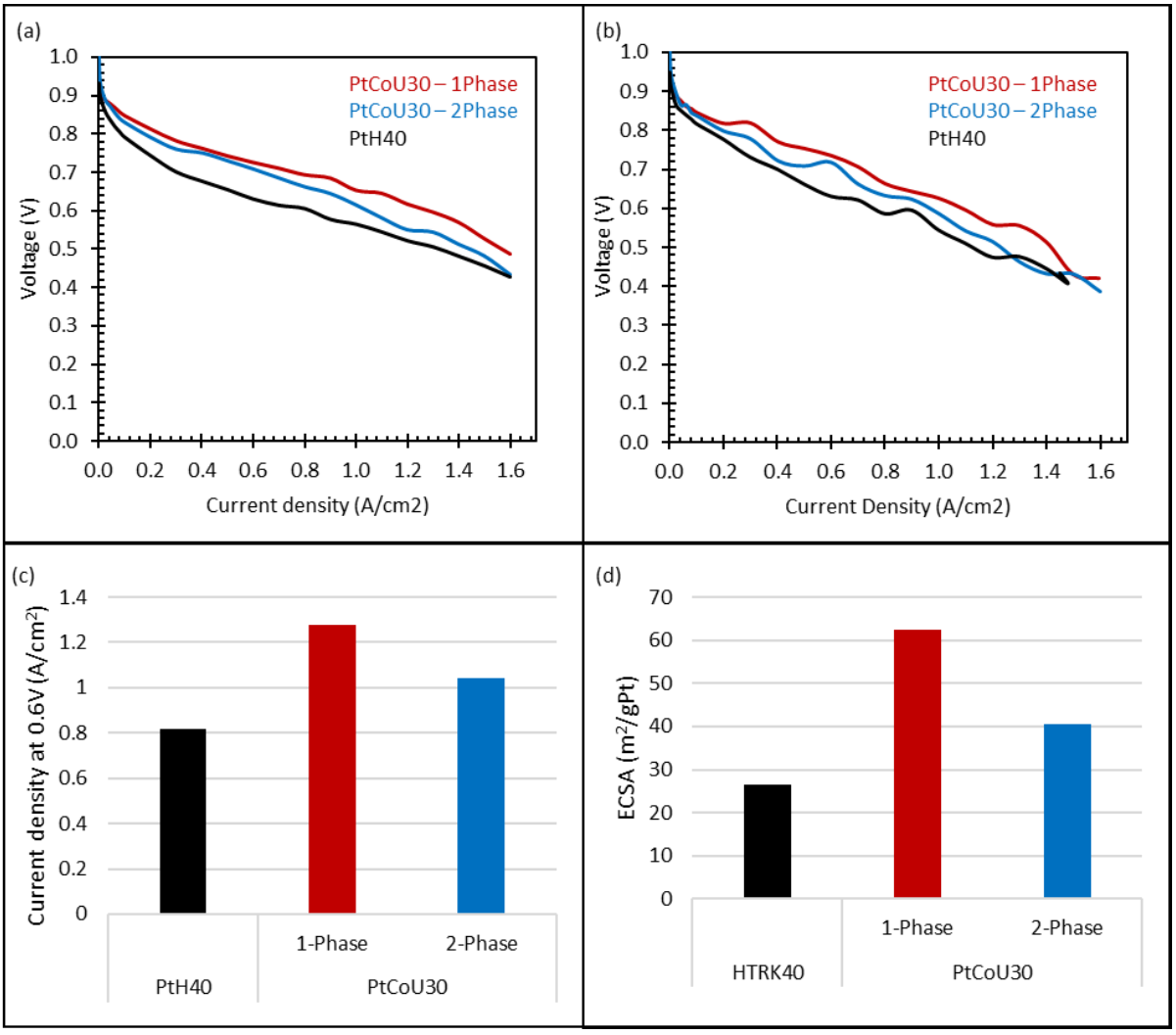


*Figure 4-19: Polarization curves under stationary (a), and automotive (b) test conditions, as well as the current density at 0.6 V (c) and ECSA (d), for 1-phase and 2-phase 30 wt% ionomer content PtCoU30 MEAs and PtH40 reference.*

The 2-Phase PtCoU30 showed increasing performance losses with increasing current density compared to the 2-phase PtCoU30. Figure 4-19 (c) illustrates the large difference in current density at 0.6 V, where the 1-phase performed 23% better than the 2-phase. Figure 4-19 (d) shows that the 2-phase PtCoU30 also had 35% lower ECSA compared to the 1-phase. The reduced ECSA of the 2-phase is likely due to an increase in ionically isolated catalyst particles caused by reduced ionomer/catalyst interface. In section 4.3.1 it was shown that the 2-phase MEA CL is thicker, and less porous than the 1-phase CL, suggesting that the ionomer that was not heat-treated (the wet phase ionomer) likely clogged the pore volume, thereby isolating clusters of catalyst. The reduced performance is due to the increased ohmic resistance and reduced mass transfer capacity (to remove water and supply gaseous reagents) associated with the 2-phase ionomer. Itota et al. (2022) showed similar results for heat-treated catalyst supported in GV40, compared to non-heat-treated catalyst; above 0.7 A/cm$^2$ the heat-treated catalyst performed significant better, with larger ECSA and lower charger transfer resistance. They attributed the high resistance, poor ECSA, and performance to the large ionomer/catalyst aggregates and small interfaces seen in the non-heat-treated catalyst inks.

#### *4.3.3.2 PtCoT50 1-phase vs 2-phase electrochemical performance*

Figure 4-20 shows the polarisation curves obtained under stationary and automotive conditions, as well as bar charts of the current density at 0.6 V and the ECSA, for 1-phase and 2-phase 24 wt% ionomer content PtCoT50 MEAs and PtH40 reference.

Figure 4-20 (a) and (b) shows that, the 1-phase 24 wt% ionomer PtCoT50 MEA performed better than the 2-phase 24 wt% PtCoT50 MEA, for both sets of conditions.

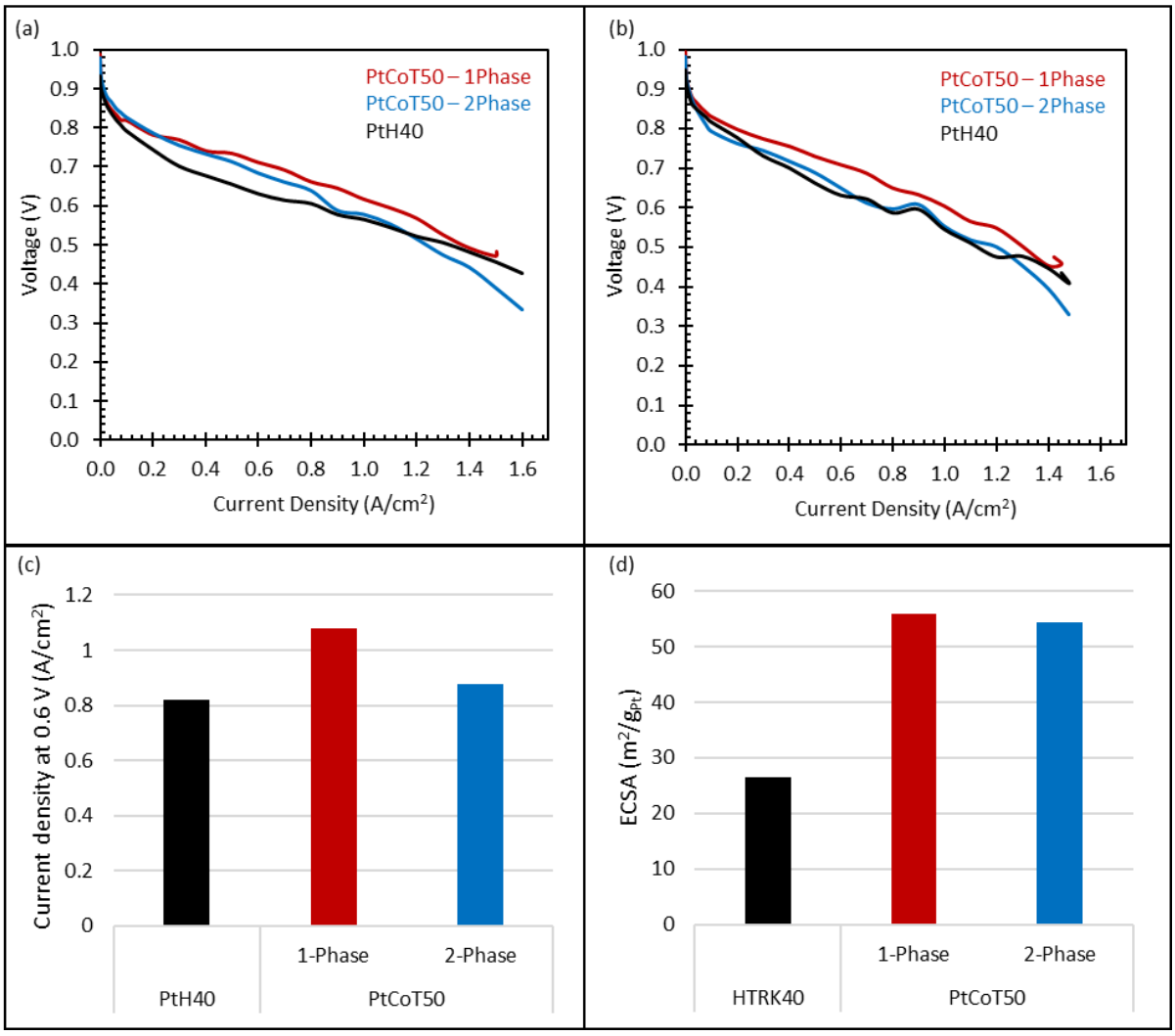


*Figure 4-20: Polarisation curves under stationary (a), and automotive (b) conditions, as well as the current density at 0.6 V (c) and ECSA (d), for 1-phase and 2-phase 30 wt% ionomer content PtCoT50 MEAs and PtH40 reference.*

The PtCoT50 results are consistent with what was observed for PtCoU30. The 2-phase PtCo50 MEA showed slightly greater activation losses than the 1-phase in the activation region (0.0 A/cm$^2$ to 0.2 A/cm$^2$), while Ohmic (0.2-1.2 A/cm$^2$) and mass transfer (>1.2 A/cm$^2$) losses were much more pronounced for the 2-phase PtCoT50. Figure 4-20 (d) illustrates the difference in current density at 0.6 V, where the 1-phase performed 23% better than the 2-phase. Figure 4-20 (c) shows a less pronounced difference in ECSA between 1-phase and 2-phase PtCoT50 compared to that of PtCoU30 MEAs. As was discussed for the PtCoU30 MEAs, the reduced ECSA of the 2-phase is likely due to ionic isolation of catalyst particles. Again, as was postulated for the PtCoU30 MEAs, the reduced performance seen in the 2-phase PtCoT50 MEA is due to the increased ohmic resistance and reduced mass transfer capacity. These results are consistent with the work shown by Itota et al. (2022), as discussed under PtCoU30 performance.

The difference between 1-phase and 2-phase PtCoT50 performance and ECSA was not as significant as was observed for PtCoU30. This may be due to the differences in metal and carbon content of PtCoU30 and PtCoT50. At the same Pt loading, PtCoU30 has a thicker catalyst layer and relative amount of carbon, compared to PtCoT50. These results suggest that a higher carbon content catalyst benefits more from incorporating the ionomer with the catalyst in a drying step, thereby improving the catalyst/ionomer interface. A thicker catalyst layer necessarily requires adequate mass transfer channels and extended ionomer networks, whereas for a thinner catalyst layer (as is the case for PtCoT50), the deleterious effects of decreased mass transfer channels and increased ohmic resistance is not as severely evident in performance. Catalysts with higher Pt/C ratios, and resulting thinner CLs (as is the case for PtCoT50) have a higher proportion of Pt located on the carbon surface, and therefore ECSA is less susceptible to limitations in CL porosity (Li et al., 2019). As has been discussed, PtCoT50 is supported on graphitised carbon, which increases its hydrophobicity, and results in hydrophobic catalyst ionomer compacts (Itota et al., 2022). This characteristic likely contributes to the difference in the ionomer interface seen between PtCoT50 and PtCoU30 for 1-phase and 2-phase formulations. However, the nature of the different supports was not investigated extensively in the current work.

### 4.3.4 Electrochemical durability

#### *4.3.4.1 Carbon Corrosion accelerated stress tests*

*PtCoU30*

Figure 4-21 shows the ECSA as a function of cycle number for *in-situ* carbon corrosion accelerated stress test (AST) on 1-phase and 2-phase PtCoU30 MEAs. The 1-phase ECSA remained unchanged for the first 100 cycles, after which a steep decline was observed (>60 % loss after 1000 cycles), showing complete degradation after 5000 cycles. The 2-phase experienced an initial increase in ECSA after 100 cycles, followed by a smaller decline in ECSA (53% loss compared to 66% loss for the 1-phase).

The small change in ECSA after 100 cycles is consistent with the stages of carbon corrosion proposed by Hu et al., (2021). They showed that initially, carbon support corrosion results in some particle loss, while mass transfer performance remains unchanged. Micropores become progressively larger and supporting structure thinner with a reduction in triple phase boundary, but a small amount of performance and ECSA loss occurs here. The sharp decline in ECSA above 1000 cycles is consistent with the next stage in carbon corrosion described by Hu et al., (2021). In this final stage the increasingly fragile support structure becomes unable to support the packing force. The catalyst layer abruptly collapses, filling micropores and leaving a dense mass of support. This is associated with a sharp drop in ECSA and performance.

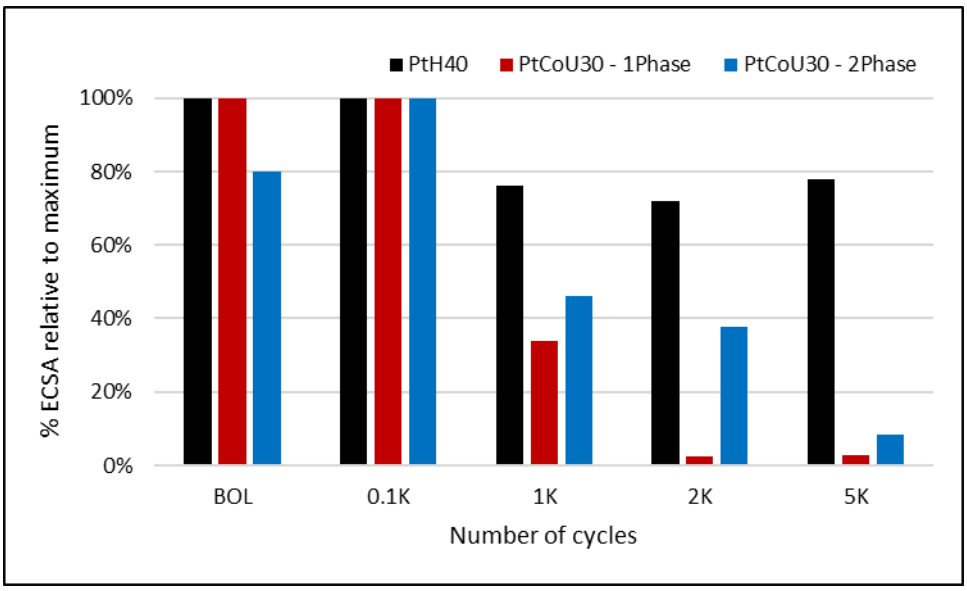


*Figure 4-21: ECSA as a function of cycle number for in-situ carbon corrosion AST on 1-phase and 2-phase PtCoU30 MEAs with PtH40 benchmark*

The results shown Figure 4-21 indicate that the portion of ionomer that was not dried with the catalyst (2-Phase) provides a measure of protection against carbon corrosion. This is likely due to the smaller pore volume observed by MIP in the 1-phase MEA. It has been shown that carbon corrosion is accelerated in CLs with larger pore areas, due to the ease of oxidants accessing the carbon support (Du et al., 2021). The 2-phase catalyst layer may also have reduced corrosive water contact by providing alternative water transport channels, separated from the catalyst agglomerates. The initial increase in ECSA for the 2-phase MEA was likely due to previously inaccessible catalyst sites becoming available following the widening of micropores in the first stage of carbon corrosion, as described by Hu et al., (2021).

These results are consistent with the *in-situ* carbon corrosion study on heat-treated and non-heat treated catalyst inks shown by Itota et al. (2022). They proposed that the increased rate of support degradation in heat treated samples was due to the increased wetting properties seen in heat treated ionomer/support interfaces, resulting in accelerated carbon corrosion.

Figure 4-22 shows Cross sectional SEM images of (a) 1-Phase PtCoU30 and (b) 2-Phase PtCoU30 MEAs after 5 000 cycles of carbon corrosion AST. The 1-phase catalyst layer appeared relatively smoothly distributed, apart from the apparent crack. The 2-phase sample exhibited multiple large breaks in the catalyst layer. The change in catalyst layer thickness from BOL to EOL conditions for both 1-phase and 2-phase was also determined from SEM images. The 1-phase MEA went from 11.2 μm to 5.8 μm, whereas the 2-phase went from a larger BOL thickness of 16.7 to 6.3 μm

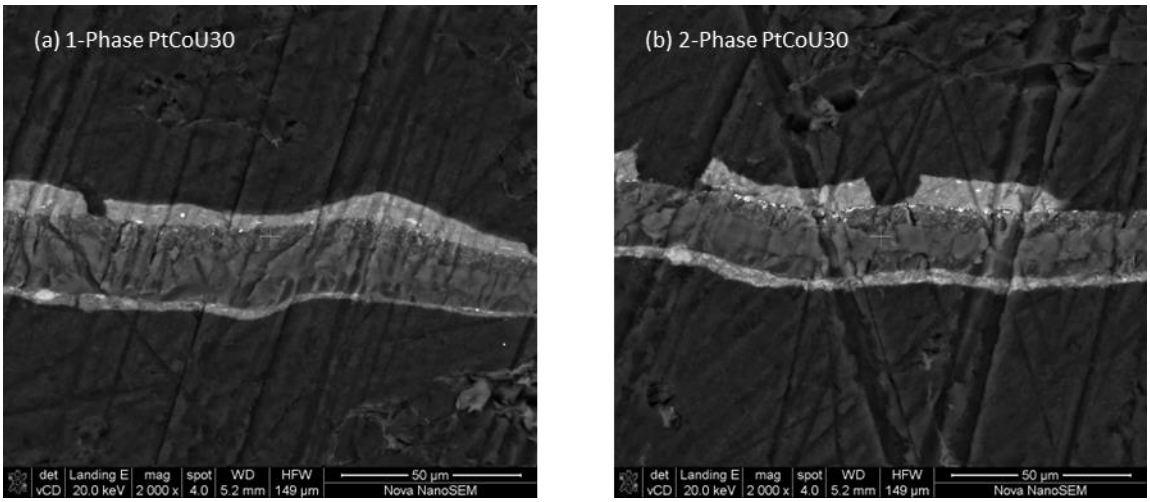


*Figure 4-22: Cross sectional SEM images of (a) 1-Phase PtCoU30 and (b) 2-Phase PtCoU30 MEAs after 5 000 cycles of AST. (Cathode: top layer)*

The 2-phase lost a greater percentage of CL thickness (62 % compared to 48 % for 1-phase), however, the CL thickness and ECSA after 5000 cycles remained greater than the 1-phase. It should be noted that the 2-phase MEA had significant breaks in the CL, constituting severe disruption of the in-plane electronic conductivity.

EDX elemental analysis was performed on the EOL samples in three regions: cathode layer, membrane adjacent to cathode, and membrane adjacent to anode. It was observed that the EOL 1-phase and 2-phase MEA cathodes consisted of 35.0 wt% Pt and 34.4 wt% Pt respectively. However, the membrane adjacent to the cathode in the 2-phase MEA showed significantly more Pt (19.3 wt%) compared to the 1-phase (8.8 wt%). Normalising the Pt content to the respective Flourine signals in the membrane showed that the 2-phase MEA experienced more than double the amount of Pt intrusion into the membrane compared to the 1-phase (1-phase Pt/F:0.29; 2-phase Pt/F: 0.12). Despite having lost significantly more Pt to the membrane, the 2-phase MEA showed a smaller decline in ECSA compared to the 1-phase. This may be associated with a more robust catalyst layer structure, owing to the smaller pore volume limiting corrosion, and the slightly thicker EOL catalyst layer structure. The addition of non-heat-treated ionomer likely confers a structural protection from CL collapse. However, the 2-phase CL exhibited multiple large breaks, and twice the amount of Pt intrusion into the membrane. Unfortunately polarisation curves could not be performed in this study to assess the EoL performance of the 1-phase and 2-phase MEAs due to instrument limitations.

*PtCoT50*

Figure 4-23 shows the ECSA as a function of cycle number for *in-situ* carbon corrosion AST on 1-phase and 2-phase PtCoT50. The PtCoT50 MEAs experienced significant losses in ECSA after 1000 cycles. This behaviour was consistent with what was observed with the PtCoU30 MEAs. Initially, carbon support corrosion results in limited particle loss, while mass transfer performance remains unchanged (first 100 cycles). Micropores become progressively larger and supporting structure thinner with a reduction in triple phase boundary, but minimal loss of performance and ECSA occurs here. The sharp decline in ECSA above 1000 cycles is consistent with the next stage in carbon corrosion described by Hu et al., (2021). In this final stage the increasingly fragile support structure becomes unable to support the packing force. The catalyst

layer abruptly collapses, filling micropores and leaving a dense mass of support. This is associated with a sharp drop in ECSA and performance.

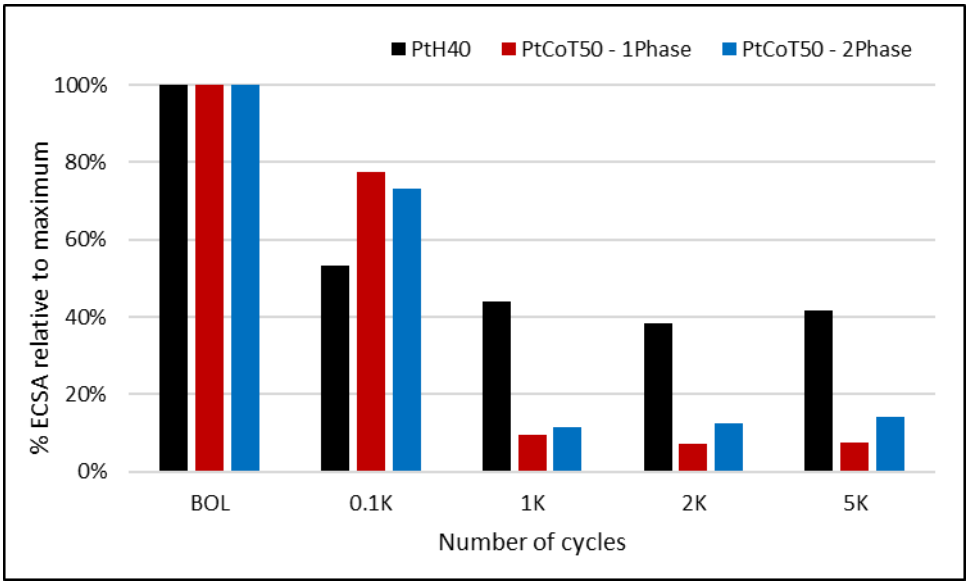


*Figure 4-23: ECSA as a function of cycle number for in-situ carbon corrosion AST on 1-phase and 2-phase PtCoT50 MEAs with PtH40 benchmark*

Compared to the PtCoU30 results, the PtCoT50 showed very little difference in ECSA loss between the 1-phase and 2-phase MEAs after 5000 cycles (92.4% loss for 1-phase and 85.8% loss for 2-phase). The 2-phase MEA showed only slightly smaller loss in ECSA compared to the 1-phase. This is consistent with the fact that the differences in 1-phase and 2-phase performance were more pronounced in the PtCoU30 MEAs than for the PtCoT50 MEAs. For PtCoU30 there was a significant benefit in performance for the 1-phase MEA, and a contrasting benefit for carbon corrosion stability for the 2-phase MEA. The effects of the ionomer treatment are therefore likely more significant for catalysts with lower metal content (higher carbon/catalyst ratio, and thicker catalyst layers). Yoshimune and Harada (2019) showed that the ionomer shell thickness and density in the CL depends on the Pt loading. They showed that a 30 wt% Pt/C catalyst had lower ionomer shell thickness and higher ionomer shell density compared to a 50 wt% Pt/C catalyst. This difference was attributed to the decrease in Pt-Pt distance for the higher Pt loading catalyst, which inhibited facile ionomer-carbon adsorption due to the smaller available carbon surface area.

Figure 4-24 shows the cross-sectional SEM images of (a) 1-Phase PtCoT50 and (b) 2-Phase PtCoT50 MEAs after 5000 cycles of carbon corrosion AST. It was determined that the 1-phase and 2-phase PtCoT50 MEA cathode catalyst layers lost 27.2 % (6.1 μm to 4.4 μm) and 61.1% (5.7 μm to 2.2 μm) from BOL to EOL, respectively. The EOL 1-phase MEA appears visibly thicker, with a rougher irregular surface. Despite similar losses in ECSA during carbon corrosion AST, the 2-phase MEA lost significantly more catalyst layer thickness, unlike what was observed in PtCoU30 samples. The heat - treated portion of ionomer in the 2-phase PtCoT50 did not contribute to improved carbon corrosion stability. This may be explained by the high metal content and correspondingly lower carbon presence, compared to the lower metal content PtCoU30.

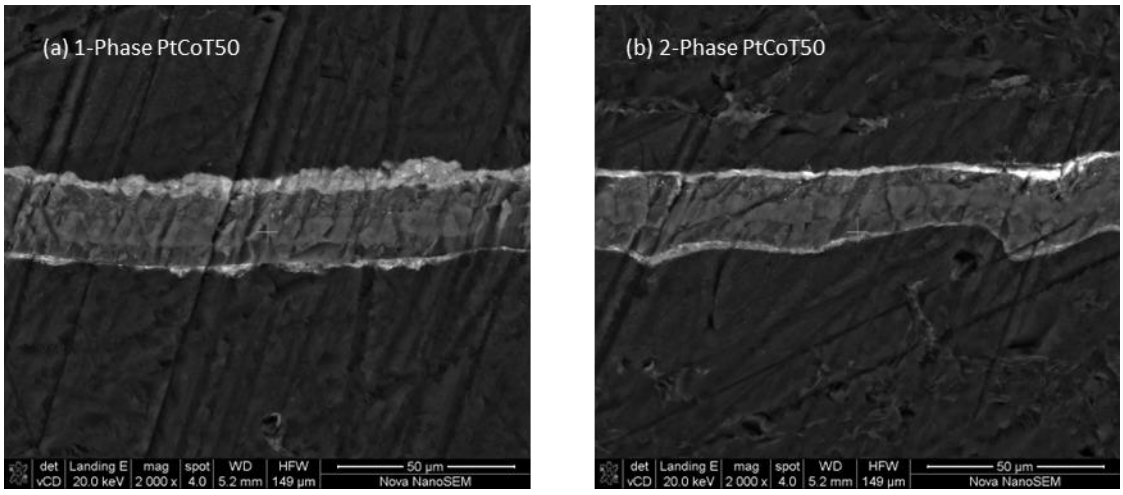


*Figure 4-24: Cross sectional SEM images of (a) 1-Phase PtCoT50 and (b) 2-Phase PtCoT50 MEAs after 5000 cycles of AST. (Cathode: top layer)*

EDX analysis showed that 2-phase MEA suffered more significantly from Pt intrusion into the membrane as evidenced by the Pt to F weight ratio in the membrane adjacent to the cathode catalyst layer. The 1-phase showed Pt/F ratio of 0.13 compared to 0.26 for the 2-phase. This is consistent with the results shown for PtCoU30 MEAs. The 2-phase MEA is more susceptible to Pt deposition in the membrane, however, the rate and absolute amount of ECSA loss is lower for the 2-phase compared to the 1-phase MEAs. This suggests that while Pt dissolution and migration, as well as CL thickness loss is enhanced in the 2-phase MEAs during carbon corrosion, the structural benefits (larger particle agglomerate sizes) allow for retention and slowed rate of ECSA loss.

#### *4.3.4.2 Particle stability accelerated stress test*

PtCoU30

Figure 4-25 shows the ECSA as a function of cycle number for *in-situ* particle stability testing on 1-phase and 2-phase PtCoU30 MEAs. Figure 4-25 shows that the 1-phase PtCoU30 experienced an initial rapid decline of 28.8% after 100 cycles, after which the ECSA remained relatively stable. The 2-phase PtCoU30 MEA showed a more gradual decline in ECSA, with a total decrease of 13.9% after 10 000 cycles. The incorporation of a portion of non-heat-treated ionomer (2-phase) to the heat-treated ionomer/catalyst ink conveyed a protective effect, improving the particle stability. The increased rate of Pt dissolution migration and coalescence in the 1-phase MEA can be attributed to the larger BOL ECSA (62.3 $m^2/g$) and greater inter-agglomerate pore volume, compared to the 2-phase MEA, which had significantly lower BOL ECSA (40.5 $m^2/g$)

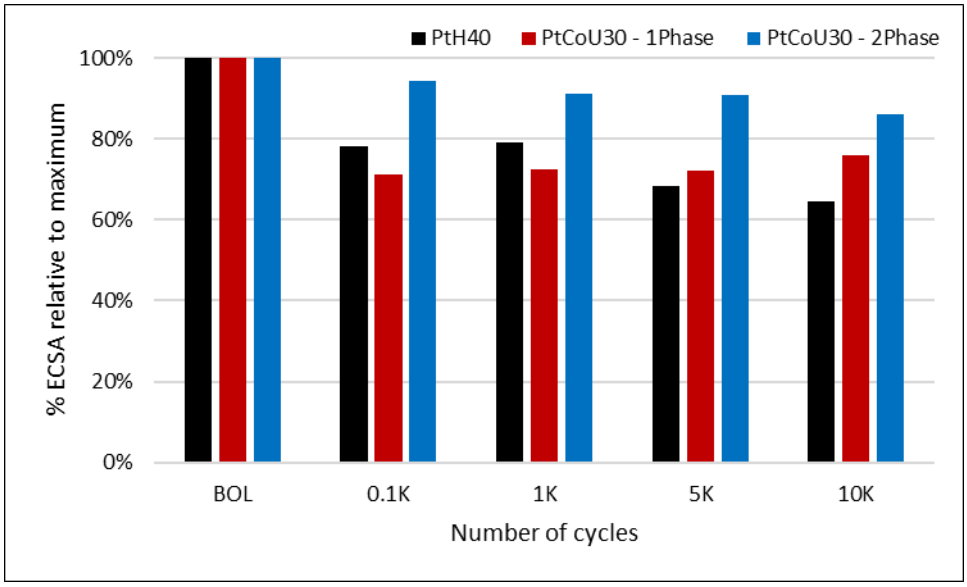


*Figure 4-25: ECSA as a function of cycle number for in-situ particle stability AST on 1-phase and 2-phase PtCoU30 MEAs with PtH40 benchmark*

Figure 4-26 shows the cross-sectional SEM images of (a) 1-Phase PtCoU30 and (b) 2-Phase PtCoU30 MEAs after 10 000 cycles of particle stability testing. The 1-phase cathode CL showed visible cracks after particle stability AST, whereas the 2-phase CL is visibly intact and thicker. Here the 1-phase MEA lost 29.8 % in CL thickness (11.2 µm to 7.9 µm) compared to the 2-phase (12.3%; 16.7 µm to 14.6 µm). From EDX analysis it was determined that the amount of Pt deposition in the membrane next to the cathode was similar for 1-phase and 2-phase MEAs, with Pt/F weight ratios of 0.12

and 0.91 respectively. Despite losing similar amounts of Pt to the membrane, the 2-phase PtCoU30 MEA showed improved particle stability in terms of catalyst layer thickness and EOL ECSA.

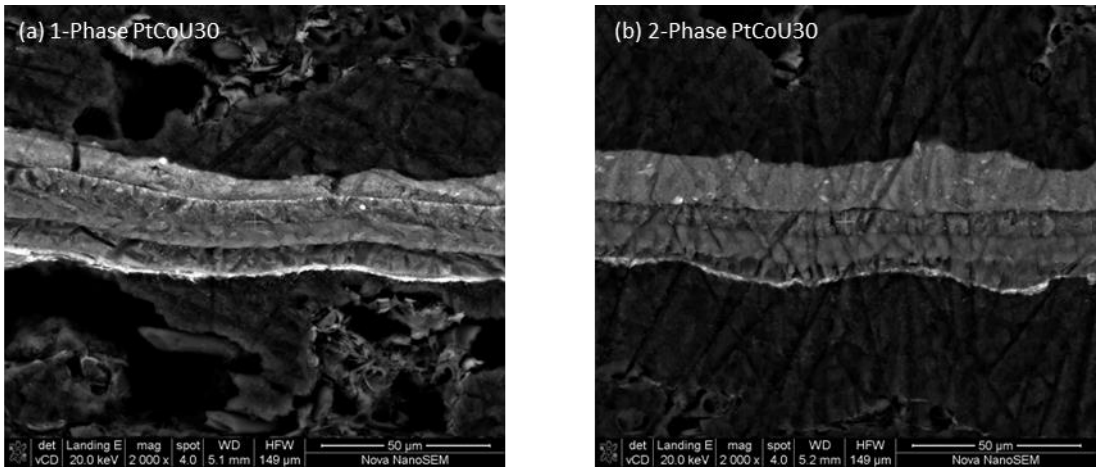


*Figure 4-26: Cross sectional SEM images of (a) 1-phase PtCoU30 and (b) 2-phase PtCoU30 MEAs after 10 000 cycles of particle stability AST. (Cathode: top layer)*

PtCoT50

Figure 4-27 shows the ECSA as a function of cycle number for *in-situ* particle stability AST on 1-phase and 2-phase PtCoT50 MEAs. As with the PtCoU30 MEAs, the PtCoT50 MEAs (both 1-phase and 2-phase) showed improved stability compared to the Pt catalyst, as has been shown in literature (Ball et al., 2006).

Both 1-phase and 2-phase PtCoT50 MEAs showed an initial increase in ECSA. This was not observed for PtCoU30 and is likely due to the higher Pt and Co density in this catalyst layer, resulting in poorer dispersion, and higher relative amount of subservice Pt particles that become exposed during initial surface Pt and Co dissolution. This initial increase has been shown in literature (Papadias et al., 2018). The 1-phase PtCoT50 MEA showed greater ECSA stability compared to the 2-phase MEA, again indicating that the 2-phase formulation does not convey the same benefit that it does to the lower metal content PtCoU30 catalyst. Here, the smaller pore volume and ionomer aggregates do not provide protection for Pt dissolution.

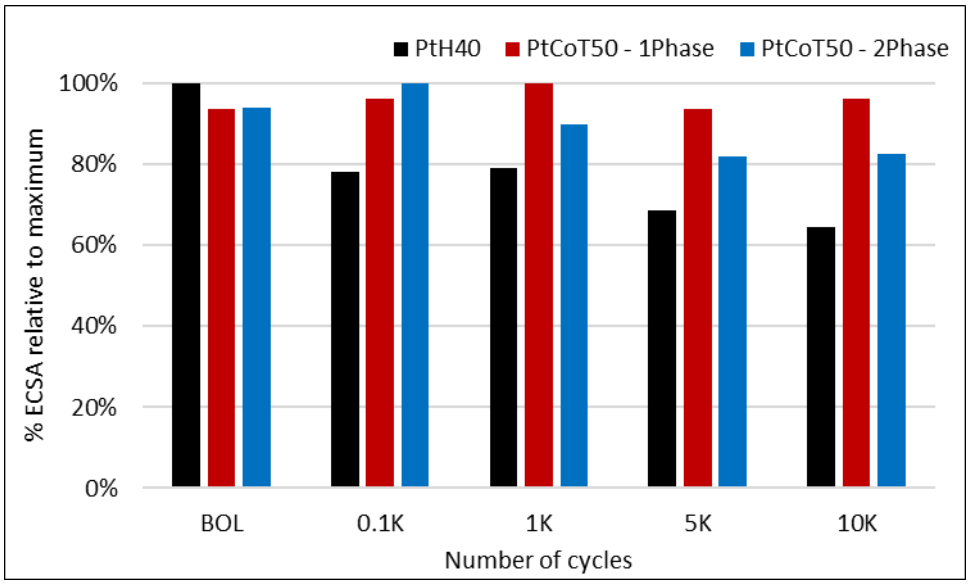


*Figure 4-27: ECSA as a function of cycle number for in-situ particle stability AST on 1-phase and 2-phase PtCoT50 MEAs with PtH40 reference.*

Figure 4-28 shows the cross-sectional SEM images of (a) 1-Phase PtCoT50 and (b) 2-Phase PtCoT50 MEAs after 10 000 cycles of particle stability AST. Here, as was observed for carbon corrosion AST, the 1-phase MEA exhibited a thicker average EOL cathode CL (5.2 μm) compared to the 2-phase MEA (3.9 μm). From BOL to EOL the 1-phase MEA lost 14.3 % (6.1 μm to 5.2 μm), whereas the 2-phase MEA lost 30.9 % (5.7 μm to 3.9 μm). EDX revealed that the Pt/F signal in the membrane adjacent to the cathode was significantly higher for the 1-phase (0.41) compared to the 2-phase (0.16).

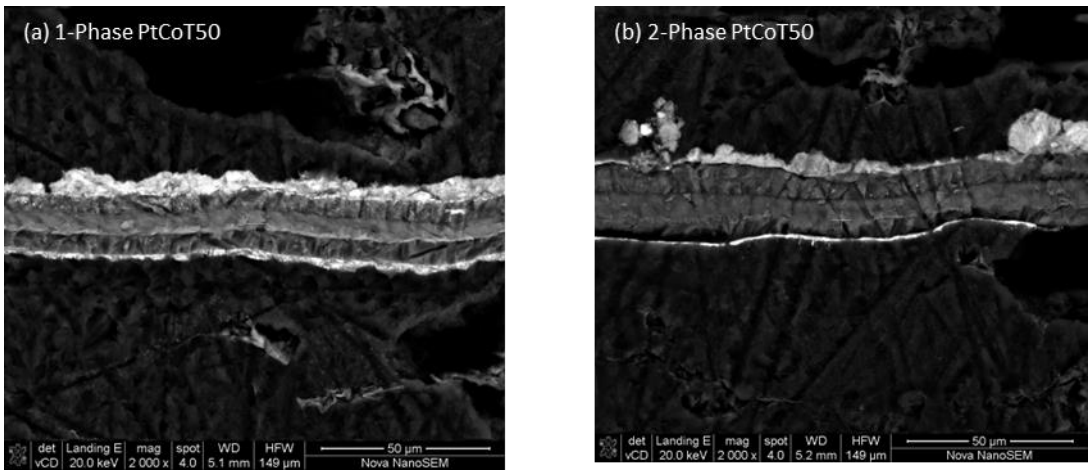


*Figure 4-28: Cross sectional SEM images of (a) 1-Phase PtCoT50 and (b) 2-Phase PtCoT50 MEAs after 10 000 cycles of particle stability testing. (Cathode: top layer)*

PtCoT50 MEAs do not enjoy the same benefit from the 2-phase ionomer treatment as the PtCoU30 MEAs. The 1-phase PtCoT50 MEA showed superior performance, carbon corrosion and particle stability characteristics compared to the 2-phase. Whereas for PtCoU30, the 1-phase MEA clearly outperformed the 2-phase, while the 2-phase showed higher stability. This difference in behaviour is ascribed to the metal content of the catalyst material. The thicker catalyst layer in the PtCo30 MEAs is more susceptible to ionomer aggregates blocking pore volume, thereby reducing PtCo particle utilisation and mass transfer, while providing a protection from corrosion and particle dissolution during stability ASTs. The thinner PtCoT50 CL showed a smaller difference in pore volume distribution for the 1-phase and 2-phase ionomer ink formulations, suggesting that the 2-phase ionomer formulation does not affect the CL to the same extent as the PtCoU30 CL. This may be due to the partially graphitised carbon support in PtCo50 catalyst.

For higher metal content catalysts, there is no benefit in incorporating ionomer in a second phase. Both performance and durability were improved in the 1-phase formulation. However, when the metal/carbon ratio is lower, such as the case of PtCoU30, the structural changes observed in the 2-phase MEA (notably the smaller inter-agglomerate pore volume) results in poorer performance, but improved carbon corrosion and particle stability.

### 4.3.5 Design for a low PGM MEA

This thesis investigated the physical and electrochemical characteristics of two commercial PtCo/C catalysts and an in-house Pt benchmark for PEMFCs. Ex-situ electrochemical characterisation provided insight into the catalytic activity, durability and ECSA of these catalysts. The MEA ionomer content was optimised for the two PtCo/C catalysts with a cathode and anode loading of 0.20 $mg_{Pt}/cm^2$ and 0.05 $mg_{Pt}/cm^2$ respectively. Lastly the effect of ionomer ink treatment was investigated to determine whether the performance and/or durability could be improved by incorporating 2-phases of ionomer.

Figure 4-29 shows a radar chart comparing key outcomes for the 1-phase and 2-phase PtCo MEAs, compared to the PtH40 Benchmark.

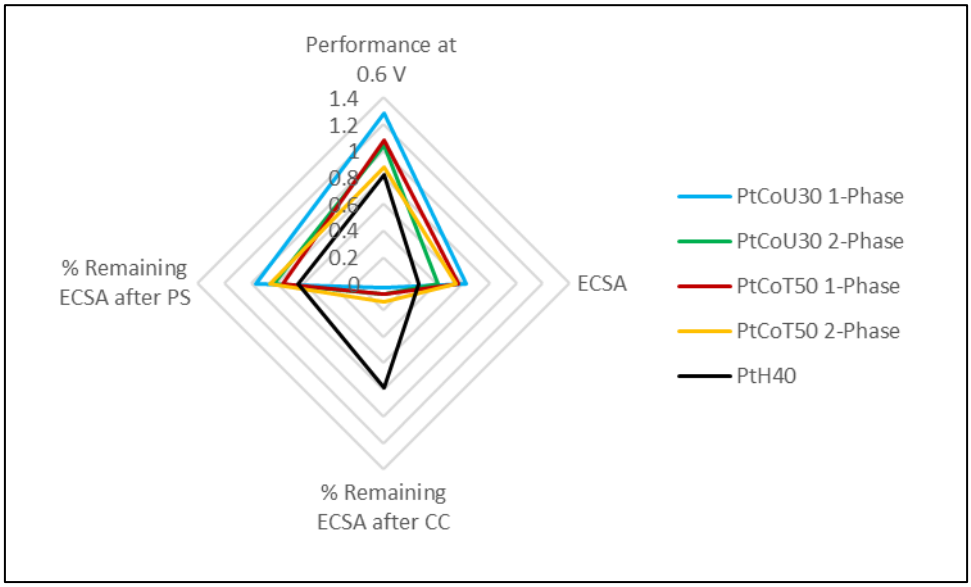


*Figure 4-29: Radar chart of 1-phase and 2-phase PtCo MEA performance.*

The parameters used for this visual comparison are:

1. MEA performance at 0.6V (A/cm$^2$)
2. Beginning of Life ECSA
3. Percentage ECSA loss after Carbon Corrosion AST
4. Percentage ECSA loss after Particle Stability AST

Figure 4-29 shows that the 1-phase PtCoU30 MEA has the greatest performance at 0.6 V, the highest BOL ECSA, and retains the most ECSA following particle stability AST. PtH40 showed the greatest resistance to ECSA loss following carbon corrosion AST, however, it performed the worst in the other three categories shown here. The two PtCoT50 MEAs do not match the 1-phase PtCoU30 MEA.

Based on these findings a 30 wt% PtCo/C MEA with 30 wt% ionomer content in 1-phase is the recommended design for a low PGM PtCo MEA given the current ink formulation and coating technology.

# 5 Conclusions and recommendations

## 5.1 Conclusions

The overarching goal of this project was to suggest a high performing and low PGM MEA design using a PtCo alloy catalyst. The first step in the selection of the appropriate catalyst was to determine the morphology, composition, size distribution, physical surface area, ECSA, ORR performance and durability of two commercial PtCo catalysts, (PtCoU30 and PtCoT50) against a Pt benchmark (PtH40).

The alcohol/water ratio in the PtCoT50 catalyst ink was optimised in order to produce good quality RDE thin films. It was shown that although the PtH40 catalyst showed the highest ECSA (and smallest average particle size), the PtCo catalysts showed higher ORR activity, despite signs of higher selectivity towards $H_2O_2$ production. PtCoU30 exhibited similar specific activity and higher mass activity compared to the PtCoT50 catalyst. The PtCoT50 catalyst showed the highest catalyst durability, likely due to its high metal content and larger average particle size. The smaller particle size and higher initial ECSA of the PtCoU30 catalyst resulted in a greater loss in ECSA during catalyst durability AST. PtH40 showed the best support durability. The PtCoT50 experienced the greatest loss in ECSA during support durability studies, likely due to its higher Pt/C ratio accelerating carbon degradation and facilitating Pt agglomeration.

The second objective was to optimise the MEA ionomer content used for two commercial PtCo catalysts to select the best performing catalyst for low loading PEMFCs. The optimal ionomer content, for the best performance, was 24 wt% and 30 wt% for the PtCoT50 and PtCoU30 MEAs respectively. This suggested that the higher metal content catalyst (PtCoT50) required less ionomer than the PtCoU30, due to the thinner catalyst layer thickness. Both optimised PtCo MEAs outperformed the PtH40 benchmark. This was illustrated by the current density at 0.6 V, which were 1.28 A/cm$^2$, 0.88 A/cm$^2$, and 0.82 A/cm$^2$ for PtCoU30, PtCoT50 and PtH40 respectively. This trend was consistent with the activities seen in ex-situ RDE. The effect of catalyst properties on MEA durability was studied by In-situ carbon corrosion and particle stability ASTs. The carbon corrosion ASTs showed that the PtCo catalysts lost significantly more ECSA (>80%) compared to the Pt catalyst (~20%) after 5000 cycles. After 10 000 cycles of particle stability the PtCoU30 MEA lost 24% and the PtCoT50 MEA lost 17%

of the ECSA. The PtH40 MEA lost the most ECSA at 35%. The improved particle stability of the PtCo MEAs was attributed to the protective role Co played as a sacrificial anode during Pt degradation. It was concluded that the 30 wt% ionomer content PtCo30 was the best performing MEA.

Finally, the effect of catalyst ink preparation (1-phase and 2-phase) on performance and durability for two commercial PtCo catalysts was determined. It was shown that for PtCoU30 and PtCoT50, the 1-phase ink formulation resulted in significantly better performance, whereas there was a slight benefit in terms of carbon corrosion and particle stability for the 2-phase formulation for both PtCoU30 and PtCoT50 MEAs. The improved stability was largely due to a reduction in CL pore volume, preventing degradation of isolated particles. The minor benefit of the 2-phase ionomer formulation, in terms of stability, was less significant compared with the reduced performance. Therefore, it was recommended that the 1-phase PtCoU30 is the best MEA for use in either stationary or automotive application.

## 5.2 Recommendations

For future ionomer optimisation trials, it is recommended that the phase of ionomer be kept constant when a range of ionomers are tested. In the current thesis, a 1-phase ionomer ink was made, to which additional ionomer (2-phase) was added in order to achieve a higher desired ionomer content. The results of this thesis have shown that a 1-phase MEA is not comparable to a 2-phase MEA. It is therefore recommended that ionomer optimisation be done solely with 1-phase inks, or indeed with inks in which the ionomer received the same amount (or lack) of heat treatment.

Furthermore, it is recommended that PtCo be the preferred catalyst in future technology development for low loading MEAs, compared to Pt, given the significant and consistently improved performance. PtCo catalysts also exhibited improved particle stability. However, in both ex-situ and in-situ carbon corrosion ASTs, Pt/C outperformed both PtCo/C catalysts. Therefore, if an MEA with high resistance to carbon corrosion is desired, then a Pt/C MEA is recommended.

# 6 References


Ball, S., Theobald, B., Thompsett, D. and Hudson, S. 2006. Enhanced Durability of PtCo catalysts for PEMFC. *ECS Meeting Abstracts*. MA2005-02(33):1178–1178. DOI: 10.1149/ma2005-02/33/1178.

Banham, D. and Ye, S. 2017. Current status and future development of catalyst materials and catalyst layers for proton exchange membrane fuel cells: An industrial perspective. *ACS Energy Letters*. 2(3):629–638. DOI: 10.1021/acsenergylett.6b00644.

Bing, Y., Liu, H., Zhang, L., Ghosh, D. and Zhang, J. 2010. Nanostructured Pt-alloy electrocatalysts for PEM fuel cell oxygen reduction reaction. *Chemical Society Reviews*. 39(6):2184–2202. DOI: 10.1039/b912552c.

Bligaard, T. and Nørskov, J.K. 2007. Ligand effects in heterogeneous catalysis and electrochemistry. *Electrochimica Acta*. 52(18):5512–5516. DOI: 10.1016/j.electacta.2007.02.041.

Brunauer, S., Emmett, P.H. and Teller, E. 1938. Adsorption of Gases in Multimolecular Layers. *J. Am.Chem.Soc.* 60(2):309–319.

Chong, L., Wen, J., Kubal, J., Sen, F.G., Zou, J., Greeley, J., Chan, M., Barkholtz, H., et al. 2018. Ultralow-loading platinum-cobalt fuel cell catalysts derived from imidazolate frameworks. *Science (New York, N.Y.)*. 362(6420):1276–1281. DOI: 10.1126/science.aau0630.

DOE Fuel Cell Technologies Office. 2016. Available: https://www.energy.gov/sites/default/files/2017/05/f34/fcto_myrdd_fuel_cells.pdf.

Du, L., Prabhakaran, V., Xie, X., Park, S., Wang, Y. and Shao, Y. 2021. Low-PGM and PGM-Free Catalysts for Proton Exchange Membrane Fuel Cells: Stability Challenges and Material Solutions. *Advanced Materials*. 33(6):1–18. DOI: 10.1002/adma.201908232.

Garsany, Y., Baturina, O.A., Swider-Lyons, K.E. and Kocha, S.S. 2010. Experimental methods for quantifying the activity of platinum electrocatalysts for the oxygen reduction reaction. *Analytical Chemistry*. 82(15):6321–6328. DOI: 10.1021/ac100306c.

Garsany, Y., Atkinson, R.W., Gould, B.D. and Swider-Lyons, K.E. 2018. High power, Low-Pt membrane electrode assemblies for proton exchange membrane fuel cells. *Journal of Power Sources*. 408(October):38–45. DOI: 10.1016/j.jpowsour.2018.10.073.

Gatto, I., Stassi, A., Baglio, V., Carbone, A., Passalacqua, E., Aricò, A.S., Schuster, M. and Bauer, B. 2015. Optimization of perfluorosulphonic ionomer amount in gas diffusion electrodes for PEMFC operation under automotive conditions. *Electrochimica Acta*. 165:450–455. DOI: 10.1016/j.electacta.2015.03.068.

Guo, Y., Pan, F., Chen, W., Ding, Z., Yang, D., Li, B., Ming, P. and Zhang, C. 2021.

*The Controllable Design of Catalyst Inks to Enhance PEMFC Performance: A Review*. V. 4. Springer Singapore. DOI: 10.1007/s41918-020-00083-2.

Hargreaves, J., McFarlane, A. and Said, L. 2018. Available: https://app.knovel.com/hotlink/khtml/id:kt011TW221/alternative-catalytic/oxygen-reduction-reaction.

Higuchi, E., Uchida, H. and Watanabe, M. 2005. Effect of loading level in platinum-dispersed carbon black electrocatalysts on oxygen reduction activity evaluated by rotating disk electrode. *Journal of Electroanalytical Chemistry*. 583(1):69–76. DOI: 10.1016/j.jelechem.2005.01.041.

Holdcroft, S. 2014. Fuel cell catalyst layers: A polymer science perspective. *Chemistry of Materials*. 26(1):381–393. DOI: 10.1021/cm401445h.

Hu, Z., Xu, L., Gan, Q., Du, X., Dai, W., Wang, Q., Zheng, W., Ding, Y., et al. 2021. Carbon corrosion induced fuel cell accelerated degradation warning: From mechanism to diagnosis. *Electrochimica Acta*. 389:138627. DOI: 10.1016/j.electacta.2021.138627.

Itota, B.J., Chowdhury, M., Barron, O. and Chamier, J. 2022. The impact of the thermal treatment during ink preparation on the ionomer-supported catalyst interactions in the catalyst layers. *International Journal of Hydrogen Energy*. 47(10):6848–6859. DOI: 10.1016/j.ijhydene.2021.12.060.

Kaewsai, D., Piumsomboon, P., Pruksathorn, K. and Hunsom, M. 2017. Synthesis of polyaniline-wrapped carbon nanotube-supported PtCo catalysts for proton exchange membrane fuel cells: activity and stability tests. *RSC Advances*. 7(34):20801–20810. DOI: 10.1039/C7RA01514C.

Kaur, G. 2022. *PEM Fuel Cells - Fundamentals, Advanced Technologies, and Practical Application*. Elsevier. DOI: 10.1016/C2020-0-00143-X.

Kim, D.S., Welch, C., Hjelm, R.P., Kim, Y.S. and Guiver, M.D. 2012. *Polymers in Membrane Electrode Assemblies*. V. 10. Elsevier B.V. DOI: 10.1016/B978-0-444-53349-4.00287-9.

Kim, K.H., Lee, K.Y., Kim, H.J., Cho, E.A., Lee, S.Y., Lim, T.H., Yoon, S.P., Hwang, I.C., et al. 2010. The effects of Nafion® ionomer content in PEMFC MEAs prepared by a catalyst-coated membrane (CCM) spraying method. *International Journal of Hydrogen Energy*. 35(5):2119–2126. DOI: 10.1016/j.ijhydene.2009.11.058.

Kocha, S.S., Shinozaki, K., Zack, J.W., Myers, D.J., Kariuki, N.N., Nowicki, T., Stamenkovic, V., Kang, Y., et al. 2017. Best Practices and Testing Protocols for Benchmarking ORR Activities of Fuel Cell Electrocatalysts Using Rotating Disk Electrode. *Electrocatalysis*. 8(4):366–374. DOI: 10.1007/s12678-017-0378-6.

Kumano, N., Kudo, K., Suda, A., Akimoto, Y., Ishii, M. and Nakamura, H. 2019. Controlling cracking formation in fuel cell catalyst layers. *Journal of Power Sources*. 419(February):219–228. DOI: 10.1016/j.jpowsour.2019.02.058.

Lei, C., Bessarabov, D., Ye, S., Xie, Z., Holdcroft, S. and Navessin, T. 2011. Low equivalent weight short-side-chain perfluorosulfonic acid ionomers in fuel cell cathode

catalyst layers. *Journal of Power Sources*. 196(15):6168–6176. DOI: 10.1016/j.jpowsour.2011.03.024.

Lei, C., Yang, F., Macauley, N., Spinetta, M., Purdy, G., Jankovic, J., Cullen, D.A., More, K.L., et al. 2021. Impact of Catalyst Ink Dispersing Solvent on PEM Fuel Cell Performance and Durability. *Journal of The Electrochemical Society*. 168(4):044517. DOI: 10.1149/1945-7111/abf2b0.

Li, D., Pan, Y.-T., Wang, X., Wang, C., Kim, Y.S. and Spendelow, J.S. 2019. Effect of the Catalyst Metal Content on PEMFC Durability. *ECS Meeting Abstracts*. MA2019-02(35):1575–1575. DOI: 10.1149/ma2019-02/35/1575.

Li, T., Shen, J., Chen, G., Guo, S. and Xie, G. 2020. Performance Comparison of Proton Exchange Membrane Fuel Cells with Nafion and Aquivion Perfluorosulfonic Acids with Different Equivalent Weights as the Electrode Binders. *ACS Omega*. 5(28):17628–17636. DOI: 10.1021/acsomega.0c02110.

Myers, D.J., Kropf, A.J., Wegener, E.C., Mistry, H., Kariuki, N. and Park, J. 2021. Degradation of Platinum-Cobalt Alloy PEMFC Cathode Catalysts in Catalyst-Ionomer Inks. *Journal of The Electrochemical Society*. 168(4):044510. DOI: 10.1149/1945-7111/abf4ab.

National Institute of Standards and Technology. 2006. *PEM Fuel Cells*. Available: https://www.physics.nist.gov/MajResFac/NIF/pemFuelCells.html [2021, May 07].

Nikkuni, F.R., Dubau, L., Ticianelli, E.A. and Chatenet, M. 2015. Accelerated degradation of Pt3Co/C and Pt/C electrocatalysts studied by identical-location transmission electron microscopy in polymer electrolyte environment. *Applied Catalysis B: Environmental*. 176–177:486–499. DOI: 10.1016/j.apcatb.2015.04.035.

O'hayre Ryan, C.S.-W.C.W.G.P.F.B. 2016. Available: https://app.knovel.com/hotlink/khtml/id:kt00CR5M0Y/fuel-cell-fundamentals/polymer-electrolyte-membrane.

Orfanidi, A., Madkikar, P., El-Sayed, H.A., Harzer, G.S., Kratky, T. and Gasteiger, H.A. 2017. The Key to High Performance Low Pt Loaded Electrodes. *Journal of The Electrochemical Society*. 164(4):F418–F426. DOI: 10.1149/2.1621704jes.

Papadias, D.D., Ahluwalia, R.K., Kariuki, N., Myers, D., More, K.L., Cullen, D.A., Sneed, B.T., Neyerlin, K.C., et al. 2018. Durability of Pt-Co Alloy Polymer Electrolyte Fuel Cell Cathode Catalysts under Accelerated Stress Tests. *Journal of The Electrochemical Society*. 165(6):F3166–F3177. DOI: 10.1149/2.0171806jes.

Pollet, B.G. and Kocha, S.S. 2022. *Using Ultrasound to Effectively Homogenise Catalyst Inks: Is this Approach Still Acceptable? Recommendations on the use of ultrasound for mixing catalyst inks*. V. 66. DOI: 10.1595/205651321X16196162869695.

Pollet, B.G., Kocha, S.S. and Staffell, I. 2019. Current status of automotive fuel cells for sustainable transport. *Current Opinion in Electrochemistry*. 16:90–95. DOI: 10.1016/j.coelec.2019.04.021.

Qi, Z. and Kaufman, A. 2003. Low Pt loading high performance cathodes for PEM fuel

cells. *Journal of Power Sources*. 113(1):37–43. DOI: 10.1016/S0378-7753(02)00477-9.

Ramaswamy, N., Kumaraguru, S., Gu, W., Kukreja, R.S., Yu, K., Groom, D. and Ferreira, P. 2021. High-Current Density Durability of Pt/C and PtCo/C Catalysts at Similar Particle Sizes in PEMFCs. *Journal of The Electrochemical Society*. DOI: 10.1149/1945-7111/abe5ea.

Riese, A., Banham, D., Ye, S. and Sun, X. 2015. Accelerated Stress Testing by Rotating Disk Electrode for Carbon Corrosion in Fuel Cell Catalyst Supports. *Journal of The Electrochemical Society*. 162(7):F783–F788. DOI: 10.1149/2.0911507jes.

Santiago, E.I., Varanda, L.C. and Villullas, H.M. 2007. Carbon-supported Pt-Co catalysts prepared by a modified polyol process as cathodes for PEM fuel cells. *Journal of Physical Chemistry C*. 111(7):3146–3151. DOI: 10.1021/jp0670081.

Sasikumar, G., Ihm, J.W. and Ryu, H. 2004. Dependence of optimum Nafion content in catalyst layer on platinum loading. *Journal of Power Sources*. 132(1–2):11–17. DOI: 10.1016/j.jpowsour.2003.12.060.

Sethuraman, V.A., Weidner, J.W., Haug, A.T., Pemberton, M. and Protsailo, L. V. 2009. Importance of catalyst stability vis-à-vis hydrogen peroxide formation rates in PEM fuel cell electrodes. *Electrochimica Acta*. 54(23):5571–5582. DOI: 10.1016/j.electacta.2009.04.062.

Shinozaki, K., Morimoto, Y., Pivovar, B.S. and Kocha, S.S. 2016. Suppression of oxygen reduction reaction activity on Pt-based electrocatalysts from ionomer incorporation. *Journal of Power Sources*. 325:745–751. DOI: 10.1016/j.jpowsour.2016.06.062.

Sneed, B.T., Cullen, D.A., Mukundan, R., Borup, R.L. and More, K.L. 2018. PtCo Cathode Catalyst Morphological and Compositional Changes after PEM Fuel Cell Accelerated Stress Testing. *Journal of The Electrochemical Society*. 165(6):F3078–F3084. DOI: 10.1149/2.0091806jes.

Stamenković, V., Schmidt, T.J., Ross, P.N. and Marković, N.M. 2002. Surface composition effects in electrocatalysis: Kinetics of oxygen reduction on well-defined Pt3Ni and Pt3Co alloy surfaces. *Journal of Physical Chemistry B*. 106(46):11970–11979. DOI: 10.1021/jp021182h.

Stariha, S., Macauley, N., Sneed, B.T., Langlois, D., More, K.L., Mukundan, R. and Borup, R.L. 2018. Recent Advances in Catalyst Accelerated Stress Tests for Polymer Electrolyte Membrane Fuel Cells. *Journal of The Electrochemical Society*. 165(7):F492–F501. DOI: 10.1149/2.0881807jes.

Takahashi, I. and Kocha, S.S. 2010. Examination of the activity and durability of PEMFC catalysts in liquid electrolytes. *Journal of Power Sources*. 195(19):6312–6322. DOI: 10.1016/j.jpowsour.2010.04.052.

Takahashi, S., Mashio, T., Horibe, N., Akizuki, K. and Ohma, A. 2015. Analysis of the Microstructure Formation Process and Its Influence on the Performance of Polymer Electrolyte Fuel-Cell Catalyst Layers. *ChemElectroChem*. 2(10):1560–1567. DOI: 10.1002/celc.201500131.

Toda, T., Igarashi, H., Uchida, H. and Watanabe, M. 1999. Enhancement of the Electroreduction of Oxygen on Pt Alloys with Fe, Ni, and Co. *Journal of The Electrochemical Society*. 146(10):3750–3756. DOI: 10.1149/1.1392544.

Tsotridis, G., Pilenga, A., Marco, G. De and Malkow, T. 2015. *EU Harmonised Test Protocols for PEMFC MEA Testing in Single Cell Configuration for Automotive Applications; JRC Science for Policy report*. DOI: 10.2790/54653.

Wang, C. and Spendelow, J.S. 2021. Recent developments in Pt–Co catalysts for proton-exchange membrane fuel cells. *Current Opinion in Electrochemistry*. 28:100715. DOI: 10.1016/j.coelec.2021.100715.

Wang, C., Cheng, X., Yan, X., Shen, S., Ke, C., Wei, G. and Zhang, J. 2019. Respective Influence of Ionomer Content on Local and Bulk Oxygen Transport Resistance in the Catalyst Layer of PEMFCs with Low Pt Loading. *Journal of The Electrochemical Society*. 166(4):F239–F245. DOI: 10.1149/2.0401904jes.

Wang, Y., Ruiz Diaz, D.F., Chen, K.S., Wang, Z. and Adroher, X.C. 2020. Materials, technological status, and fundamentals of PEM fuel cells – A review. *Materials Today*. 32(February):178–203. DOI: 10.1016/j.mattod.2019.06.005.

Wang, Y.J., Zhao, N., Fang, B., Li, H., Bi, X.T. and Wang, H. 2015. Carbon-Supported Pt-Based Alloy Electrocatalysts for the Oxygen Reduction Reaction in Polymer Electrolyte Membrane Fuel Cells: Particle Size, Shape, and Composition Manipulation and Their Impact to Activity. *Chemical Reviews*. 115(9):3433–3467. DOI: 10.1021/cr500519c.

Xu, H., Kunz, H.R., Bonville, L.J. and Fenton, J.M. 2007. Improving PEMFC Performance Using Low Equivalent Weight PFSA Ionomers and Pt-Co/C Catalyst in the Cathode. *Journal of The Electrochemical Society*. 154(2):B271. DOI: 10.1149/1.2401059.

Yang, C.J. 2009. An impending platinum crisis and its implications for the future of the automobile. *Energy Policy*. 37(5):1805–1808. DOI: 10.1016/j.enpol.2009.01.019.

Yang, D., Guo, Y., Tang, H., Wang, Y., Yang, D., Ming, P., Zhang, C., Li, B., et al. 2021. Influence of the dispersion state of ionomer on the dispersion of catalyst ink and the construction of catalyst layer. *International Journal of Hydrogen Energy*. 46(66):33300–33313. DOI: 10.1016/j.ijhydene.2021.07.172.

Yoshimune, W. and Harada, M. 2019. Effect of Pt loading on the adsorption of perfluoro-sulfonic acid ionomer in catalyst ink for polymer electrolyte fuel cells. *Chemistry Letters*. 48(5):487–490. DOI: 10.1246/cl.190017.

Yu, X. and Ye, S. 2007. Recent advances in activity and durability enhancement of Pt/C catalytic cathode in PEMFC. Part II: Degradation mechanism and durability enhancement of carbon supported platinum catalyst. *Journal of Power Sources*. 172(1):145–154. DOI: 10.1016/j.jpowsour.2007.07.048.

Yuan, X.-Z., Song, C., Wang, H. and Zhang, J. 2010. *Electrochemical Impedance Spectroscopy in PEM Fuel Cells*. London: Springer London. DOI: 10.1007/978-1-84882-846-9.

Yuanbo Engineering. n.d. *Cross-Section of Membrane Electrode Assembly Layers*. Available: https://www.pemteco.com/technology/membrane-electrode-assembly-type.html [2022, October 25].

Zignani, S.C., Antolini, E. and Gonzalez, E.R. 2008. Evaluation of the stability and durability of Pt and Pt-Co/C catalysts for polymer electrolyte membrane fuel cells. *Journal of Power Sources*. 182(1):83–90. DOI: 10.1016/j.jpowsour.2008.03.061.